NEUTRON SCATTERING FROM NAPHTHALENE AND AMMONIUM DIHYDROGEN PHOSPHATE

Thesis

Submitted by

ELIZABETH ANNE YEATS, B.Sc.

For the degree of

Doctor of Philosophy

University of Edinburgh,

Department of Natural Philosophy.

MARCH, 1971.

C O N T E N T S

Page

CHAPTER 1

AN INTRODUCTION TO NEUTRON SCATTERING FROM CRYSTALS

1.1 The Lattice Dynamics of Crystals in the Harmonic Approximation 1

1.2 Neutron Scattering Cross-Sections . . . 6

1.2a. Bragg Scattering 8

1.2b. One-Phonon Scattering 9

1.2c. Incoherent Scattering 10

1.3 The Measurement of Phonon Dispersion Curves . . 11

1.4 The Resolution of a Triple Axis Spectrometer . 13

1.5 Focussing a Triple Axis Spectrometer . . . 17

1.6 Spurious Peaks in the Scattered Neutron Count Rate. 20

1.7 The Operation of a Triple Axis Spectrometer . . 21

CHAPTER 2

A NEUTRON DIFFRACTION STUDY OF PERDEUTERONAPHTHALENE

2.1 Introduction 24

2.2 The Structure Factor for Bragg Scattering of Neutrons 24

2.3 Experimental Procedure 26

2.4 Determination of Structure Factors from Experimental Intensity Data 28

Absorption 30

Extinction 31

Renninger Effect 32

Determination of Scale Factor from a Wilson Plot. 33

2.5 The Structure Refinement 35

2.5.1 The Rigid-Body Thermal Motion Constraint (R.B.T.P. Constraint) 35

2.5.2 Discussion of R.B.T.P. Constrained Refinement. 37

2.5.3 Refinement under m m m Symmetry Constraint 40

2.5.4 Refinement under Further Molecular Symmetry Constraint. 41

C O N T E N T S (Contd.)

		Page
	2.5.5 The Correlation Matrix . . .	41
2.6	Further Refinements of Neutron Diffraction Data .	42
2.7	Discussion	45

CHAPTER 3

THE LATTICE DYNAMICS OF NAPHTHALENE

3.1	Theoretical Introduction	48
3.2	The Preliminary Calculation and its Results .	52
3.3	The Effect of Molecular Distortion on the Phonon. Frequencies	55
3.4	The One-Phonon Structure Factors for Naphthalene.	56
3.5	The Measurement of Phonon Frequencies in $C_{10}D_8$.	57
3.6	The Dependence of Phonon Frequencies on the Model Parameters	59
3.7	Comparison of Experimental and Calculated Phonon Dispersion Curves	61

CHAPTER 4

FERRO-ELECTRICITY AND ANTIFERRO-ELECTRICITY IN KH_2PO_4 AND $NH_4H_2PO_4$

4.1	Introduction	66
4.2	The Crystal Structures	66
	4.2a KH_2PO_4	68
	4.2b $NH_4H_2PO_4$	69
4.3	The Dielectric Constants as Functions of Temperature	70
4.4	Ferroelectricity and Low Frequency Modes in Perovskites	71

C O N T E N T S (Contd.)

		Page
4.5	The Significance of the Eigenvectors . .	74
4.6	The Use of Group Theory	75
4.7	Experimental Evidence for Low Frequency Modes in KH_2PO_4	80
4.8	Coupled Phonon and Tunnelling Modes in KH_2PO_4 and Kobayashi's Theory	83

CHAPTER 5

EXPERIMENTAL MEASUREMENTS ON DEUTERATED AMMONIUM DIHYDROGEN PHOSPHATE ($ND_4D_2PO_4$)

5.1	Experimental	87
5.2	Measurement of Quasi-elastic Intensity round the M-point in $ND_4D_2PO_4$	90
5.3	The $ND_4D_2PO_4$ Γ -point Scattering . . .	93
5.4	Resolution Considerations	94
	5.4a. For $\Delta E = 0$	94
	5.4b. For Energy Analysis	98

CHAPTER 6

THE EIGENVECTOR DETERMINATION FOR THE ANTIFERROELECTRIC MODE IN $ND_4D_2PO_4$

6.1	Examples of Eigenvector Determination . .	101
	6.1a. Perovskites	101
	6.1b. The Ferro-electric Mode in KD_2PO_4 . .	102
	6.1c. The Anti-ferroelectric Mode in $ND_4D_2PO_4$.	104
6.2	A Fourier Synthesis Method for Eigenvectors .	106

C O N T E N T S (Contd.)

		Page
6.3	Series Termination Effects	110
6.4	Applications of the Fourier Synthesis Method .	112
	6.4a) $D'(\underline{r})$ for the KD_2PO_4 Ferro-electric mode	112
	6.4b) $D(\underline{r})$ for the $ND_4D_2PO_4$ anti-ferroelectric mode	116
6.5	The Approximation Used to Calculate $F(\underline{K})$ . .	118
6.6	Discussion	119
	6.6a) KD_2PO_4	121
	6.6b) $ND_4D_2PO_4$	122
Acknowledgements		124
References		125

SUMMARY

In this thesis we examine aspects of coherent neutron scattering from crystals, and show that it is a powerful method for locating atomic positions in crystals as well as obtaining information on the frequencies and patterns of atomic motion in crystal vibrations.

In the first chapter the theory of lattice dynamics in the harmonic approximation is developed, and expressions presented for the cross-sections for neutrons scattered from non-magnetic crystals under various experimental conditions. The use of a triple axis spectrometer to measure the energy versus wave vector relation of the vibrations in a crystal is described. The idea of instrumental resolution and focussing is introduced, and its relevance to our measurements is considered.

The measurement of neutron elastic scattering from perdeuteronaphthalene is described, and the deduction of elastic structure factors from experimental intensity data is presented. We perform several constrained refinements of the data, and show that this approach can often give results of higher physical significance than a conventional unconstrained refinement.

The theory of lattice dynamics is then extended to include molecular crystals. Starting from an interatomic potential in parametric form, the phonon dispersion curves for naphthalene are calculated. The dependence of phonon frequencies on the potential parameters is examined, and the measurement of these frequencies using a triple axis spectrometer is described. The results of several model calculations are given, and the

discrepancies between theory and experiment examined.

Ferroelectricity and antiferroelectricity in KH_2PO_4 and $NH_4H_2PO_4$ is the subject of the second part of this thesis. The lattice dynamical approach to the problem of ferro-electricity is stressed, and the use of group theory, in determining the pattern of atomic displacements in the so-called "ferro-electric mode" is described. Experimental evidence is given, which shows that this mode is over-damped in KD_2PO_4, and neutron scattering from it is quasi-elastic.

The antiferro-electric and ferro-electric modes in $ND_4D_2PO_4$ also scatter neutrons quasi-elastically, and we describe the use of a triple axis spectrometer to measure this type of scattering. Its distribution in reciprocal space is described, and the results of energy analysis of the scattering are presented.

The determination of the eigenvector of the antiferro-electric mode from a set of quasi-elastic intensities is then described. We use both a least squares procedure, and a Fourier synthesis method to solve this problem and compare the results with the corresponding calculations for the KD_2PO_4 ferro-electric mode. Finally we examine the validity of our solution, in the light of the various criticisms of these methods.

I declare that, unless otherwise indicated, the work described in this thesis is my own unaided work.

Elizabeth A. Yeats

CHAPTER 1

AN INTRODUCTION TO NEUTRON SCATTERING FROM CRYSTALS

Many excellent review articles have been written on most of the topics considered in this chapter. However, we attempt to present, in a fairly logical manner, the ideas, quantities and equations which we shall require later, and discuss their relevance to our work. Of necessity, much is omitted and, throughout, the reader is referred to the appropriate reviews if he wishes to read to greater depth in any particular topic.

We consider the theory of atomic vibrations in a crystal and show how they govern its neutron inelastic scattering properties. In particular, we use the scattering cross-section to discuss what processes in the crystal scatter neutrons under various experimental conditions. We then describe the use of the triple axis crystal spectrometer to measure the energy versus wave vector spectrum of crystal vibrations, and conclude with a discussion of the instrumental resolution.

1.1 The Lattice Dynamics of Crystals in the Harmonic Approximation

The theory of lattice dynamics in the harmonic approximation has been developed by Born and collaborators[1], and we shall use their notation wherever possible. Review articles and recent developments of the theory have been contributed by Cochran[2,3,4], Cochran and Cowley[5] and Maradudin and others[6].

We assume that, for a crystal with the k^{th} atom in the ℓ^{th}

unit cell having a displacement $\underline{u}(\ell k)$ from its equilibrium position $\underline{R}(\ell k)$, the potential energy may be written

$$\phi = \phi_0 + \phi_1 + \phi_2 + \cdots\cdots$$

where
$$\phi_1 = \sum_{\ell k x} \frac{\partial \phi}{\partial x(\ell k)} u_x(\ell k) \qquad (1.1)$$

and

$$\phi_2 = \tfrac{1}{2} \sum_{\ell k x} \sum_{\ell' k' y} \frac{\partial^2 \phi}{\partial x(\ell k)\, \partial y(\ell' k')} u_x(\ell k) u_y(\ell' k') \, .$$

Under the adiabatic approximation, $\phi_1 = 0$ for a crystal initially in equilibrium, and we shall only consider the harmonic approximation in which all terms in the expansion of ϕ above ϕ_2 are ignored. The equation of motion for atom k in the ℓ^{th} unit cell is then

$$m_k \frac{\partial^2}{\partial t^2} \left[u_x(\ell k) \right] = - \sum_{\ell' k' y} \phi_{xy}(\ell k \ell' k') u_y(\ell' k') \qquad (1.2)$$

where the ϕ_{xy} replace the second derivatives of equation (1.1), and are force constants. If we assume that the $u_x(\ell k)$ may be expressed as a superposition of travelling waves, each of the form

$$u_x(\ell k) = \frac{1}{\sqrt{m_k}} U_x(k \underline{q}) \exp i \left[\underline{q}.\underline{R}(\ell k) - \omega(\underline{q}) t \right] \, , \qquad (1.3)$$

then substitution in equation (1.2) gives

$$\omega^2(\underline{q}) U_x(k \underline{q}) = \sum_{k' y} M_{xy}(k k' \underline{q}) U_y(k' \underline{q}) \qquad (1.4)$$

with $$M_{xy}(k k' \underline{q}) = \frac{1}{\sqrt{m_k m_{k'}}} \sum_{\ell'} \phi_{xy}(\ell k \ell' k') \exp i \left(\underline{q}.\left[\underline{R}(\ell' k') - \underline{R}(\ell k) \right] \right).$$

Since $\underline{R}(\ell k) = \underline{R}(\ell) + \underline{R}(k)$ we may include $\exp(i\underline{q}.\underline{R}(\ell))$ in $\underline{U}$ redefining its phase. Then $M_{xy}(kk'\underline{q})$ is independent of ℓ and is an element of the dynamical matrix, $\underline{M}$. The equations of motion are now

$$\omega^2\underline{U} = \underline{M}\,\underline{U} \quad . \tag{1.5}$$

$\underline{U}$ is a column matrix and $\underline{M}$ is a $3N \times 3N$ matrix if there are N atoms in the unit cell. Demanding a non-trivial solution of equation (1.5) determines $3N$ values of $\omega_j^2(\underline{q})$, each of which gives an eigenvector $\underline{U}_j(\underline{q})$ whose components are the reduced (i.e. $\sqrt{m}$ included) atomic displacements in the mode j, there being three for each atom.

We may write the displacement of the k^{th} atom, under simultaneous excitation of all possible modes, as

$$\underline{u}(\ell k) = \frac{1}{\sqrt{Nm_k}} \sum_{\underline{q}j} \underline{U}_j(\underline{q})Q(\underline{q}j)\exp i\,\underline{q}.\underline{R}(\ell k) \tag{1.6}$$

which expresses $\underline{u}(\ell k)$ in terms of the $3N$ normal modes. The $Q(\underline{q}j)$ are normal co-ordinates for, it may be shown (see for example reference 5) that the system Hamiltonian is

$$H = \tfrac{1}{2} \sum_{\underline{q}j} \left(\left|\dot{Q}(\underline{q}j)\right|^2 + \omega^2(\underline{q}j)\left|Q(\underline{q}j)\right|^2 \right) \quad . \tag{1.7}$$

The summation is over all possible values of $\underline{q}$. We now consider how many distinct values of $\underline{q}$ there are for a crystal of $\mathcal{N}$ unit cells defined by vectors $\underline{a}_1, \underline{a}_2, \underline{a}_3$, and whose reciprocal lattice is defined by $\underline{b}_1$, $\underline{b}_2$, $\underline{b}_3$. We select a volume of crystal defined by $N_1\underline{a}_1$, $N_2\underline{a}_2$, $N_3\underline{a}_3$ and impose periodic boundary conditions, i.e. the displacements of atoms separated by $\sum_{i=1}^{3} N_i\underline{a}_i$ must be the same. Possible values

of $\underline{q}$ are then $\underline{q} = \sum_{i=1}^{3} \frac{S_i \underline{b}_i}{N_i}$ where S_i are integers, (1.8)

and each reciprocal lattice cell contains $N_1 \times N_2 \times N_3$ distinct $\underline{q}$'s. If $N_1 \times N_2 \times N_3$ is large these $\underline{q}$'s are distributed almost continuously. Equation (1.4) shows that $\omega_j(\underline{q}) = \omega_j(\underline{q} + \underline{\tau})$ where $\underline{\tau}$ is any reciprocal lattice vector, and so the first Brillouin zone contains all distinct modes. In equation (1.7) we sum over all these values of $\underline{q}$, and over all $3N$ values of j for each $\underline{q}$.

Returning to equation (1.4) we see that we may calculate the $3N \times 3N$ elements of the dynamical matrix for a particular $\underline{q}$, and find its eigenvalues and eigenvectors, $\omega^2(\underline{q}j)$ and $\underline{U}(\underline{q}j)$, providing the $\phi_{xy}(\ell k \ell' k')$ are known. Each $\underline{U}(\underline{q}j)$ describes a pattern of atomic vibrations in the crystal which is independent of all other patterns, $\underline{U}(\underline{q}j')$ $(j' \neq j)$, and is a normal mode of vibration of the crystal at a particular instant of time. These normal modes have a time variation expressed by $\exp(-i\omega(\underline{q}j)t)$, and are usually called phonon modes. By repeating the calculation for many $\underline{q}$'s in the Brillouin zone, we may obtain $\omega(\underline{q}j)$ as a function of $\underline{q}$ and build up the phonon dispersion curves of the crystal. Any pattern of atomic displacements existing in the crystal may be expressed as a superposition of these normal modes at a particular time, t.

From equation (1.2) we see that the $\phi_{xy}(\ell k \ell' k')$ give the force in the x-direction on the atom (ℓk) when atom $(\ell' k')$ has a small unit displacement along y. There are, in general, 9 independent ϕ_{xy}'s for each pair of atoms (ℓk) and $(\ell' k')$, and for a crystal with long-range forces we must include distant neighbour interactions, i.e. a large number of values of $(\ell' k')$

must be considered. The number of independent ϕ_{xy}'s is then reduced by imposing translational invariance, i.e. there can be no nett force on any atom as a direct result of a uniform translational displacement of the crystal. If all atoms are given the same displacement, then translational invariance applied to equation (1.2) requires that

$$- \sum_{\substack{\ell k \neq \\ \ell' k'}} \phi_{xy}(\ell k \ell' k') = \phi_{xy}(\ell k \ell k) \quad . \qquad (1.9)$$

Equation (1.9) defines the "self-terms", i.e. the $\phi_{xy}(\ell k \ell' k')$ for $\ell = \ell'$ and $k = k'$. This incidentally ensures that some modes, the acoustic modes, have frequencies which go to zero as $\underline{q} \rightarrow 0$. Crystal symmetry reduces the number of independent elements of $\underline{M}$. Naphthalene is the only crystal for which we make calculations of the phonon dispersion curves. Since this crystal has low symmetry, we are not required to consider the ways in which the number of independent ϕ_{xy}'s may be reduced for crystals of high symmetry. The reader is referred to a paper by Herman[7] for details of the process for the diamond structure. In Chapter 3 we shall consider this point specifically for the naphthalene crystal.

We have discussed how the phonon dispersion curves of a crystal may be calculated from the ϕ_{xy}'s. If the number of independent ϕ_{xy}'s is not large, experimental phonon frequencies may be used to find these force constants, usually by comparing observed and calculated frequencies and using a least squares procedure to find the best values of the ϕ_{xy}. These ϕ_{xy} may then be interpreted in terms of known interactions, such as Coulomb and Van der Vaals. If there are many ϕ_{xy}'s to be

determined, an approach giving more meaningful results is to postulate the form of the interatomic potential as a parametric function and use it to calculate the individual force constants. The dynamical matrix may then be built up and solved to obtain a set of phonon frequencies for comparison with the experimental values. The potential function parameters are then varied to give better agreement between the two sets of frequencies.

An example of this approach is the treatment of the lattice dynamics of the molecular crystals naphthalene and anthracene. Pawley[8] has calculated phonon dispersion curves in these crystals starting from a Buckingham potential. This allows description of an extremely complex system of interactions by a small number of parameters. The general theory must be extended slightly for a molecular crystal, and this is presented in Chapter 3, along with a discussion of the dispersion curves for naphthalene.

1.2 Neutron Scattering Cross-Sections

The general theory of neutron scattering has been developed by Weinstock[9] and other workers. Van Hove[10] has used a different, but equivalent, approach. We make very little attempt to derive the results which we require, and the interested reader is recommended to refer to the original papers for details. The probability of a particle of wave vector $\underline{k}_o$ being scattered by a system for which the interaction Hamiltonian is H' is

$$w = \frac{2\pi}{\hbar} |H'_{fi}|^2 \left(\frac{1}{2\pi}\right)^3 \frac{k_1 M}{\hbar^2} \, dE_F \, d\Omega \, \delta(E_f - E_i) \quad .$$

$\underline{k}_1$ is the scattered wave vector, the delta function expresses

energy conservation, and

$$H'_{fi} = \sum_{mn} \langle m | e^{-i\underline{k}_1 \cdot \underline{r}} V(\underline{r}) e^{i\underline{k}_o \cdot \underline{r}} | n \rangle \qquad (1.10)$$

with $V(\underline{r})$ depending on the interaction. $|m\rangle$ and $|n\rangle$ are states of the system. For an incident flux of particles, $\frac{\hbar k_o}{M}$, the scattering cross-section is

$$\frac{d^2\sigma}{dE_F d\Omega} = \left(\frac{M}{2\pi\hbar^2}\right)^2 \frac{k_1}{k_o} |H'_{fi}|^2 \delta\left(\frac{\hbar^2 k_1^2}{2M} + E_f^s - \frac{\hbar^2 k_o^2}{2M} - E_i^s\right) \qquad (1.11)$$

where E_i^s and E_f^v are the initial and final energies of the system. For thermal neutrons scattered from a non-magnetic crystal, H' arises only from interaction with nuclei, for which it is sufficient to consider s-wave scattering. A suitable form of $V(\underline{r})$ is

$$V(\underline{r}) = \left(\frac{2\pi\hbar}{M}\right) \sum_{\ell} b(\ell)\, \delta(\underline{r} - \underline{r}(\ell)) \qquad (1.12)$$

where $b(\ell)$ is a scattering length. For simplicity we consider one atom in the unit cell only, the extension to k atoms being fairly obvious. Substituting equation (1.12) in (1.10), it may be seen that one term arises in which the scattering lengths are correlated with interference between scattering from atoms of different ℓ. This is the coherent part, the remainder is the incoherent part which arises from independent scattering from the atoms.

The coherent cross-section is

$$\frac{d^2\sigma^{coh}}{dE\, d\Omega} = \frac{k_1}{k_o}\, b_{coh}^2\, S^{coh}(\underline{K}, \omega) \quad ,$$

where $S^{coh}(\underline{K}, \omega)$ depends only on the wave vector change $\underline{K}$ and the energy transfer $\hbar\omega$. This was first emphasised by Van Hove.

The atomic positions are functions of time since the crystal vibrates, and by introducing a space-time correlation function it may be shown that

$$S^{coh}(\underline{K}\,\omega) = \sum_{\ell\ell'} \frac{1}{2\pi} \int_{-\infty}^{+\infty} e^{-i\omega t} \exp i\underline{K}.(\underline{R}(\ell') - \underline{R}(\ell)) \ll e^{-i\underline{K}.\underline{u}(\ell,0)} \; e^{i\underline{K}.\underline{u}(\ell' t)} \gg dt \quad .$$

Expanding the exponential, and using the results of Section 1.2,

$$S^{coh}(\underline{K}\,\omega) = S^{o\,coh}(\underline{K}\,\omega) + S'^{coh}(\underline{K}\,\omega) + \ldots . \qquad (1.13)$$

and we now discuss the form of the leading terms in this expansion.

a) Bragg Scattering

$$S^{o\,coh}(\underline{K}\,\omega) = \delta(\omega)\Delta(\underline{K} - \underline{\tau})Ne^{-2W} \left| \sum_{\ell} \exp(i\underline{K}.\underline{R}(\ell)) \right|^2 \qquad (1.14)$$

where $W = \frac{1}{2}\langle \underline{K}.\underline{u}(\ell) \rangle^2$.

The summation, ℓ is over all unit cells in the crystal, and the experimental conditions for observing this scattering are

$$|\underline{k}_o| = |\underline{k}_1| , \qquad \underline{K} = \underline{\tau} . \qquad (1.15)$$

Since $\left(\frac{d^2\sigma}{\partial E d\Omega}\right)^{coh}$ contains, for a crystal with several atoms k in the unit cell, terms with factors such as $\exp(i\underline{K}.\underline{R}(k_1))$, $\exp(i\underline{K}.\underline{R}(k_2))$ etc., it is seen that it is the crystal structure which governs the relative magnitudes of the cross-sections for different $\underline{K}$. This Bragg or elastic scattering cross-section only contains the motion of the atoms in the modifying factor, e^{-2W}.

b) One-phonon Scattering

$$S'^{\,coh}(\underline{K}\,\omega) = N\delta(\underline{K} - \underline{\tau} + \underline{q})\delta(-E \pm \hbar\omega(\underline{q}j)) \begin{Bmatrix} \bar{n}(\underline{q}j) \\ \bar{n}(\underline{q}j) + 1 \end{Bmatrix}$$

$$\times \left| \left(\frac{1}{Nm}\right)^{\frac{1}{2}} \left(\frac{1}{\omega(\underline{q}j)}\right)^{\frac{1}{2}} \underline{K}.\underline{U}_j(\underline{q}) \exp(-W(\underline{K})) \exp(i\underline{K}.\underline{R}(\ell)) \right|^2 \qquad (1.16)$$

for scattering from mode $(\underline{q}j)$. The $\bar{n}$ are thermally averaged occupation numbers, the upper applying for scattering with neutron energy gain, the lower for neutron energy loss. From this expression is obtained the one-phonon "structure factor", $G(\underline{K}j)$ which, for a crystal with k atoms in the unit cell, is

$$\underline{K}.\sum_k b_k \exp(-\tfrac{1}{2}W_k(\underline{K}))m_k^{-\frac{1}{2}} \underline{e}_k(\underline{q}j)\exp(i\underline{\tau}.\underline{R}_k) \qquad (1.17)$$

(we have written b_k for b(k), $\underline{R}_k$ for $\underline{R}(k)$, and replaced $\underline{U}_j(\underline{q})$ for atom k by $\underline{e}_k(\underline{q}j)$ which is more commonly used in this context). In general, $G(\underline{K}j)$ is a complex quantity, but the scattering cross-section, proportional to $|G(\underline{K}j)|^2$, is always real.

Experimental conditions must satisfy

$$\frac{|\underline{k}_o|^2}{2M} - \frac{|\underline{k}_1|^2}{2M} = \pm\hbar\omega(\underline{q}j)$$

$$\underline{K} \pm \underline{q} = \underline{\tau} \qquad . \qquad (1.18)$$

$G(\underline{K}j)$ depends on the product of $\underline{K}$ with the mode polarisation vector $\underline{e}_k(\underline{q}j)$, i.e. it depends explicitly on the motion of the atoms as well as their positions in the unit cell. If the $\underline{e}_k(\underline{q}j)$ are known from symmetry arguments in simple crystals, or from model calculations in more complicated crystals, we may select the particular phonon mode from which neutrons are scattered predominantly, by choosing a $\underline{\tau}$ for which $G(\underline{K}j')$ is

considerably larger than $G(\underline{K}j)$ for all $j \neq j'$. As we show in Chapter 3, calculations of the $G(\underline{K}j)$ are essential for the measurement of phonon frequencies in molecular crystals, which usually have several modes within a small frequency range.

Thermal neutrons have wavelengths between 1Å and 2Å, with corresponding energies of 80 to 20 meV. The energies of the atomic vibrations of course depend on the strength of the restoring forces in the crystal through the ϕ_{xy}'s, and vary considerably. However the range between a few meV and 60 meV may be taken as typical. The energies of thermal neutrons are thus of the same order of magnitude as that of atomic vibrations, and it is possible to resolve the changes in neutron energy which occur on scattering from these vibrations.

The inverse ω-dependence of the cross-section (equation (1.16)) shows that the scattering peaks, for the acoustic modes, around the Bragg positions. These acoustic mode contributions account for most of the so-called "thermal diffuse" scattering from crystals. This ω-dependence also serves to reduce the intensity of scattering from the higher frequency modes relative to that from the acoustic branches.

c) The Inchoherent Scattering

The incoherent part of the scattering may similarly be expanded to give an elastic term which peaks at $\omega = 0$ and contains a $\underline{K}$-dependence expressed by the Debye-Waller factor, e^{-W}. All terms in this expansion depend on the incoherent scattering length, b^{incoh}, which for most nuclei is considerably less than b^{coh} (typically $b^{incoh} \approx 0.2\, b^{coh}$). However, b^{incoh} for hydrogen is exceptionally large, being about five times as large as a typical value of b^{coh}. The coherent phonon

peaks for hydrogenous materials lie on a strong incoherent background. Consequently these materials must be deuterated before attempting coherent scattering experiments.

1.3 The Measurement of Phonon Dispersion Curves

The triple axis crystal spectrometer presents a convenient method for measuring the frequencies of phonons with wave vectors ranging over the whole Brillouin zone. This machine has been used exclusively to perform the energy analysis of neutrons scattered coherently from naphthalene (Chapter 3) and $ND_4D_2PO_4$ (Chapter 5).

The instrumental design and operation have been described by Brockhouse[11], and we shall only discuss the points which are relevant to our measurements. Other methods have been described and used for measuring phonon frequencies; for example time-of-flight machines[12] and infra-red and Raman spectroscopy [13, 14]. However, the former rarely presents results in such a convenient form as the triple axis spectrometer and the optical methods, although they give better resolution than neutron measurements, are usually restricted to give information on phonons of only zero wave-vector. A discussion of these methods is not appropriate here, especially since the reviews give such an extensive list of references.

To satisfy equations (1.18) and give a peak in the scattered neutron intensity, corresponding to scattering from a phonon, the energy and wave vector change of the neutrons reaching the detector must be continuously variable. The orientation of the sample must also be variable to allow selection of the phonon wave vector $\underline{q}$ and the particular branch j, (the latter by

altering the $\underline{\tau}$ of equation (1.17).

In Figure 1.1 we illustrate a triple axis spectrometer schematically. A monochromator crystal (table 1) rotates so that neutrons of any desired energy, say E_o, may be selected from the reactor Maxwellian distribution by Bragg reflection to pass along arm 1. The direction of arm 1 and the angle of the monochromator define $\underline{k}_o$. The specimen table (table 2) is rotated and the angle between arms 1 and 2 is changed so that, although neutrons $\underline{k}_o$ are scattered by various processes in the sample, giving a range of scattered wave vectors, only those travelling in a single direction (along arm 2) fall on the analyser crystal (table 3). Arm 3 and table 3 are positioned so that only neutrons of one energy, say E_1, travelling along arm 2, can be Bragg reflected by the analyser to pass along arm 3 and so reach the detector. This ensures that the neutrons, say $\underline{k}_1$, counted in the detector, have exchanged wave vector $\underline{k}_o - \underline{k}_1$ and energy $E_o - E_1$ with the specimen. Equations (1.18) may be satisfied by keeping E_o or E_1 fixed.

The sensitivity of the analysing system is a function of E_1, which is difficult to measure or calculate. It is therefore better to keep E_1 fixed and vary E_o. Any dependence of the reflectivity of the monochromator upon E_o is unimportant since the counting time for each setting of the machine is controlled by a monitor counter placed in the monochromatic beam between monochromator and sample.

The scan through a chosen phonon peak is executed by varying $E_o - E_1$ and/or $\underline{k}_o - \underline{k}_1$ in steps over a range centred about the expected values of $\hbar\omega(\underline{q}j)$ and $\underline{\tau} + \underline{q}$.

The spectrometer is usually operated in one of two modes, called "constant-$\underline{K}$" and "constant-E" methods. In the former $\underline{k}_1 - \underline{k}_o$ is fixed and E_o is varied with E_1 fixed so that neutrons may be scattered by modes of wave vector $\underline{q}$, and a peak is obtained in the count rate when $E_o - E_1 = \pm \hbar\omega(\underline{q}j)$. Neutron loss was used exclusively, i.e. $E_o - E_1 = + \hbar\omega(\underline{q}j)$. In the "constant-E" mode, the energy transfer to the specimen is fixed, and $\underline{k}_o - \underline{k}_1$ varied so that $\underline{q}$ is altered. A peak in the counting rate occurs when $\underline{q}$ attains a value for which there is a phonon of energy $(E_o - E_1)$.

1.4 The Resolution of a Triple Axis Spectrometer

The machine resolution is important in the planning of an experiment, and it has been discussed by several authors. Cooper and Nathans[15] consider the problem in great detail, and it is to this paper that the reader who requires extensive knowledge should turn. We have found that restricted considerations presented by Peckham and others[16] were sufficient for our phonon measurements. Our investigation of $ND_4D_2PO_4$ was mainly concerned with the instrumental energy resolution, and we obtain a simple expression for this as a function of various instrumental parameters. We also discuss the effect on the $\underline{K}$-space resolution of altering some instrumental parameters.

To allow a reasonable number of neutrons to pass through the machine, there is finite collimation, in the form of Soller slits, along arms 1 and 2. This allows neutrons travelling at a small angle to the direction of $\underline{k}_o$ to reach the specimen, and those with wave vector not exactly along $\underline{k}_1$ to be reflected by the analyser crystal into the detector. Neutrons reaching the

detector have therefore a finite spread in energy, and the energy transfer to the sample is $E_o - E_1 \pm \Delta E$. The finite mosaic spreads of monochromator (η_m) and analyser (η_a) also contribute to the energy spread, but we shall show that their effect may usually be neglected. The finite resolution causes a broadening of, for example, phonon peaks in the distribution of scattered neutrons.

We assume that the angular transmission functions for Soller slits are of Gaussian shape - a good approximation for systems of divergence greater than 0.5°. (This condition applies here, since typical collimator widths for the instrument used are 0.8°). Neutrons scattered at $d\theta_m$ to the Bragg angle θ_m, for monochromator planes of spacing d_m, have a spread

$$d\lambda_o = 2d_m \cos\theta_m \, d\theta_m$$

or $$dk_o = k_o \cot\theta_m \, d\theta_m, \qquad dE_o = 2E_o \cot\theta_m \, d\theta_m \ .$$

If α_m is the full Gaussian width for the collimator in arm 1 (neutrons at $\alpha_m/2$ to the optimum angle have a probability $(\frac{1}{2\pi})^{\frac{1}{2}} \exp(-\frac{1}{2})$ of being transmitted), then we replace $d\theta_m$ by α_m to give the standard deviation of the Gaussian distribution of neutron energies arriving at the specimen as

$$\Delta E_o' = 2E_o \cot\theta_m \, \alpha_m \ .$$

The mosaic, η_m, gives an additional spread

$$\Delta E_o'' = 2E_o \cot\theta_m \, \eta_m .$$

The sum of the two independent Gaussians has a total energy spread

$$\Delta E_o = 2E_o \cot\theta_m \, (\alpha_m^2 + \eta_m^2)^{\frac{1}{2}} \ .$$

Typical values of η_m are 0.1^o or 0.2^o, and so

$$\Delta E_o \approx 2E_o \cot \theta_m \alpha_m \quad .$$

Similar arguments apply to the arm 2 collimator, specified by α_a.

$$\Delta E_1 = 2E_1 \cot \theta \alpha_a \quad .$$

Ignoring effects on the neutron wave vector distribution caused by scattering from the chosen process in the specimen, the energy resolution of the spectrometer is

$$\Delta E = \sqrt{\Delta E_o^2 + \Delta E_1^2} \quad .$$

If the machine is set to measure incoherent elastic scattering, a plot of the counting rate in the detector as a function of energy transfer will be a Gaussian, centred at zero energy transfer, and of width

$$\Delta E_{\text{incoherent}} = 2E_o(\cot^2\theta_m \alpha_m^2 + \cot^2\theta_a \alpha_a^2)^{\frac{1}{2}} \quad . \qquad (1.19)$$

Scattering by the specimen convolutes the neutron wave vector distribution, and only for incoherent elastic scattering does equation (1.19) give the exact energy spread. If neutrons are scattered by phonons in the sample, the width of the scattered neutron group depends on the $\underline{q} - \omega$ relation of the sample through the one-phonon cross-section of equation (1.16). For Bragg scattering the neutron energy spread should be very small since, ideally, the neutron distribution is convoluted with a delta function. Finite sample mosaic spread causes deviations from this ideal case.

Equation (1.19) shows that the energy resolution may be

improved by reducing the collimator widths, ensuring that they still allow a reasonable number of neutrons to reach the sample and analyser. For our series of measurements it was found that α_m and α_a could be reduced to around 0.7° without serious loss of intensity. The value E_o should be kept as low as possible; the limit is usually fixed by having to choose λ_o so that there are negligible numbers of $\lambda_o/2$ neutrons in the beam incident on the monochromator. If germanium crystals are available for monochromator and analyser, second order contamination of the beams (may) be eliminated, and the upper limit on λ_o is determined by the Maxwellian distribution of neutrons from the reactor. Energy resolution is also improved by scattering neutrons from monochromator and analyser planes, which, at the chosen wavelength, give small values for $\cot \theta_m$ and $\cot \theta_a$, i.e. high index planes. The intensity of neutrons Bragg reflected from a ~~aluminium~~ monochromator decreases as the indices (h,k,ℓ) of the reflection increase, and decreasing collimation widths results in a further diminution of the neutron intensity after passing along the collimator. Thus, increased resolution is inevitably accompanied by a decrease in the number of neutrons reaching the detector, and the values of the parameters of equation (1.19) must be chosen to give good energy resolution while keeping counting times reasonable.

The design of the instrument reduces the monochromator and analyser planes available for Bragg scattering of neutrons of a given wavelength. For the PLUTO triple axis machine, which was used exclusively, θ_m and θ_a cannot exceed 55.5° and 54° respectively.

1.5 Focussing a Triple Axis Spectrometer

We have seen that there is a correlation between neutron wave number and direction of travel, at a particular setting of the machine, so that the number of neutrons falling on the analyser shows such a correlation, modified by scattering at the sample. The choice of machine parameters to correlate these effects so that the counting rate at the detector, N_D, is maximised is called focussing.

By considering, in turn, the effects on wave number and angular distribution of the neutrons scattered by monochromator, sample, and analyser, Collins[17] has obtained an expression for N_D when the machine is set up to observe scattering from a phonon in the sample. By computing N_D for various sets of machine parameters, the experimental conditions may be chosen to optimise N_D. Usually, collimation widths and mosaic spreads are fixed at values giving reasonable focussing over a whole range of experiments, and only d_m, d_a and E_o may be varied.

The approximate effect on the $\underline{K}$-space resolution caused by wave vector spread may be estimated. If neutrons at $d\theta_m$ to the optimum direction for Bragg scattering, θ_m, can reach the sample because of finite collimation, their wave vector spread is

$$d\underline{k}_o = (|\underline{k}_o| \cot\theta_m \, d\theta_m)\hat{\underline{k}}_o - |\underline{k}_o| \, d\theta_m \, \frac{d\hat{\underline{k}}_o}{d\theta_m}$$

$$= (|\underline{k}_o| \cot\theta_m \, d\theta_m \; ; \; |\underline{k}_o| \, d\theta_m) \quad . \qquad (1.20)$$

The first component lies along $\hat{\underline{k}}_o$, the second is perpendicular to $\hat{\underline{k}}_o$. Hence $d\underline{k}_o$ lies parallel to the monochromator planes from which the neutrons are scattered. This spread, small for large θ_m, is also proportional to wave number and collimation

width (through $d\theta_m$). For small θ_m, $d\underline{k}_o$ lies approximately along $\underline{k}_o$, but for large θ_m, $d\underline{k}_o$ will be almost perpendicular to $\underline{k}_o$. A similar spread occurs on reflection from the analyser. Mosaic spread η_m or η_a alters the lengths of $d\underline{k}_o$ and $d\underline{k}_1$, but we shall ignore this effect since η_m and η_a were always much smaller than α_m and α_a in our experiments.

The resolution function for given instrumental parameters may be estimated by convoluting the neutron wave vector spreads at monochromator and analyser. The resulting distribution should correspond to the distribution of elastically scattered intensity around a reciprocal lattice point, i.e. the 50% probability ellipsoid of the resolution function should be of the same shape as the contours $I = 0.5I_o$, say, obtained when the instrument is set with $E_o - E_1 = 0$ and $\underline{K}$ is varied around $\underline{K} = \underline{\tau}$. This is illustrated in Figure 1.2, which shows the rotation of the major axis of the resolution ellipse relative to the scattering vector, $\underline{K}$, for large θ_m and θ_a (corresponding to good energy resolution). The resolution ellipse has an eccentricity close to unity. If θ_m and θ_a are small, the ellipse becomes circular for large $\underline{K}$, and if small θ_m and θ_a are associated with large $\underline{k}_o$ and $\underline{k}_1$, the $\underline{K}$-space resolution will become poorer.

A convenient method by which the instrumental parameters, corresponding to focussing for phonon scattering, may be chosen has been presented by Peckham et al.[16]. This is the method which we have adopted for our measurement of phonons in naphthalene. The broadening of a phonon peak, caused by instrumental resolution, may be minimised by restricting $d\underline{k}_o$ so that all neutrons scattered by the sample in a particular direction have the same energy; i.e. differentiating eqs. (1.18) with respect to $\underline{k}_o$ and using

equation (1.1), we obtain the condition that

$$\underset{\underline{q}}{\text{grad}}\ \omega \cdot d\underline{k}_o = \hbar/m\ \underline{k}_o \cdot d\underline{k}_o \quad ; \quad \underline{d}_o \cdot d\underline{k}_o = 0$$

should be satisfied for all $d\underline{k}_o$. ($\underline{d}_o$ is the normal to the monochromator planes). This requires $(\frac{m}{\hbar} \underset{\underline{q}}{\text{grad}}\ \omega - \underline{k}_o)$ to be parallel to $\underline{d}_o$. Placing a similar restriction on $d\underline{k}_1$ requires $(\frac{m}{\hbar} \underset{\underline{q}}{\text{grad}}\ \omega - \underline{k}_1)$ to be parallel to $\underline{d}_1$. Perfect focussing occurs if these two conditions are satisfied simultaneously. Figure 1.3 shows these conditions in the form of a vector diagram in which the distance GD is zero under ideal focussing. The vectors OL, QL, OD and QD are varied to minimise GD by altering the instrumental parameters.

The width of a phonon peak also depends on the track in energy-momentum space followed in an individual scan. This width is a minimum when the track is normal to the phonon dispersion surface. In a 2-dimensional plot, such as Figure 3, this requires the track to be at right angles to the particular branch of the phonon dispersion curves. For a spectrometer operated in either the "constant-E" or "constant-$\underline{K}$" mode, we may only choose between a track parallel to the $\underline{q}$-axis or to the ω-axis. Thus it is unnecessary to consider this effect in any detail, but it may be pointed out that, if we wish to measure phonon frequencies in a particularly steep region of the dispersion curves, a "constant-E" scan is preferable to a "constant-$\underline{K}$" scan.

In Chapter 5 we show that it is important to consider instrumental energy resolution, and the distribution of Bragg intensity in $\underline{K}$-space before attempting to observe scattering from very low frequency modes in ferroelectrics and antiferroelectrics.

1.6 Spurious Peaks in the Scattered Neutron Count Rate

Various spurious processes can give peaks in N_D when a triple axis machine is set up to observe scattering from a phonon of wave vector $\underline{q}$ and energy $\hbar\omega(\underline{q}j)$. A neutron beam directed along $\underline{k}_1$, but of the same energy as the beam incident on the sample, may just give the correct conditions for Bragg scattering from the sample. If this beam is then inelastically scattered into the detector, a peak in N_D will occur. The intensity of this process is often of the same order of magnitude as for phonon scattering, although it is often considerably sharper in energy. A special case occurs when the machine is set to measure quasi-elastic scattering ($E_o - E_1 \approx 0$; $\underline{q}$ small). The spread in the neutron wave vectors may be sufficient for the scattering vector $\underline{K}$ (including experimental spread) to fall very close to the reciprocal lattice point being investigated. This means that neutrons Bragg scattered from the sample may be recorded in the detector after elastic scattering in the analyser. If $\underline{E}_o - E_1$ is increased from zero at small $\underline{q}$, N_D will peak and may be confused with scattering from an acoustic phonon. Usually this peak intensity is several orders of magnitude above that for typical phonons, and the position of the peak alters as the incident wavelength is changed. These properties should allow it to be distinguished from phonon peaks.

Higher order scattering at monochromator and/or analyser can cause spurious peaks if conditions such as

$$2\underline{k}_o - \underline{k}_1 = \underline{\tau}' + \underline{q}' \; ; \quad 4E_o - E_1 = \pm \hbar\omega(\underline{q}'j')$$

$$2\underline{k}_o - 3\underline{k}_1 = \underline{\tau}'' + \underline{q}'' \; ; \quad 4E_o - 9E_1 = \pm \hbar\omega(\underline{q}''j'')$$

are satisfied. The corresponding scattering diagrams are given in Figures 1.4a and 1.4b. Then scattering from a phonon $\underline{q}'$ of frequency $\omega(q'j')$ may be recorded. In particular, if $2\underline{k}_o - \underline{k}_1 = \underline{\tau}'$ and $4E_o - E_1 = 0$, then spurious Bragg scattering may occur with an intensity similar to that for phonons.

The second type of spurious process may be eliminated by using germanium analyser and monochromator, but this may not always be practicable. If it is not, then careful scattering diagrams must be drawn to ensure that peaks in N_D cannot be caused by spurious processes. Ideally, these considerations should be made before beginning measurements, to optimise useful output. However this may require the very quantities which are to be measured - the phonon frequencies.

1.7 The Operation of a Triple Axis Spectrometer

In a particular scan, there are six angles to be calculated. - the three arm positions, and the angles of the crystal tables. As the scan proceeds, arm 3 and table 3 are usually fixed, but the others are stepped to follow the chosen track in ω and $\underline{K}$. The operation of the machine must be at least partially computerised to cut experimental time.

The design and operation of the PLUTO triple axis spectrometer have been described in detail elsewhere[18,19,20]. We shall give an outline of its operation and point out its advantages. The machine is controlled by an on-line PDP-8 computer. Its zero angles - the angles of the arms when all are aligned parallel to the primary beam, and the table angles when the chosen planes, specified by d_m and d_a, lie along the incident

neutron beam- are measured at the start of the experiment. The specimen zero angle, defined as the setting when the x-axis of the sample is parallel to arm 1, is also obtained. To make these measurements, shaft angles may be typed directly into the computer and the "manual operating program" sets the shafts to the specified values.

The reactor neutrons have a broad energy spectrum and are scattered in all directions by the monochromator. The neutrons falling on specimen, analyser and detector must be restricted to those which have passed down the collimators in the three arms. Thus the monochromator and arm 1 must be heavily shielded, both for biological and scientific reasons. This shielding is in the form of a 3 ft. thick drum, around the monochromator, with six segments which may be raised individually to allow entry of the primary beam. The detector is also well shielded giving a total weight of detector and shielding which exceeds one ton, and is raised on air bearings when any shaft is to be moved. Once all six shafts have positioned, the air is turned off. The whole assembly moves on an accurately machined bed plate.

The type of scan required is chosen ("constant-K" or "constant-E") and the appropriate angle calculating program is called down from magnetic tape. The input to these programs consists of the machine parameters selected and details of the scan to be performed. These are listed in Table 1.1. Once the six angles for each step of the scan have been calculated, the shaft-driving program is called from tape and the scan executed. The shaft angles are measured by optical digitizers which allow a rotation of each shaft of greater than 655° before the digitizer output code loses its identity, and this has the advantage that the angles for each point in the scan are set up independently and cumulative positioning errors cannot occur. The six angles

may be read to 0.01^{o}. This corresponds to an accuracy of 1 in 10^{4} in the mean energy of the incident neutron beam, and at an average wavelength of 1$\overset{o}{A}$, $\underline{\tau} + \underline{q}$ may be obtained to an accuracy of 1 part in 10^{3}. This makes the machine particularly appropriate for automatic extended runs. A complete set of instructions allowing the machine to perform a set of scans, typically occupying 12 $\rightarrow$ 24 hours, may be punched on paper tape in a few minutes.

This method of control is extremely versatile. The results of one scan may be required to decide some of the details of the following scan, and were on-line control not available, there could be a significant delay before the shaft-angles of the new scan were available.

ACO - First lattice parameter (in $\mathring{A}$)

BCO - Second lattice parameter (in $\mathring{A}$)

DAN - Analyser plane spacing (in $\mathring{A}$)

UDM - Monochromator plane spacing (in $\mathring{A}$)

ZAN - Table 3 zero angle

VZM - Table 1 zero angle

GZ1 - Arm 1 zero angle

GZ2 - Arm 2 zero angle

GZ3 - Arm 3 zero angle

QOO - Table 2 zero angle

XQQ - Component of $\underline{K}$ along direction 1 (reduced units)

YQQ - Component of $\underline{K}$ along direction 2 (reduced units)

WAV = Average value of λ_o (in $\mathring{A}$)

LOW - $(E_o - E_1)$ for first point in scan

HIG - $(E_o - E_1)$ for last point in scan

STP - Energy step between consecutive points

KON - Specifies energy units

RXX - Step along first component of $\underline{K}$ (reduced units)

SYY - Step along second component of $\underline{K}$ (reduced units)

EGY - Value of $(E_1 - E_o)$ if "constant-E" scan

NOO - Number of steps in "constant-E" scan.

Table 1.1

Parameters required by Computer to calculate angles for an automatic scan.

Figure 1.1 Schematic Diagram of a Triple Axis Spectrometer (page 12)

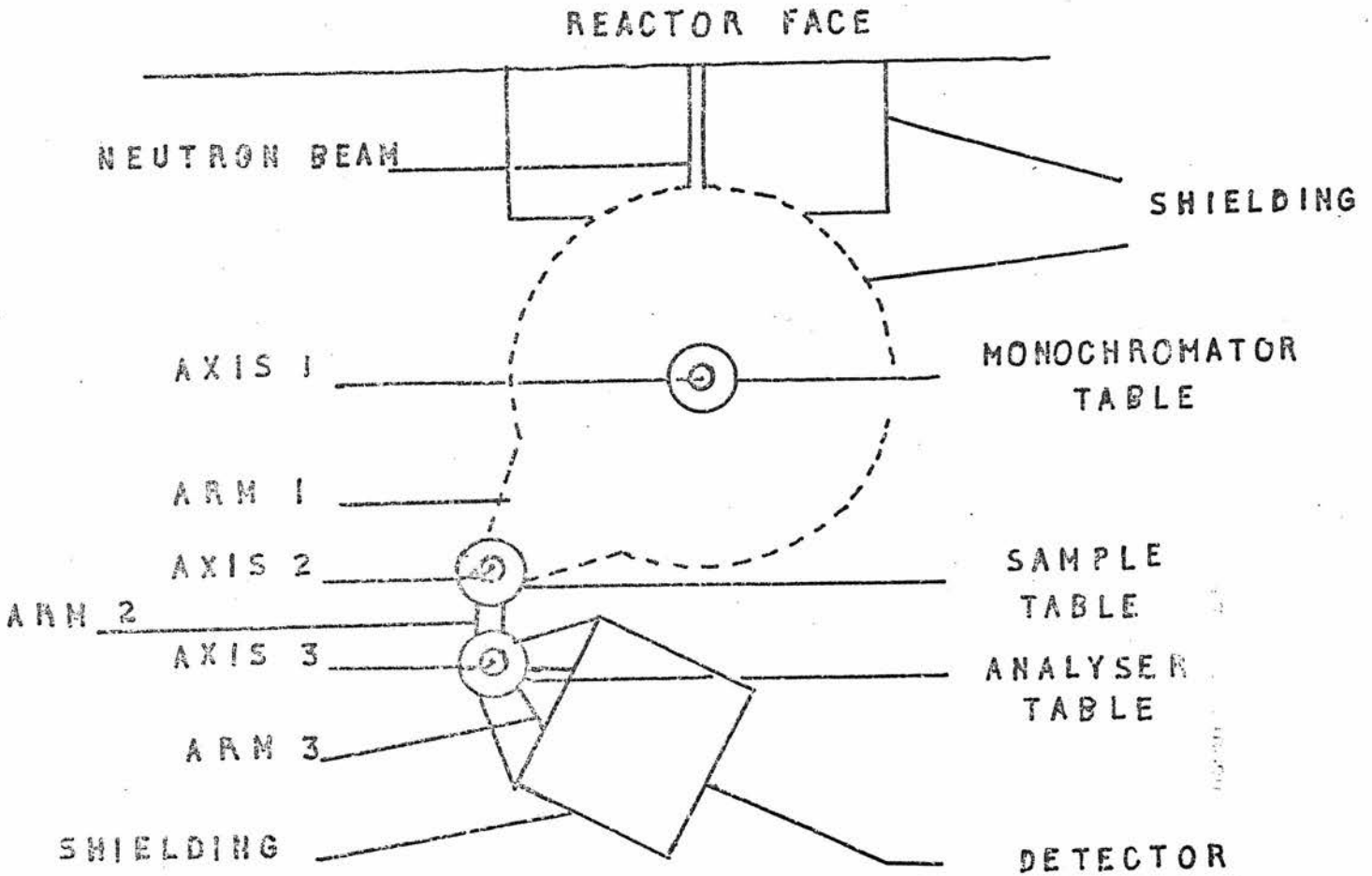
REACTOR FACE
NEUTRON BEAM
SHIELDING
AXIS 1
MONOCHROMATOR TABLE
ARM 1
AXIS 2
SAMPLE TABLE
ARM 2
AXIS 3
ANALYSER TABLE
ARM 3
SHIELDING
DETECTOR

FIGURE

1·1

Figure 1.2 Resolution Ellipse for Small and Large $\underline{K}$ (page 18)

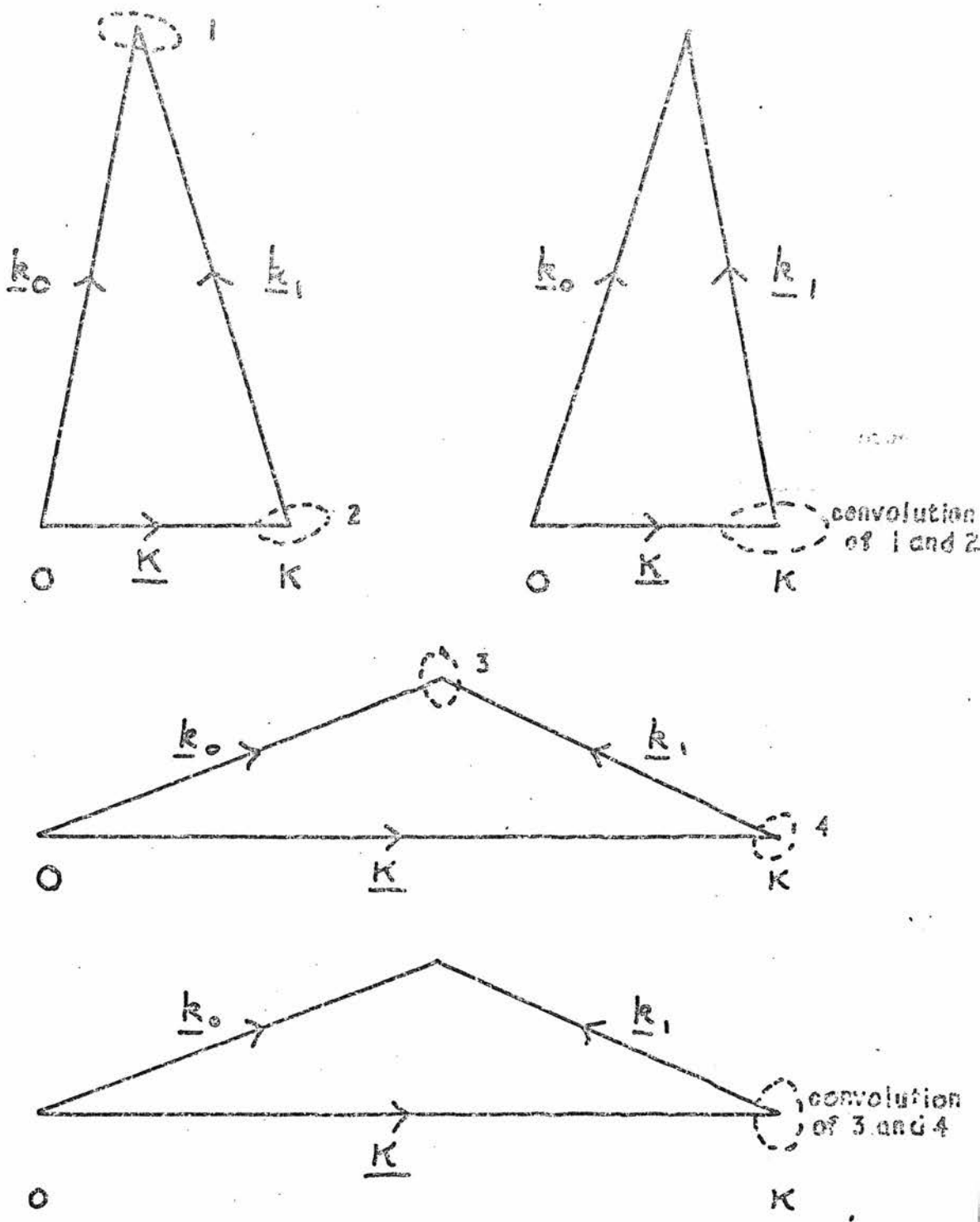

broken curve represents 50% probability

FIGURE

1·2

Figure 1.3 Vector Diagram Illustrating Focussing of a Triple Axis Spectrometer (page 19)

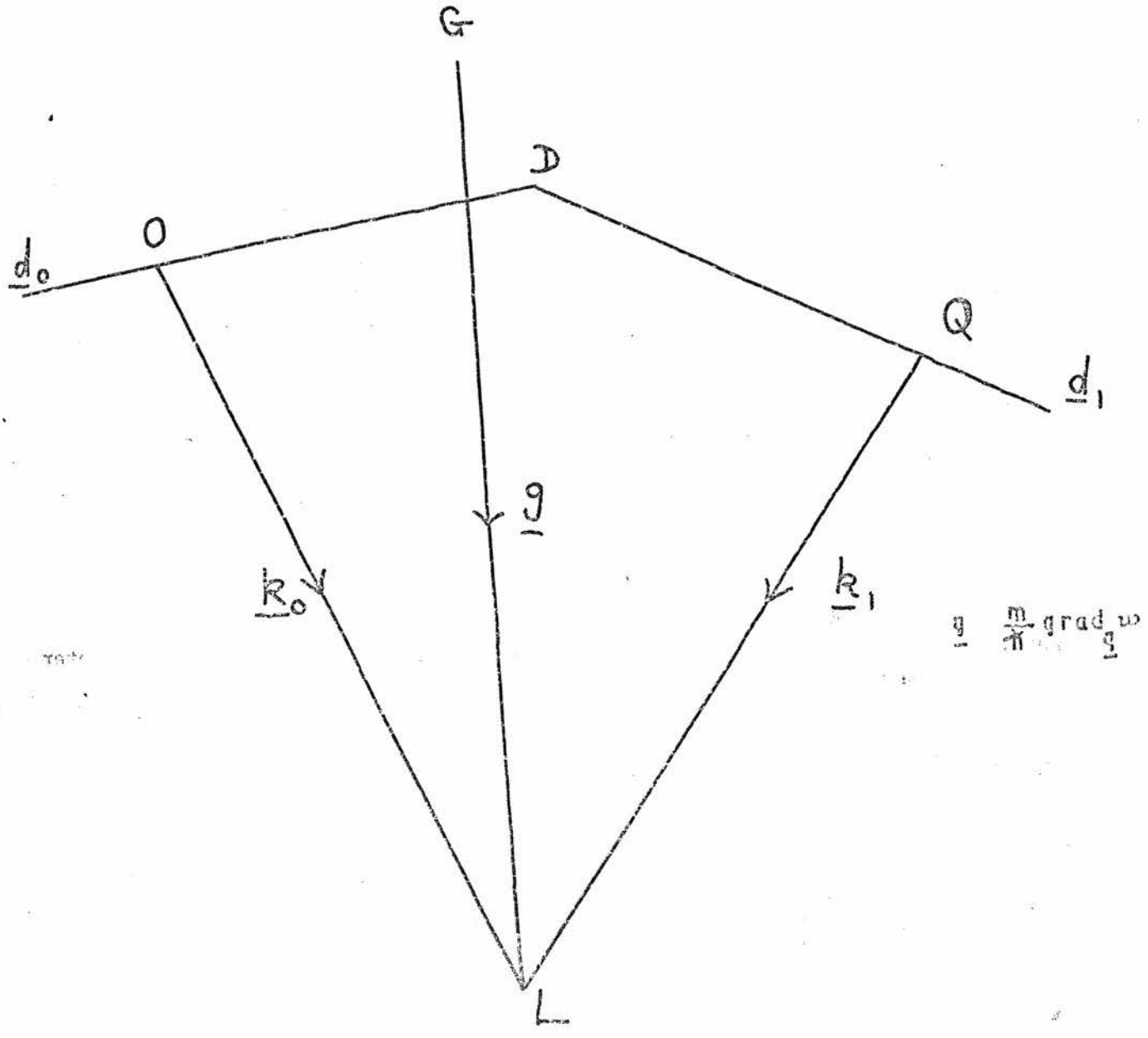

$\underline{g} = \frac{m}{\pi} \text{grad}_{\underline{g}_1} \omega$

FIGURE

1-3

Figure 1.4 Scattering Diagrams Illustrating the Formation of Spurious Peaks in the Scattered Neutron Count Rate of a Triple Axis Spectrometer (page 20)

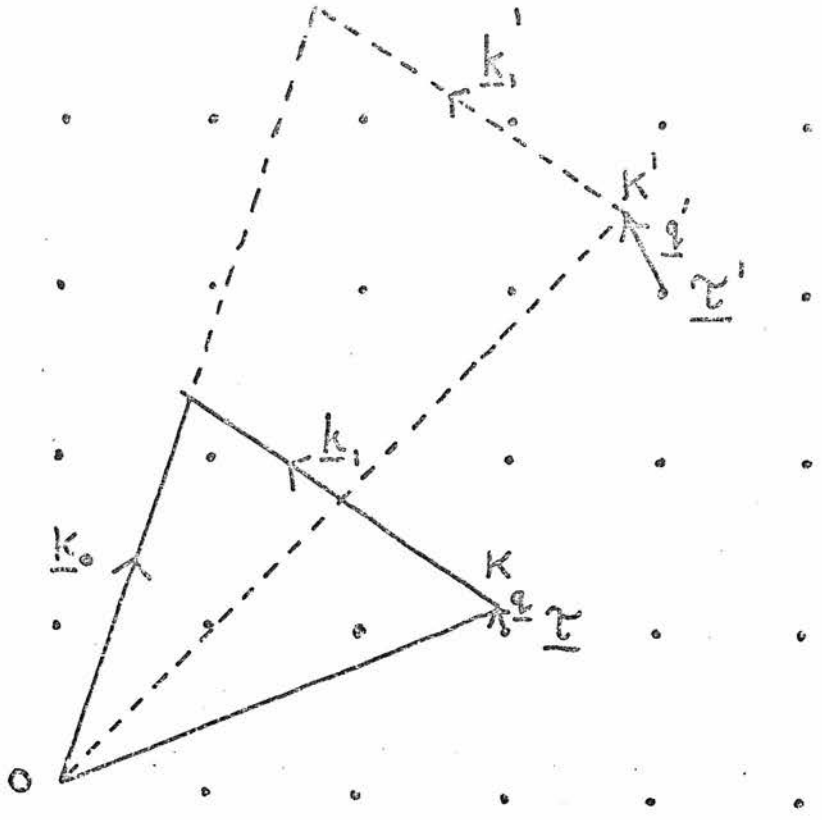

FIGURE 1·4a

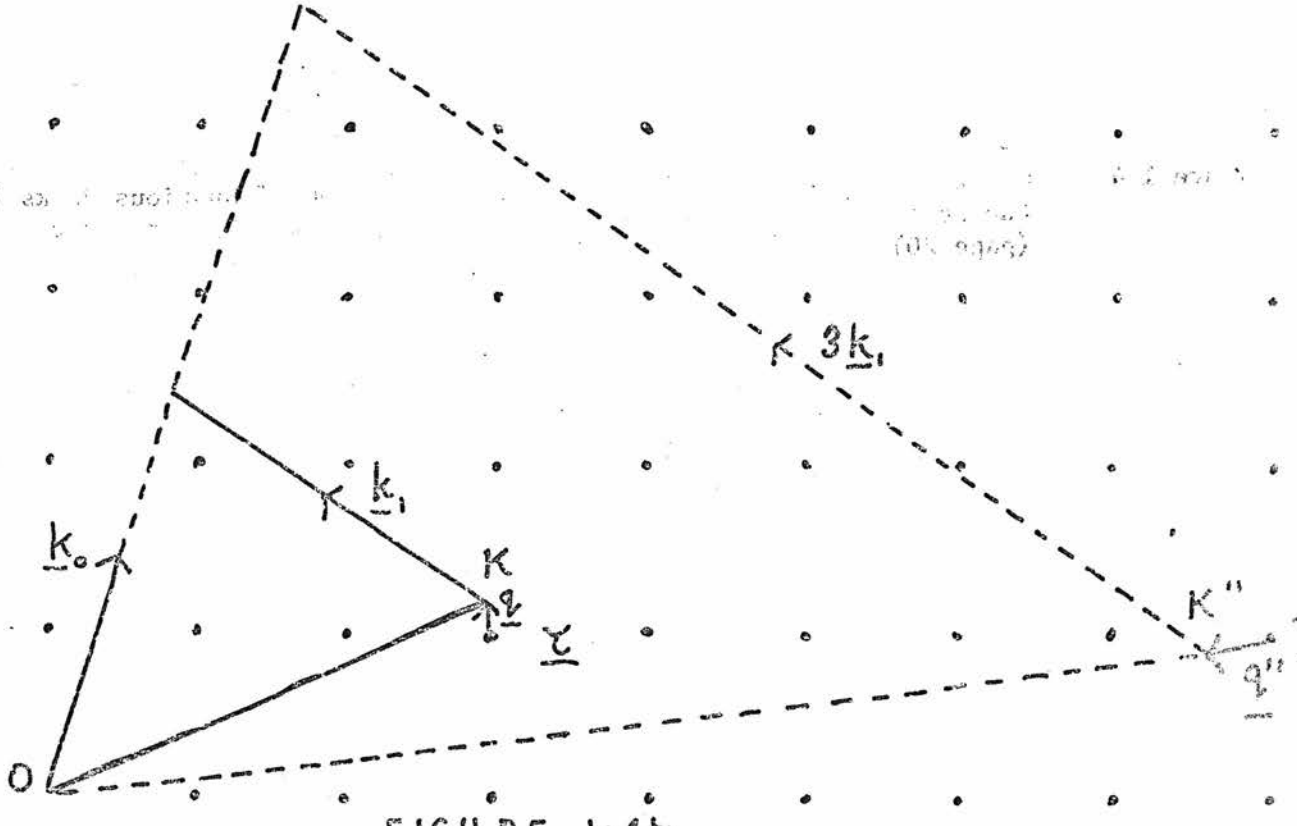

FIGURE 1·4b

CHAPTER 2

A NEUTRON DIFFRACTION STUDY OF PERDEUTERONAPHTHALENE

2.1 Introduction

In the past, several authors have presented refinements of the naphthalene crystal structure. Ahmed and Cruickshank[21] have refined the extensive data obtained by Abrahams, Robertson and White[22], and an extended refinement has been described by Cruickshank[23]. The data used were from X-Ray diffraction studies, and as the scattering factor is proportional to the atomic number, the carbon contribution is dominant. Therefore the hydrogen atoms could not be located accurately in this study.

The development of neutron scattering techniques now enables us to determine hydrogen nuclear positions in crystals, since the coherent neutron scattering length for hydrogen is comparable with that for many "heavy" atoms. However, one of the aims of the structural studies, to be described in this chapter, was to furnish us with the accurate position co-ordinates and cell dimensions required for work on the lattice dynamics of naphthalene. These inelastic scattering studies were to use a fully deuterated crystal, because of the large incoherent neutron scattering length for hydrogen. Hence, our elastic neutron scattering measurements were made on a crystal of deuterated naphthalene ($C_{10}D_8$).

2.2 The Structure Factor for Bragg Scattering of Neutrons

From general scattering theory (Chapter 1) the coherent part of the intensity of elastically scattered neutrons from a crystal unit cell depends on the function $|F_o(\underline{K})|^2$ where

$\underline{K}$, the scattering vector, is equal to a reciprocal lattice vector. $F_o(\underline{K})$ is the elastic structure factor,

$$F_o(\underline{K}) = \sum_k^{(b_k)} \exp(-W_k(\underline{K}))\exp(i\ \underline{K}.\underline{R}_k) \qquad (2.1)$$

where the summation is over all atoms in the unit cell; each atom is situated at $\underline{R}_k$, and has Debye-Waller factor, $\exp(-W_k(\underline{K}))$. The crystal symmetry simplifies the expression; in particular, for a crystal with a centre of symmetry, equation (2.1) reduces to

$$\sum_k 2b_k \exp(-W_k(\underline{K}))\cos(\underline{K}.\underline{R}_k)\ ,$$

where the summation, k, is taken over the asymmetric unit. The naphthalene crystal structure is monoclinic with space group $P2_1/c$, although the old convention, i.e. $P2_1/a$, is frequently used for naphthalene. There are two molecules in the unit cell - that at the origin (E-molecule) and the diad related one at $(0\ \tfrac{1}{2}\ \tfrac{1}{2})$ (D-molecule). The asymmetric unit is one half the E-molecule, and the crystal symmetry imposes restrictions on some structure factors. Using $P2_1/c$,

if $k+\ell = 2n$; $F_o(hk\ell) = F_o(h\bar{k}\bar{\ell})$; $F_o(\bar{h}k\ell) = F_o(hk\bar{\ell})$;

if $k+\ell = 2n+1$; $F_o(hk\ell) = -F_o(h\bar{k}\bar{\ell})$; $F_o(\bar{h}k\ell) = -F_o(hk\bar{\ell})$;

in the second case these relations imply that $F_o(\underline{K}) = 0$ if $h = \ell = 0$ or $k = 0$.

The Debye-Waller factors are, in general, anisotropic and may be written

$$\exp(-(b_{11}^{k'} h^2 + b_{22}^{k'} k^2 + b_{33}^{k'} \ell^2 + 2b_{12}^{k'} hk + 2b_{23}^{k'} k\ell + 2b_{13}^{k'} h\ell)) \qquad (2.2)$$

to take account of the thermal motion of the atoms in the

crystal. The structure factors are thus functions of the parameters we wish to determine, and by relating these F_o's to experimentally measured intensities, a least squares analysis will give the best values of the $\underline{R}_k$'s and b_{ij}^k's. Unfortunately it is $|F_o(\underline{K})|^2$ which determines the scattered intensity, i.e. phases (or in this case the signs), of the F_o's cannot be determined experimentally.

The results of Chapter 1 show that the scattered intensity for $|\underline{k}_o| = |\underline{k}_1|$ contains, in addition to coherent elastic scattering, contributions from incoherent elastic and thermal diffuse scattering. In Section 2.4 we discuss these effects in more detail.

2.3 Experimental Procedure

All measurements, to be described in this chapter, were made on a 7 mm diameter sphere, which had been cut from one end of a large single crystal of 98°/o deuterated naphthalene. This crystal was grown by Dr. J. Sherwood using the moving vessel technique[24]. The diffraction data were obtained on a Ferranti 4-circle diffractometer at the DIDO reactor at A.E.R.E., Harwell. This diffractometer, illustrated schematically in Fig. 2.1, has been described by Arndt and Willis[25], and was used in the moving crystal/moving detector mode.

Off-line computer operation was employed, the control tape being generated by an Atlas programme written by N.A. Curry. The angles for all four diffractometer shafts, which set the crystal on a Bragg reflection, are input for this programme, and a tape is generated which steps the shafts to give the required scan of the Bragg peak as detector output. The shaft-setting angles are calculated relative to the diffractometer datum

positions. These datum positions are necessary because the shaft-setting system is incremental. For two of the shafts the datum positions may be set by the experimenter, but the detector datum is set with the detector parallel to the neutron beam, incident on the specimen. The crystal table (Ω) is at datum when the χ-circle is aligned normal to the incident neutron beam, with the specimen between χ-circle and monochromator.

Since an X-Ray beam was totally absorbed in passing through our crystal, we used the back reflection technique to determine the crystal orientation. The crystal was then mounted, with $\underline{a}^*$ vertical, inside a soda-glass bulb to reduce sublimation losses during the experiment. The accurate alignment was then carried out on the four circle machine, to better than 0.05°.

The cell parameters for $C_{10}D_8$ were accurately determined by measuring the detector angle, $2\theta_B$, for several reflections along $\underline{a}^*$ $\underline{b}^*$ and $\underline{c}^*$, and using the relation

$$\frac{2\sin^2\theta_B}{\lambda^2} = h^2a^{*2} + k^2b^{*2} + \ell^2c^{*2} + 2h\ell a^*c^*\cos\beta^* .$$

The results are given in Table 2.1.

From these preliminary measurements, it was found that the crystal mosaic spread was 0.5° (F.W.H.M.), relative to an aluminium monochromator of small mosaic, and with fine instrumental collimation.

The Bragg intensity profile was measured by moving crystal table and detector in steps of $\theta : 2\theta$ with $\Delta\theta = 0.04^\circ$, from $\theta_B - 1.0^\circ$ to $\theta_B + 1.0^\circ$. In addition, the background was measured by scanning from $\theta_B - 2.0^\circ$ to $\theta_B - 1.0^\circ$ and from $\theta_B + 1.0^\circ$ to $\theta_B + 2.0^\circ$. In all reflections measured, the average

background counting rate had been reached at the extremities of the centre scan, i.e. there were no elastic intensity wings outside $\theta_B \pm 1^o$. The detector aperture was selected by choosing the smallest which gave the full integrated intensity for the reflections with large θ_B.

The reflections, to be measured, were divided into groups of eight separated by a standard reflection, (200) or (110). These standard reflections were a check on the crystal alignment and on the behaviour of the counting chains. After every two reflections all shafts were returned to datum, and so any cumulative errors in the shaft settings could be quickly recognised. A sequence of positioning orders was included after every four reflections, which was only executed if a machine positioning fault had been registered. This caused all shafts to be driven to their limit switches and then returned to datum.

331 independent reflections were measured at 295°K, additional scans giving 32 equivalent reflection pairs.

2.4 Determination of Structure Factors from Experimental Intensity Data

A typical intensity scan is illustrated in Figure 2.2. The general incoherent background was easily subtracted by interpolating between the two background scans. In most cases, the variation in $\underline{K}$ across the scan was so small that this background could be considered flat. The remaining intensity arises from elastic scattering and thermal diffuse scattering. The second contribution peaks at the reciprocal lattice point and consists of one, two and higher order phonon-scattered intensity, but is dominated by the contribution

from the one-phonon acoustic modes. The contribution from one-phonon scattering (first order thermal diffuse scattering) to experimental Bragg intensities depends on the type of scan used. The problem has been discussed, for cubic crystals, by Nilsson[26] who has obtained an explicit expression for the correction factor, $\alpha_{T.D.S.}$, for a moving crystal/stationary detector scan through the Bragg peak, assuming an infinite slit height. Cooper and Rouse[27] have extended Nilsson's treatment to include a moving crystal/moving detector scan ($w/2\theta$), and have avoided the assumption of an infinite slit. In a later paper, Cooper and Rouse[28] have extended their analysis and present methods and expressions which allow measured Bragg intensities to be corrected for first and second order thermal diffuse scattering in crystals of any symmetry. They also consider the effect of instrumental resolution on thermal diffuse intensities. For a crystal of low symmetry, the computation is considerable, but may be reduced by making certain assumptions about the acoustic mode velocities (for example, assuming them to be independent of direction of propagation in the crystal).

At the time of the data collection and subsequent structure refinement (Section 2.5), the results of reference (28) were not available. Using elastic constant measurements for $C_{10}H_8$, in conjunction with our phonon calculations of Chapter 3, applied to both $C_{10}H_8$ and $C_{10}D_8$, it should be possible to use the results of reference (28) to obtain a value for $\alpha_{T.D.S.}$ However it was anticipated that a considerably more accurate and more extensive set of Bragg intensity data would be obtained using a smaller crystal of $C_{10}D_8$. Thus we have not attempted to correct our present data for thermal diffuse scattering.

The total integrated intensity (I_{obs}) of each reflection,

i.e. the area under the intensity profile, was calculated by summing the areas of rectangles of height N_{Ti} and width W.

$$I_{obs} = \sum_i (N_{2i} - N_{1i}) \frac{W}{M_i} = \begin{matrix}\text{area under scan profile} \\ - \text{(background)}\end{matrix}$$

where W is the step-width, in this case 0.04°. M_i is proportional to the total number of neutrons from the monochromator which fall on the specimen while N_{2i} counts are recorded from the detector, and takes account of variations in counting time and reactor flux. The summation, i, is over all points in the scan. Usually N_{1i}, the background count, was independent of i, but of course varied with $(h^2 + k^2 + \ell^2)$.

The experimental Bragg intensity is then

$$I_B^{obs}(\underline{K}) = I_{obs}/(1 + \alpha) ,$$

where α is a correction factor.

This intensity has been measured by reflecting neutrons from a macroscopic crystal, and before it can be used to calculate the observed structure factor, $F^{obs}(\underline{K})$, certain corrections have to be made. The correction factors relate $I_B^{obs}(\underline{K})$ to the integrated intensity from a small element, δV, and include absorption, extinction, and Renninger effects.

Absorption

The intensity of any reflection is reduced by attenuation of the neutron beam in its path through the crystal. The corrected intensity is

$$I_B^A(\underline{K}) = I_B^{obs}(\underline{K}) \times \frac{V}{\int_V e^{-\mu x} dV} \qquad (2.3)$$

where x is the path length of the beam in the crystal for that particular reflection, μ is the linear absorption coefficient, and V is the crystal volume. μ was measured by finding the reduction in intensity of a neutron beam passing through a $C_{10}D_8$ crystal of thickness 1.5 cm. For a 98°/o deuterated crystal μ was 0.43 cm^{-1}.

For a spherical crystal, equation (2.3) is easily integrated for $\theta_B = 0^\circ$ and $\theta_B = 90^\circ$, and the values of $I_B^A/I_B^{obs} = A^*$ are tabulated in International Tables for X-Ray Crystallography Vol. II, pp. 302-5, in 5° intervals for various values of μR, R being the radius of the sphere. In our case, μR was 0.15 and A^* varied from 1.25 for $\theta = 0^\circ$ to 1.24 for $\theta = 90^\circ$. Jeffery and Rose[29] have shown that small deviations from a sphere can cause large uncertainties in A^*, a 2.5°/o uncertainty in R giving an uncertainty in A^* of 20°/o for $\mu R = 7.5$. However, for $\mu R = 0.15$, the uncertainty in A^* is $\lesssim$ 1.5°/o. Since we are only interested in relative values of intensity, the maximum difference in absorption correction between $\theta = 0^\circ$ and $\theta = 90^\circ$ is less than 1°/o of the intensity of any particular reflection. This is certainly considerably less than the experimental error, and we have neglected such corrections.

Extinction

Various authors, Zachariasen[30,31], Bacon and Lowde[32], and James[33] have published theoretical correction factors for extinction effects. However, for most cases, these cannot be calculated exactly. We thought that the mosaic spread of 0.5° was sufficiently large that extinction effects could be ignored in obtaining structure factors from the intensity data.

Our refinements therefore did not contain an extinction correction (but see Section 2.6).

Renninger Effect

This effect is a reduction in the intensity of the reflection from the crystal planes (h k ℓ), caused by simultaneous reflection of the incident and/or scattered neutron beam by other planes (h' k' ℓ'), (h" k" ℓ") etc. The condition for these additional reflections to occur is that the points (h' k' ℓ') etc. lie on the Ewald sphere as the sphere rotates about the line (0 0 0) to (h k ℓ). It is difficult to calculate the exact effect of all possible simultaneous processes, although approximate procedures have been developed for some restricted cases. One method is to select the azimuthal angle, ψ, to minimise the Renninger effect, and a programme has been written (Powell (1966)), to select the best value of ψ by varying the three crystal setting angles.

We now compute the values $|F^{obs}_{hk\ell}|^2$ from the integrated observed intensities. The $I^{obs}_B(\underline{K})$ will have been corrected, if necessary, for T.D.S., absorption, extinction, Renninger effect, and are the intensities expected from a large number of crystal blocks of volume δV. The total volume of these blocks is that of the sample , i.e. V. Then, from the results of Buerger[34], which we quote without proof,

$$I_B(\underline{K}) = \int Q\delta V \quad \text{where} \quad Q = N_c^2\lambda^3 L p |F_{hk\ell}|^2 \ .$$

$F_{hk\ell}$ = calculated structure factor.

N_c = number of cells per unit volume.

L = Lorentz factor.

p = polarisation factor .

N_c and λ are fixed in a particular diffraction experiment,

but L and p may vary with $\underline{K}$, so

$$I_B(\underline{K}) = cLp \left| F_{hk\ell}^{calc} \right|^2 \quad . \qquad (2.4)$$

The observed structure factors are to be compared with the calculated. It is convenient to correct the $F_{hk\ell}^{obs}$ for Lorentz and polarization factors, then it remains to determine the scale factor relating $F_{hk\ell}^{obs}$ and $F_{hk\ell}^{calc}$. c may be found as a parameter in the refinement, but an experimental value is useful in detecting extinction effects and in correctly estimating the thermal parameters (obviously c and b_{ij}^k's are correlated).

The Lorentz factor, which allows for the different times taken for different reciprocal lattice points to sweep through the reflecting sphere, is

$$L = \frac{1}{\sin 2\theta_B}$$

for the geometrical conditions of our experiment (normal-beam equatorial geometry). For neutrons, p = 1 as there is no polarization effect. Then

$$\left| F_{hk\ell}^{obs} \right| = (I_B^{obs}(\underline{K}))^{1/2} \sqrt{\sin 2\theta_B} \qquad (2.5)$$

and $\Sigma \left| F_{hk\ell}^{obs} \right| = s \Sigma \left| F_{hk\ell}^{calc} \right|$, where s is a scale factor.

Determination of Scale Factor from a Wilson Plot

The statistical result (Wilson[35])

$$\langle |F_{hk\ell}|^2 \rangle = \sum_{i=1}^{N} f_i^2 \quad , \quad \text{with } f_i \text{ the scattering factor,}$$

is used. The f_i should be corrected for thermal effects, but these are constant over a small range of $\sin\theta/\lambda$, and the

constants c' in each range may be found from

$$c'\langle |F_{hk\ell}^{obs}|^2 \rangle = \sum_i (f_i')^2 \qquad (2.6)$$

with f_i' the theoretical scattering lengths with no Debye-Waller factor included. Equation (2.6) with the mean values of $|F_{hk\ell}^{obs}|^2$ over a small range of $\sin\theta$, then gives c' and a plot of $\ell n(c')$ against $\sin^2\theta/\lambda^2$ has $\ell n(\frac{1}{s^2})$ as its intercept at $\sin\theta/\lambda = 0$. We obtained a value of s between 600 and 500.

Since this calculation was highly inaccurate (possibly because not all reflections in a given range of $\sin\theta/\lambda$ were included, there being a tendency to measure the stronger reflections only), it was decided to estimate s as a parameter in the least-squares refinement. Omitting some weak reflections in each range of $\sin\theta/\lambda$ would give s too high a value.

Using equation (2.5), the $|F_{hk\ell}^{obs}|$ were calculated and their values are listed in Table 2.2. The standard deviations $\sigma(F)$ were calculated from the deviations of the integrated intensities

$$\sigma(I) = \sum_i (\sigma_{1i}^2 + \sigma_{2i}^2)^{1/2} ,$$

where σ_{1i} and σ_{2i} are $(N_{1i})^{1/2}$ and $(N_{2i})^{1/2}$ respectively.

The observed structure factors of the standards, (200) and (110), were distributed about their average values of 1392 and 1125 with (standard) deviation well below $\sigma(F)$. Figure 2.3 shows the histogram for (200). The 32 equivalent pairs had F's which had an average agreement of 1%; for all but three pairs, the F's agreed within the standard deviations.

2.5 The Structure Refinement

To determine the nuclear positions and thermal parameters in the $C_{10}D_8$ crystal, we performed a least squares refinement in which the function

$$\mathcal{R}' = \sum_{hk\ell} (|F^{obs}_{hk\ell}| - |F^{calc}_{hk\ell}|)^2$$

is minimised, by varying the parameters used to obtain $F^{calc}_{hk\ell}$. From Section 2.2 we see that, in general, these parameters consist of a scattering length b_k, three positional parameters, $(X_k\ Y_k\ Z_k)$ and six anisotropic temperature factors b^k_{ij} for each atom, k, in the unit cell. The six b^k_{ij} are from a harmonic theory, and in all that follows we shall ignore any anharmonic contributions to the temperature factors. For $C_{10}D_8$, this gives a total of 81 parameters to be determined in addition to the scale factor, s, (in our case the b_k's are known). All our refinements were based on unit weights.

The number of variable parameters may be reduced by applying constraints to the system. In the course of our refinement we have imposed various constraints and performed statistical tests to decide whether or not the removal of these constraints represents a better fit to the experimental data.

2.5.1 The Rigid-Body Thermal Motion Constraint

The first constraint imposed was that the internal molecular vibrations in $C_{10}D_8$ could be ignored compared with those caused by the molecule performing rigid-body thermal motions. This was discussed by Cruickshank[36], and

a least squares programme incorporating these constraints has been written (Pawley (37)). Under this constraint it has been shown that

$$F_o(\underline{K}) = c \sum_k b_k \exp(2\pi i\, \underline{Q}.\underline{R}_k)\exp(-\underline{h}.\underline{A}^{-1}\left\{\underline{T}+\underline{V}_k.\underline{L}.\underline{\tilde{V}}_k\right\}\underline{\tilde{A}}^{-1}.\underline{\tilde{h}}) \qquad (2.6')$$

where $\underline{h} = (h,k,\ell)$; $\underline{X}_k = \underline{A}.\underline{R}_k$ expresses the transformation from fractional co-ordinates to an orthogonal system in ^{o}A.

$$\underline{V}_k = \begin{bmatrix} 0 & -Z_k & Y_k \\ Z_k & 0 & -X_k \\ -Y_k & X_k & 0 \end{bmatrix} \text{, and}$$

$\underline{T}$ is the mean square translational tensor

$\underline{L}$ is the mean square rotational tensor.

The second exponential in (2.6') replaces the conventional $\exp(-\underline{h}.\underline{\beta}.\underline{\tilde{h}})$ where

$$\underline{\beta} = \begin{bmatrix} b_{11} & b_{12} & b_{13} \\ b_{12} & b_{22} & b_{23} \\ b_{13} & b_{23} & b_{33} \end{bmatrix} .$$

Imposing the rigid body constraint reduces the 54 thermal parameters in $C_{10}D_8$ to twelve, since $\underline{T}$ and $\underline{L}$ are symmetric second-rank tensors.

Using the rigid body thermal parameter constraint programme, with the initial parameters taken from the results of Cruickshank's refinement of the X-Ray data on $C_{10}H_8$, we obtained, after refinement, an R-factor of 5.3°/o, which fell to 5.1°/o when the deuterium scattering length was reduced to 0.63 to allow for the presence of the 2°/o hydrogen in the crystal. This R-factor is

$$R = \sum_{hk\ell} \left| \left| F_{hk\ell}^{obs} \right| - \left| F_{hk\ell}^{calc} \right| \right| \Big/ \sum_{hk\ell} \left| F_{hk\ell}^{obs} \right| .$$

(under $\bar{1}$ symmetry)

In Table 2.3 we list the fractional atomic co-ordinates and the thermal parameters obtained in the R.B.T.P.* refinement. These thermal parameters were calculated from the fractional co-ordinates and the $\underline{T}$ and $\underline{L}$ tensors of the refinement where

$$\underline{T} = \begin{bmatrix} 4.84 & 0.20 & -0.09 \\ & 2.92 & -0.06 \\ & & 2.29 \end{bmatrix}; \quad \sigma(\underline{T}) = \begin{bmatrix} 0.09 & 0.06 & 0.08 \\ & 0.08 & 0.08 \\ & & 0.15 \end{bmatrix}$$

both in $\mathring{A}^2 \times 10^{-2}$.

$$\underline{L} = \begin{bmatrix} 31.59 & -3.49 & 0.11 \\ & 18.45 & -1.16 \\ & & 19.12 \end{bmatrix};$$

$$\sigma(\underline{L}) = \begin{bmatrix} 1.98 & 0.78 & 1.05 \\ . & 0.93 & 0.73 \\ & & 0.85 \end{bmatrix}$$

both in deg^2. $\underline{T}$ and $\underline{L}$ are in molecular inertial system.

2.5.2 Discussion of R.B.T.P.* Constrained Refinement

In considering the results of Section 2.5.1 it is often instructive to compare them with those of Cruickshank's refinement of the X-Ray data for $C_{10}H_8$, which are included in our tables of results. It must be remembered, however, that Cruickshank inserted the hydrogens at 1.09$\mathring{A}$ from the carbons and assumed isotropic hydrogen temperature factors, whereas our refinement located the deuteriums and allowed anisotropic b_{ij}'s, although the latter were deduced from the rigid body

* Rigid Body Thermal Motion (Parameter)

$\underline{T}$ and $\underline{L}$. The atomic co-ordinates from neutron diffraction correspond to the nuclear positions, whereas X-Ray diffraction locates the centroid of the atomic electron cloud.

From the $C_{10}D_8$ bond lengths, given in Figure 2.4, we see that the lengths of the bonds C_A-C_B and C_B - C_C differ considerably and that the C-D bonds are all of length $(1.078 \pm 0.005)\overset{\circ}{A}$. These differences in C-C bond length are consistent with Cruickshank's results, and there is no evidence that the X-Ray determined bonds are significantly shorter than those determined by neutrons. The carbon ring bond angles agree with those in $C_{10}H_8$ in showing deviations from 120°, and our results indicate that the C-D bonds do not bisect the angle between the neighbouring C-C bonds.

Table 2.4 lists the atomic co-ordinates in the molecular inertia system, a finite Z-co-ordinate indicates a deviation from the plane perpendicular to the axis of greatest inertia. We see that the carbon atom deviations are of the order of one standard deviation, and D_A and D_E have displacements of two standard deviations. These may possibly be significant and this point is discussed in Section 2.5.3. Cruickshank has calculated that the shortest intermolecular distance in $C_{10}H_8$ is $H_A(0,0,0) \rightarrow H_B(\frac{1}{2},-\frac{1}{2},1)$ $(2.40\overset{\circ}{A})$, and the next shortest is $H_A(0,0,0) \rightarrow H_E(0,0,1)$ $(2.66\overset{\circ}{A})$, i.e. they involve the atoms which show deviations from the mean molecular plane. For $C_{10}D_8$, from the co-ordinates of Table 2.4, these distances are $2.42\overset{\circ}{A}$ and $2.65\overset{\circ}{A}$.

The $\underline{T}$ and $\underline{L}$ matrices for $C_{10}D_8$ are seen to be closely diagonal, showing that their principal axes almost coincide with the molecular axes. The b_{ij}'s of Table 2.3, deduced from $\underline{T}$ and $\underline{L}$ are related to Cruickshank's U_{ij}^{obs}'s (U_{ij}^{Cr})

as follows:-

$$b_{ij} = 2\pi^2 a_i^* a_j^* U_{ij}^{Cr}$$

where $a_1^* = a^*$, $a_2^* = b^*$; $a_3^* = c^*$

except that the U_{ij}^{Cr} were found from an unconstrained refinement and hence contain contributions from internal modes, whereas our b_{ij}'s were deduced from $\underline{T}$ and $\underline{L}$ and contain rigid body displacements and a restricted average of the internal mode displacements. The separate atomic mean square displacements may be found from the U_{ij}'s, and these are listed in Table 2.5.

$$(\overline{u_k^2})_{\text{Cruickshank}} = (\overline{u_k^2})_{\text{rigid-body}} + (\overline{u_k^2})_{\text{internal modes}}.$$

The second term has been calculated for carbon atoms in $C_{10}H_8$ by Higgs[38], and has been shown to be small compared with $(\overline{u_k^2})_{\text{Cruickshank}}$, i.e. the $\underline{T}$ and $\underline{L}$ deduced from the carbon U_{ij}^{Cr}, uncorrected for internal vibrations, may satisfactorily be used to discuss the rigid body motion of the $C_{10}H_8$ molecule.

If the principal axes of $\underline{T}$ and $\underline{L}$ coincide with the molecular axes, we may deduce the frequencies of vibrations about these axes from the diagonal elements of $\underline{L}$, using

$$(\text{mean square amplitude})\ \text{rad}^2 = \frac{h}{8\pi^2 I}\left\{\frac{1}{\nu}\coth\left(\tfrac{1}{2}\frac{h\nu}{kT}\right)\right\}$$

which, for $h\nu \ll kT$, reduces to

$$\omega_{ii}\ (\text{in rad}^2) = \frac{kT}{8\pi^2 I_i \nu_i^2} \qquad (2.7)$$

where I_i and ν_i are the moment of inertia and frequency for angular oscillations about axis i. These ν_i are not necessarily the average of the symmetric and anti-symmetric

Raman frequencies, since Raman molecular modes are not always oscillations about these axes. Also, the Raman measurements give the frequency for a mode with wave vector at the zone centre, whereas equation (2.7) gives an average of the frequencies for wave vectors over the whole Brillouin zone. Pawley[39] has shown that his model for the lattice dynamics of naphthalene predicts Raman modes in which the molecule oscillates about axes tilted at up to 30° to the molecular axes. The work on the phonon dispersion curves for $C_{10}D_8$ (Chapter 3) shows that for $0 \leqslant |\underline{q}| \leqslant 0.5$ in the direction $[0\ 1\ 0]$, the variation in frequency of the Raman active modes can be as much as 30%, for at least the higher branches. Our results from the refinement of Section 2.5.1 give $(63.5, 105.2, 41.3)\text{cm}^{-1}$ for the ν_i of equation (2.7). If the off-diagonal terms of $\underline{L}$ are significantly different from zero, the ν_i will differ slightly from the frequencies for oscillations exactly about the molecular axes.

2.5.3 Refinement under mmm Symmetry Constraint

A structure refinement was performed with the $C_{10}D_8$ molecule constrained to full mmm symmetry but with the b_{ij}'s fixed at the values of Table 2.3. This refinement was performed on the Edinburgh KDF9. We were unable to vary the b_{ij}'s because of the limited computer store. Later we were able to use the S.R.C. Atlas computer at Chilton to perform refinements requiring a larger computer store. The number of position parameters was only 12, namely two position coordinates for each of the atoms C_A, C_B, D_A, D_B, one coordinate for C_C and three Euler angles which determine the orientation of the molecular plane. Under this symmetry

constraint the best R-factor obtained was 5.15°/o. The R-factor with this symmetry constraint relaxed (i.e. that of Section 2.5.1) showed no significant improvement on the 25°/o level of the F-distribution. Hence the deviations of atoms C_B, C_D, D_A and D_E discussed in Section 2.5.2 do not appear to be statistically significant. The atom co-ordinates obtained under the symmetry constrained refinement are listed in Table 2.3, and the corresponding calculated structure factors are given in Table 2.2.

2.5.4 Refinement under Further Molecular Symmetry Constraint

To test the significance of the differences in bond lengths and angles found in the rigid body refinement, a further constrained refinement was carried out. The carbon rings were constrained to perfect hexagons with the direction of the C-D bonds at 120° to the neighbouring sides of the hexagon. These two bond lengths along with the three Euler angles are the only parameters necessary to determine the atomic positions. With the b_{ij}'s fixed at their values from the rigid body refinement the best R value was 6°/o, which only fell to 5.8°/o when the b_{ij}'s were allowed to vary independently. These are poorer than all other values so far obtained, on the 2°/o level of the F-distribution and we may attach high significance to the variation in bond lengths and angles.

2.5.5 The Correlation Matrix

The rigid body constrained refinement gave a final correlation matrix with some interesting properties. The only positional parameters which showed significant correlation

were x and z co-ordinates of the same atom, which indicates for the system of axes chosen, uncertainty in orientating the molecule. There was a high correlation between elements of $\underline{T}$ and $\underline{L}$, namely T_{11} and L_{22}/L_{33} ; T_{22} and L_{11} ; T_{13} and L_{13} ; T_{12} and L_{12}, which is not surprising when one considers the equations linking the U_{ij} to T_{ij} and L_{ij}, Cruickshank[40]. Using the present set of axes these become:-

$$U_{11} = T_{11} + x^2L_{22} + y^2L_{33} - 2xyL_{23} \quad (2.8a)$$

$$U_{22} = T_{22} + x^2L_{11} \quad (2.8b)$$

$$U_{33} = T_{33} + y^2L_{11} \quad (2.8c)$$

$$U_{12} = T_{12} - x^2L_{12} + xyL_{13} \quad (2.8d)$$

$$U_{13} = T_{13} - y^2L_{13} + xyL_{12} \quad (2.8e)$$

$$U_{23} = T_{23} - xyL_{11} \quad (2.8f)$$

where the U_{ij}, x, y refer to a particular atom, k. Equation (2.8b), for example, indicates that it is difficult to distinguish translational motions along axis 2 from librations about axis 1.

2.6 Further Refinements of Neutron Diffraction Data

Since our refinements, described above, and reported in the literature, (Pawley and Yeats[41]), others have used our data to obtain some very interesting results.

Speakman (1969) (private communication) has performed an unconstrained refinement with 82 parameters, and including a weighting scheme, to take some account of extinction. This

scheme set $\sqrt{w_i} = \frac{|F^{obs}|_i}{p}$ for $|F^{obs}|_i < p$ and $\sqrt{w_i} = p/|F^{obs}|_i$ for $|F^{obs}|_i > p$, with $p = 290$, on our structure factor scale, i.e. the strong reflections where extinction was more likely to occur, were given lower weight than the weak ones. $R'_W = \frac{\sum w_i (|F^{obs}|_i - |F^{calc}|_i)^2}{\sum w_i |F^{obs}_i|^2}$ was minimised, and the conventional R-value was 3.9°/o. The corresponding positional co-ordinates were in satisfactory agreement with ours, and the calculated F's had the same signs as our F's, i.e. this refinement found the same minimum. Speakman reported that introducing the deuterium scattering length as an additional parameter gave no significant improvement on his unconstrained R-value, and concluded that there was no evidence for incomplete deuteration in the observational data. He has used our data to compute the neutron-scattering density in the mean molecular plane, and this plot is included as Figure 2.5.

Pawley (1970) (private communication) has repeated the refinement of Section 2.5.1, using Speakman's weighting scheme to obtain $R'_W = 12.3$ % with $R = 5.1$°/o, showing that this does not lead to any improvement in the constrained refinement. Pawley then considered an extinction correction which has been described by Zachariasen[31] (see Duckworth, Willis and Pawley,[42]). For a spherical crystal:-

$$F_{obs}^{incorr} = F_{obs}^{corr} \left[(1 + x^2)^{1/2} - x \right]^{1/2}$$

where $x = c \ (F_{obs}^{incorr})^2 \ \text{cosec}\ 2\theta$

$F_{obs}^{incorr} = F^{obs}$, *uncorrected for extinction*,

and c is a constant, which is determined as a parameter of the refinement. With this additional parameter, R fell to

4.4°/o and R'_W was 9.88 %, a highly significant drop. With the rigid body thermal constraint relaxed, R was 3.5°/o, R'_W 6.12 % for 68 parameters, and a completely unconstrained refinement (83 parameters) gave an R of 3.3°/o and an R'_W of 5.26 %.

These results showed that the thermal motion of $C_{10}D_8$ could not be adequately described by the twelve "rigid body" thermal parameters, and that displacements due to internal modes could not be neglected. The improvement in R from 4.4°/o to 3.5°/o required an increase in the number of parameters from 26 to 68, i.e. 42 extra parameters to take account of atomic displacements under internal modes; and it is of interest to know if all those are "good" parameters. Perhaps these mode displacements may be adequately described by a small number of parameters, having physical significance. The deuterium atoms, are likely to have considerably larger displacements than the carbon atoms, by virtue of their positions in the molecule and because of their small mass (the mean square displacements depend on $\frac{1}{m}$). Pawley[43] has introduced a single deuterium isotropic temperature factor, (B), to describe their internal mode thermal displacements, and obtains R = 4°/o, R'_W = 7.6 % with B = 0.0063A^{o2}. This agrees satisfactorily with Johnson's calculations on benzene[44a], where the difference in carbon and hydrogen mean square displacements was 0.0126A^{o2} (this would predict B = 0.0057A^{o2} with hydrogens replaced by deuterium). This benzene work showed that the motion was highly anisotropic and so Pawley replaced the isotropic B by anisotropic temperature factors, β_i, the same for all deuteriums, corresponding to squared displacements along the C-D bond, across the bond, and out of the molecular plane, to obtain an R value of 3.3°/o. This

refinement relaxed the mmm symmetry constraint, but gave just as good a fit to the data as the completely unconstrained refinement. Hence the thermal motion could be described as well by 12 rigid body parameters with 3 internal mode deuterium thermal parameters as by 54 independent anisotropic thermal parameters. Values of β_i were 0.005, 0.008 and $0.021\text{A}^{\circ 2}$, compared with calculated values for deuterated benzene of 0.002, 0.006 and $0.010\text{A}^{\circ 2}$. (44a)

2.7 Discussion

The results described in this chapter, bring out the value of performing constrained refinements, and show that they may be used as tests of the significance of various deductions. We must distinguish between statistical significance and physical significance - Pawley points out that the change in R from 3.3°/o to 3.5°/o, on imposing an mmm symmetry constraint on an otherwise unconstrained molecule is statistically significant on the 0.01 probability level, but its physical significance cannot be decided until similar results have been collected for many other solid, aromatic hydrocarbons. However, the breaking of the rigid body thermal constraint may be assumed to have physical significance, in view of the satisfactory description of the additional atomic thermal motion.

There appears to be good agreement between calculations of $\overline{u^2}_{int}$ on benzene and naphthalene. Spectroscopic data on benzene predicts values of $0.0139\text{A}^{\circ 2}$ for hydrogen and $0.0013\text{A}^{\circ 2}$ for carbon, whereas Higgs has obtained values of $0.0013 - 0.0020\text{A}^{\circ 2}$ for carbon in $C_{10}H_8$, from force-field

calculations. We might imagine that this positional variation of mean square displacement might be reflected in the deuterium motion, but this is not indicated by the neutron results.

Our earlier refinements, showing a significant decrease in the deuterium scattering length, are now seen to have indicated not incomplete deuteration, but a deviation from the rigid-body thermal motion model. Including the additional deuterium isotropic B, is mathematically approximately equivalent to giving that atom a $\underline{K}$-dependent scattering length, and our value of 0.63 was simply its average over the range of experimental measurements. This is now consistent with Speakman's conclusions on incomplete deuteration - he performed an unconstrained refinement, in which the anisotropic temperature factors contained the apparent $\underline{K}$-dependence of b_D.

An important fact to emerge from the subsequent refinements is that our data was affected by extinction, although this was not at all obvious on analysing our results. Of the 25 strong reflections, 11 had $|F_{obs}| > |F_{calc}|$, and 11 had $|F_{obs}| < |F_{calc}|$, with the remaining three agreeing within experimental error. We now realise that the θ-dependence of extinction effects is important, and makes the effect difficult to analyse. This is perhaps a cautionary tale - extinction correction parameters should be included in a structure refinement, and a weighting factor which is only intensity-dependent is no substitute.

One rather interesting fact may be seen on comparing the many constrained refinements (summarized in Table 2.6). Increasing the number of parameters does not always improve the fit, what is important is to choose "good" or significant

parameters. For example, increasing the number of parameters from 25 to 26 by including an extinction correction gave $\frac{R'_W(25)}{R'_W(26)} = 1.25$, compared with a ratio of 1.016 on the 0.1°/o probability level, showing that the extinction parameter is a highly significant parameter. Similarly, the 27 parameter fit gave an R'_W ratio of 1.3, again to be compared with 1.016 for the 0.1°/o probability level. Model VI with 44 parameters gave the same R-value as model V which had 83 parameters, and a statistically better fit than the 68 parameter model IV.

a	=	8.266	±	0.008 Å	a^*	=	0.1447 $Å^{-1}$	
b	=	5.968	±	0.006 Å	b^*	=	0.1666 $Å^{-1}$	
c	=	8.669	±	0.008 Å	c^*	=	0.1376 $Å^{-1}$	
β	=	122.92	±	0.02°	β^*	=	57.08	± 0.2°

Direct and Reciprocal Space Cell Parameters for $C_{10}D_8$ at 295°K.

TABLE 2.1

0	0	2	353	315	292
0	0	3	1312	1301	1296
0	0	4	1330	1301	1294
0	0	5	357	326	344
0	0	7	350	289	316
0	1	1	135	115	112
0	1	3	622	588	583
0	1	4	682	662	638
0	1	5	265	303	295
0	1	7	265	225	239
0	1	8	92	83	91
0	2	0	739	672	678
0	2	1	482	427	439
0	2	2	958	893	908
0	2	6	672	689	691
0	2	7	164	165	157
0	3	1	756	732	728
0	3	3	606	567	577
0	3	4	321	305	326
0	3	5	497	476	470
0	4	1	537	511	513
0	4	2	217	213	210
0	4	4	805	797	808
0	4	5	601	603	589
0	5	1	375	366	354
0	5	2	555	518	516
0	5	4	60	15	16
0	5	5	323	305	302
0	6	1	664	647	653
0	6	2	1092	1162	1112
0	7	1	189	197	206
0	8	1	257	241	243
0	8	2	269	292	303
1	1	0	1110	1121	1120
1	1	1	712	612	599
1	1	-2	266	240	233
1	1	3	195	161	175
1	1	-3	465	441	429
1	1	4	292	258	257
1	1	-4	446	440	430
1	1	5	283	267	264
1	1	7	429	423	442
1	1	-7	297	323	293
1	1	-8	326	329	325
1	2	-1	704	656	656
1	2	-3	1171	1136	1147
1	2	6	402	399	397
1	2	-6	472	493	493
1	2	7	216	247	240
1	2	-7	759	854	881
1	3	1	754	725	736
1	3	-1	379	356	355
1	3	2	527	473	491
1	3	-2	194	182	176
1	3	3	567	532	546
1	3	-3	482	421	443
1	3	4	779	741	754
1	3	-4	286	240	281
1	3	5	369	375	374
1	3	-5	530	488	504
1	3	6	653	694	713
1	4	0	222	229	226
1	4	1	133	159	167
1	4	-1	658	681	665
1	4	-2	201	185	181
1	4	4	357	328	333
1	4	-5	920	956	960
1	5	-1	204	208	185
1	5	2	331	332	334
1	5	-2	514	536	529
1	5	4	200	211	233
1	5	5	226	243	253
1	6	-2	405	409	414
1	6	5	272	240	230
1	6	-5	383	392	398
1	7	3	203	228	215
1	8	1	62	61	56
1	8	-3	214	230	225
2	0	0	1301	1446	1447
2	0	1	619	575	557
2	0	-1	1140	1249	1259
2	0	2	474	423	415
2	0	-2	877	865	886
2	0	3	1293	1236	1212
2	0	-4	613	619	603
2	0	-6	248	253	251
2	0	7	480	415	438
2	0	-8	374	361	360
2	0	-9	261	282	300
2	1	0	1677	1939	2015
2	1	1	514	463	457
2	1	-1	1559	1695	1702
2	1	2	230	234	236
2	1	-2	457	435	441
2	1	3	628	500	531
2	1	-4	1126	1082	1089
2	1	-6	501	549	546
2	1	-7	638	657	653
2	2	0	483	455	457
2	2	1	478	421	411
2	2	-1	285	278	279
2	2	2	188	195	190
2	2	3	417	423	412
2	2	-3	574	799	825
2	2	4	438	367	380
2	2	-4	651	624	621
2	2	-7	553	633	628
2	2	-8	370	479	488
2	3	0	547	537	532
2	3	1	682	644	635
2	3	-1	602	602	601
2	3	2	618	597	575
2	3	-2	427	433	446
2	3	3	460	422	441
2	3	4	955	953	958
2	3	5	514	493	473
2	3	6	403	360	369
2	4	0	104	219	209
2	4	-1	353	349	345
2	4	2	330	336	339
2	4	-3	634	618	617
2	4	4	242	223	212
2	4	-5	645	625	620
2	5	0	114	104	105
2	5	2	322	337	330
2	5	-2	809	803	805
2	5	3	127	147	160
2	5	-4	294	278	296
2	5	5	259	244	239
2	5	-5	336	336	342
2	6	1	725	725	726
2	6	2	425	413	415
2	6	-4	156	179	179
2	6	-6	245	266	256
2	7	1	505	528	538
2	7	-1	289	275	262
2	7	2	420	433	445
2	7	-2	563	561	577
2	7	-3	327	336	339
2	8	1	153	152	157
2	8	2	197	186	189
2	9	-1	58	60	61
3	1	0	363	344	362
3	1	-1	1571	1680	1682
3	1	2	330	317	302
3	1	-2	147	146	156
3	1	3	470	425	425
3	1	-3	858	841	852
3	1	-4	943	906	911
3	1	-5	523	485	486
3	1	-7	765	911	921
3	2	0	852	813	825
3	2	-3	257	233	233
3	2	4	674	659	667
3	2	5	64	53	40
3	2	-5	613	586	568
3	2	-8	172	208	222
3	3	0	521	484	492
3	3	-1	312	288	290
3	3	2	352	317	310
3	3	-2	236	215	218
3	3	4	527	498	502
3	3	-4	306	411	420
3	3	5	306	365	360
3	3	6	272	275	268
3	3	-7	218	218	224
3	3	-8	257	278	282
3	4	1	119	112	113
3	4	-1	225	195	204
3	4	2	543	523	541
3	4	-3	507	518	550
3	4	-5	437	401	426
3	4	6	237	271	285
3	4	-7	263	267	275
3	5	1	634	639	657
3	5	-2	1001	1018	1014
3	5	-3	715	712	729
3	5	-5	705	715	720
3	5	-6	571	578	569
3	7	-3	140	153	142
3	7	-5	63	45	38
3	8	-2	147	152	154
4	0	0	580	528	536
4	0	1	192	193	183
4	0	-1	441	405	427
4	0	2	141	168	189
4	0	-2	502	459	489
4	0	-3	516	525	530
4	0	-4	263	263	281
4	0	-5	267	258	268
4	0	6	304	281	208
4	0	-6	296	309	332
4	0	-7	896	893	886
4	0	-8	593	585	552
4	1	0	651	607	614
4	1	1	215	223	214
4	1	-1	1240	1246	1253
4	1	2	477	491	479
4	1	3	620	608	593
4	1	-3	586	539	565
4	1	-4	760	729	726
4	1	-7	800	758	760
4	1	-8	525	564	572
4	2	0	527	530	519
4	2	1	345	310	300
4	2	-1	1193	1229	1234
4	2	4	582	566	569
4	2	-4	832	810	818
4	2	-5	312	297	283
4	2	-6	241	240	267
4	3	4	174	228	210
4	3	6	207	236	241
4	3	-6	202	221	225
4	3	-7	317	301	286
4	3	-8	270	291	300
4	4	2	191	168	185
4	4	-2	746	750	732
4	4	3	200	240	253
4	4	-3	773	757	742
4	4	4	329	344	342
4	4	5	306	346	362
4	4	-6	549	532	503
4	5	0	331	331	337
4	5	1	458	462	467
4	5	-2	144	142	141
4	5	-3	378	388	402
4	5	-5	475	457	434
4	5	-6	345	338	343
4	6	-2	310	257	263
4	6	-3	303	285	294
4	6	-5	319	318	321
4	7	0	244	248	244
4	7	1	435	434	440
4	7	-5	285	285	301
4	7	-6	300	289	300
4	8	2	132	163	157
4	8	-3	127	129	135
5	1	0	473	457	453
5	1	1	68	71	70
5	1	-1	341	336	339
5	1	2	223	192	197
5	1	-2	214	202	216
5	1	-3	145	123	125
5	1	4	284	284	230
5	1	-4	585	577	594
5	1	-8	477	412	411
5	1	-9	300	373	373
5	2	0	450	435	454
5	2	-1	1354	1357	1356
5	2	2	374	386	375
5	2	-2	554	542	534
5	2	3	707	700	705
5	2	4	204	237	254
5	2	-4	369	307	316
5	2	-5	802	803	811
5	3	0	101	117	130
5	3	-1	274	257	256
5	3	-3	416	394	382
5	4	0	282	305	299
5	4	1	614	625	625
5	4	-2	120	112	107
5	4	-3	962	1005	1018
5	4	5	196	220	222
5	4	-6	229	232	233
5	4	-7	249	237	243
5	4	-8	240	231	235
5	5	0	184	187	206
5	5	2	210	226	232
5	5	-3	191	203	212
5	5	-4	148	167	155
5	5	-6	387	379	385
5	6	0	177	206	197
5	6	-1	57	61	61
5	6	-2	332	334	336
5	6	-3	323	330	337
5	6	-6	195	198	191
6	0	-1	563	559	569
6	0	2	175	227	223
6	0	-4	1142	1128	1149
6	0	-6	1445	1425	1421
6	1	0	263	293	295
6	1	-2	141	122	150
6	1	-4	206	264	267
6	1	-5	285	260	260
6	2	-1	583	575	573
6	2	2	125	154	129
6	2	-2	716	703	696
6	2	3	172	204	204
6	2	-3	248	224	255
6	2	5	128	134	157
6	3	0	126	110	103
6	3	-1	322	339	338
6	3	-2	494	511	499
6	3	-3	530	516	505
6	3	4	105	129	134
6	4	0	378	374	377
6	4	-3	653	657	671
6	4	4	179	150	177
6	4	-4	313	323	319
6	5	-2	414	412	438
6	6	-6	551	547	552
6	7	-2	102	122	112
7	1	3	345	353	366
7	1	-4	255	201	256
7	1	-8	457	415	410
7	2	1	143	150	148
7	2	2	285	287	263
7	2	-2	402	431	435
7	3	0	192	199	187
7	3	-1	277	251	278
7	3	-2	473	482	481
7	3	-3	490	495	497
7	3	-4	508	500	491
7	3	-5	354	367	374
7	3	-7	422	417	415
7	4	0	228	275	281
7	5	1	295	298	304
7	5	-3	182	175	137
8	1	3	101	107	104
8	1	-5	204	201	266
8	1	-8	537	557	533
8	3	0	255	273	279
8	3	1	185	213	207
9	1	-5	197	189	193
9	2	-4	456	468	459
9	3	-2	252	270	267
9	3	-4	302	305	316
9	4	-2	149	163	164
9	4	-6	217	221	217
10	1	-5	355	337	333
10	2	-4	316	311	306

The columns are headed $(h\ k\ \ell)$, $|F_{obs}|$,

$|F^{r.b.}_{calc}|$ and $|F^{m\,m\,m}_{calc}|$.

Observed and Calculated Structure Factors

TABLE 2.2

	mmm symmetry			$\bar{1}$ symmetry		
	x/a	y/b	z/c	x/a	y/b	z/c
C(C)	0.0482	0.1030	0.0359	0.0480	0.1035	0.0352
C(B)	0.1149	0.1606	0.2205	0.1155	0.1591	0.2206
C(D)	0.0761	0.2476	-0.0782	0.0755	0.2487	-0.0777
C(A)	0.0857	0.0174	0.3267	0.0857	0.0164	0.3260
C(E)	0.0099	0.1869	-0.2555	0.0088	0.1876	-0.2566
D(b)	0.1883	0.3185	0.2733	0.1878	0.3178	0.2818
D(d)	0.1499	0.4043	-0.0213	0.1511	0.4053	-0.0219
D(a)	0.1368	0.0627	0.4665	0.1353	0.0630	0.4650
D(e)	0.0318	0.2978	-0.3408	0.0327	0.2972	-0.3414

Rigid body

	b_{11}	b_{22}	b_{33}	b_{23}	b_{31}	b_{12}
C(C)	116	163	174	-10	69	0
C(B)	202	250	187	-50	87	-31
C(D)	190	200	235	15	118	-18
C(A)	262	357	181	-12	115	3
C(E)	251	311	228	52	145	16
D(b)	328	314	253	-119	126	-110
D(d)	307	232	338	-6	182	-89
D(a)	432	561	197	-42	163	-17
D(e)	402	448	311	113	238	14

TABLE 2.3.

Fractional co-ordinates of the molecule with and without the symmetry constraint. The thermal parameters are from R.B.T.P. refinement.

	X	Y	Z
C(C)	-0.0088	0.7076	-0.0015
C(B)	1.2368	1.3982	0.0055
C(D)	-1.2429	1.3991	-0.0055
C(A)	2.4133	0.7046	-0.0008
C(E)	-2.4307	0.6891	-0.0031
D(B)	1.2043	2.4764	-0.0005
D(D)	-1.2461	2.4800	0.0095
D(A)	3.3453	1.2458	-0.0154
D(E)	-3.3700	1.2205	0.0155

standard deviations are 0.0055 for C

0.0079 for D.

Atomic Co-ordinates in Molecular Inertia System for $C_{10}D_8$.

TABLE 2.4

TABLE 2.5

Thermal parameters from $C_{10}D_8$ R.B.T.P. refinement

	U_{11}	U_{12}	U_{13}	U_{22}	U_{23}	U_{33}
C(C)	2.81	0.00	1.76	2.98	-0.22	4.66
C(B)	4.89	-0.65	2.21	4.56	-1.11	5.00
C(D)	4.60	-0.38	3.00	3.65	0.33	6.29
C(A)	6.34	0.06	2.93	6.51	-0.27	4.84
C(E)	6.08	0.34	3.69	5.68	1.15	6.10
D(B)	7.93	-2.31	3.21	5.73	-2.63	6.77
D(D)	7.43	-1.87	4.63	4.23	-0.13	9.04
D(A)	10.46	-0.36	4.15	10.24	-0.93	5.27
D(E)	9.73	0.29	6.06	8.18	2.50	8.32

Thermal parameters from Cruickshank's unconstrained refinement

	U_{11}^{obs}	U_{12}^{obs}	U_{13}^{obs}	U_{22}^{obs}	U_{23}^{obs}	U_{33}^{obs}
C(C)	5.47	-0.22	0.37	3.84	-0.01	3.73
C(B)	5.48	0.82	-0.28	4.79	-0.29	5.63
C(D)	5.98	-1.01	0.01	4.86	0.10	4.89
C(A)	5.84	0.41	0.10	6.84	-0.19	6.34
C(E)	5.20	-1.51	0.11	7.57	-0.19	6.08

C(C)	3.5×10^{-2} ($\mathring{A}^2$)	D(B)	6.8×10^{-2} $(\mathring{A})^2$
C(B)	4.8×10^{-2} ($\mathring{A}^2$)	D(A)	8.7×10^{-2} $(\mathring{A})^2$
C(A)	6.0×10^{-2} ($\mathring{A}^2$)		

Spherically averaged mean square displacements in $C_{10}D_8$. From rigid body thermal motion constrained refinement.

carbon in $C_{10}H_8$ = 0.16×10^{-2} ($\mathring{A}^2$)

from Johnson's results

deuterium in $C_{10}D_8$ = 0.6×10^{-2} ($\mathring{A}^2$)

from Pawley's results

C(C)	0.13×10^{-2} ($\mathring{A}^2$)	
C(B)	0.20×10^{-2} ($\mathring{A}^2$)	from Higg's calculations
C(A)	0.17×10^{-2} ($\mathring{A}^2$)	

Mean square displacements in $C_{10}H_8$ and $C_{10}D_8$ for internal modes.

TABLE 2.5

Figure 2.1 Schematic Diagram of a Four-Circle Diffractometer (page 26)

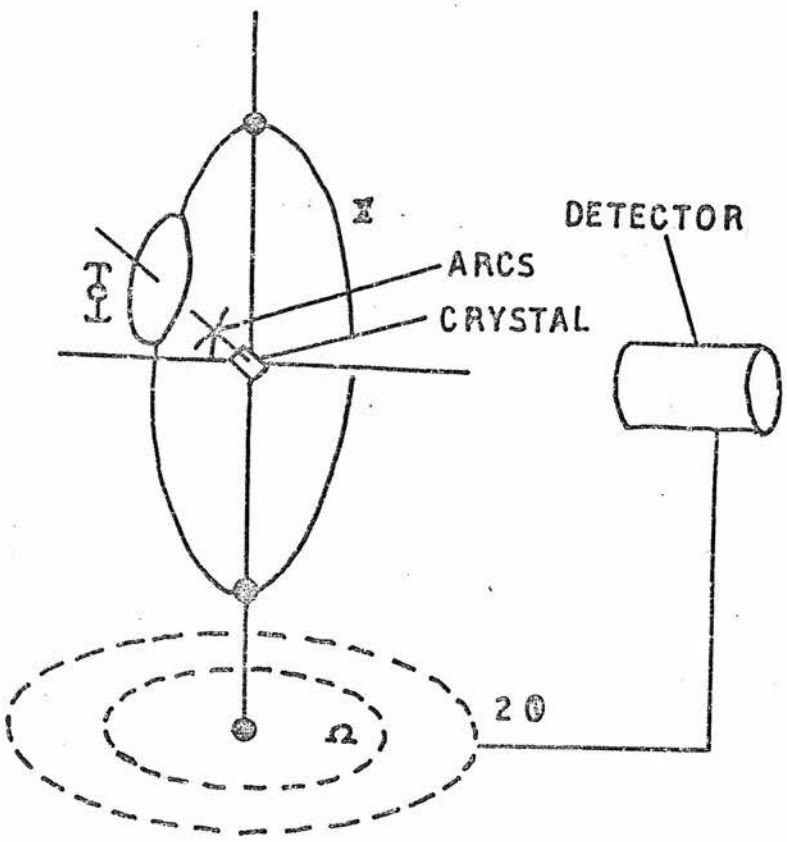

FIGURE 2·1

Figure 2.2 Typical Bragg Intensity Profile (page 28)

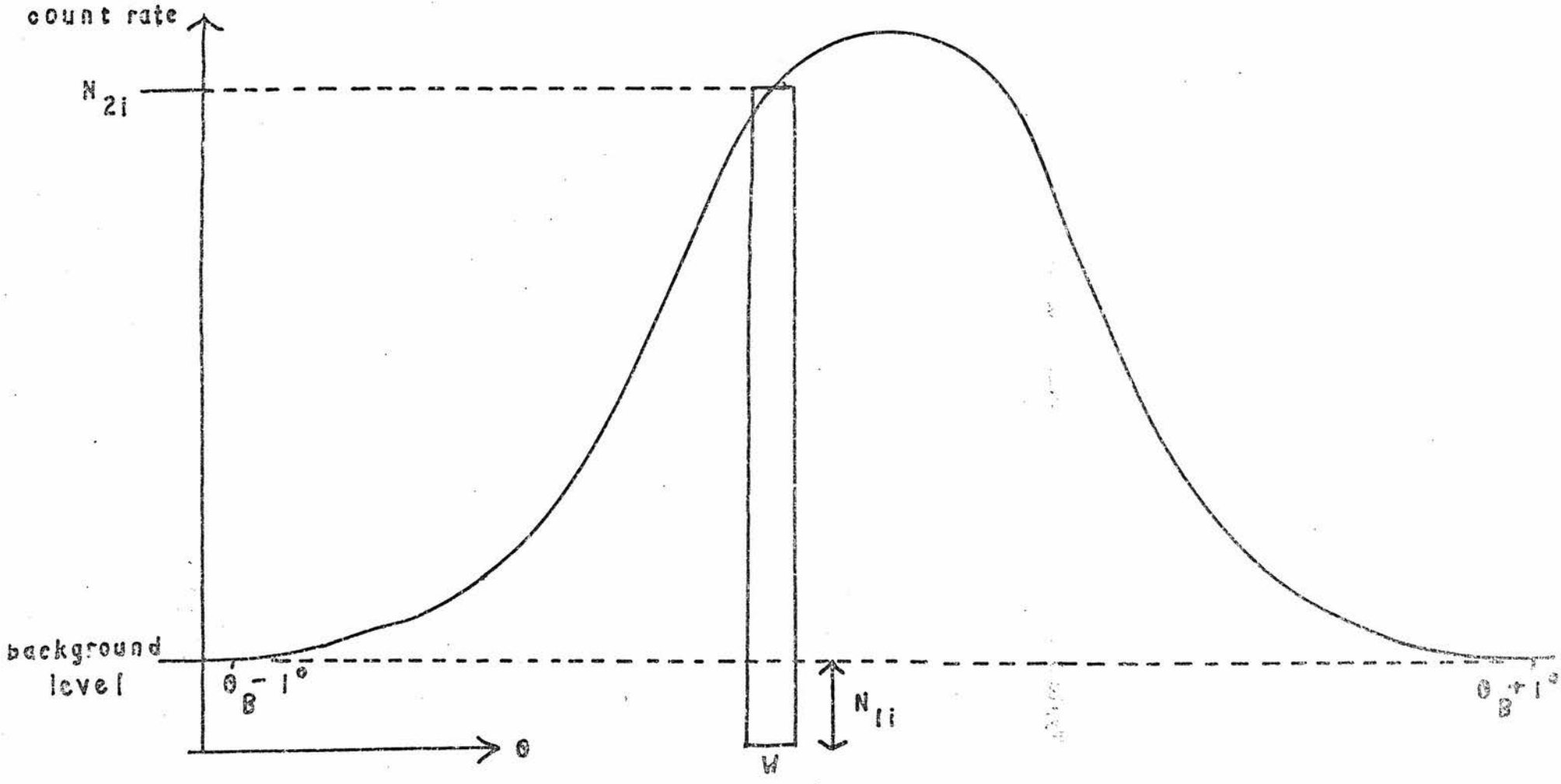
count rate
N_{2i}
background level
$\theta_B - 1°$
$\theta_B + 1°$
θ
N_{1i}
W

FIGURE 2·2

Figure 2.3 Histogram of Observed Structure Factors for (200) Standard Reflection (page 34)

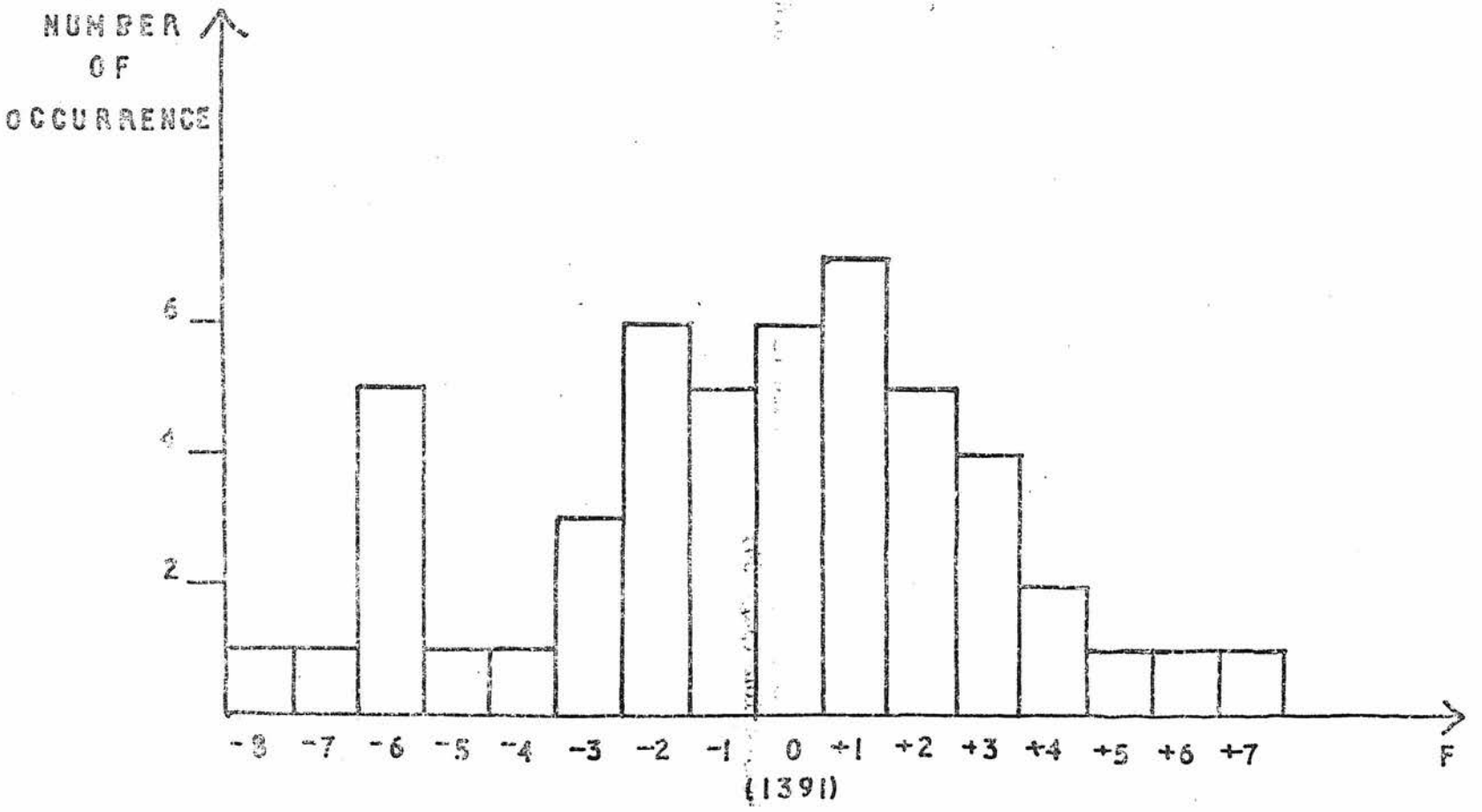

(1391)

FIGURE

2·3

Figure 2.4 The Molecule of Naphthalene under $\bar{1}$ Symmetry Constraint (page 38)

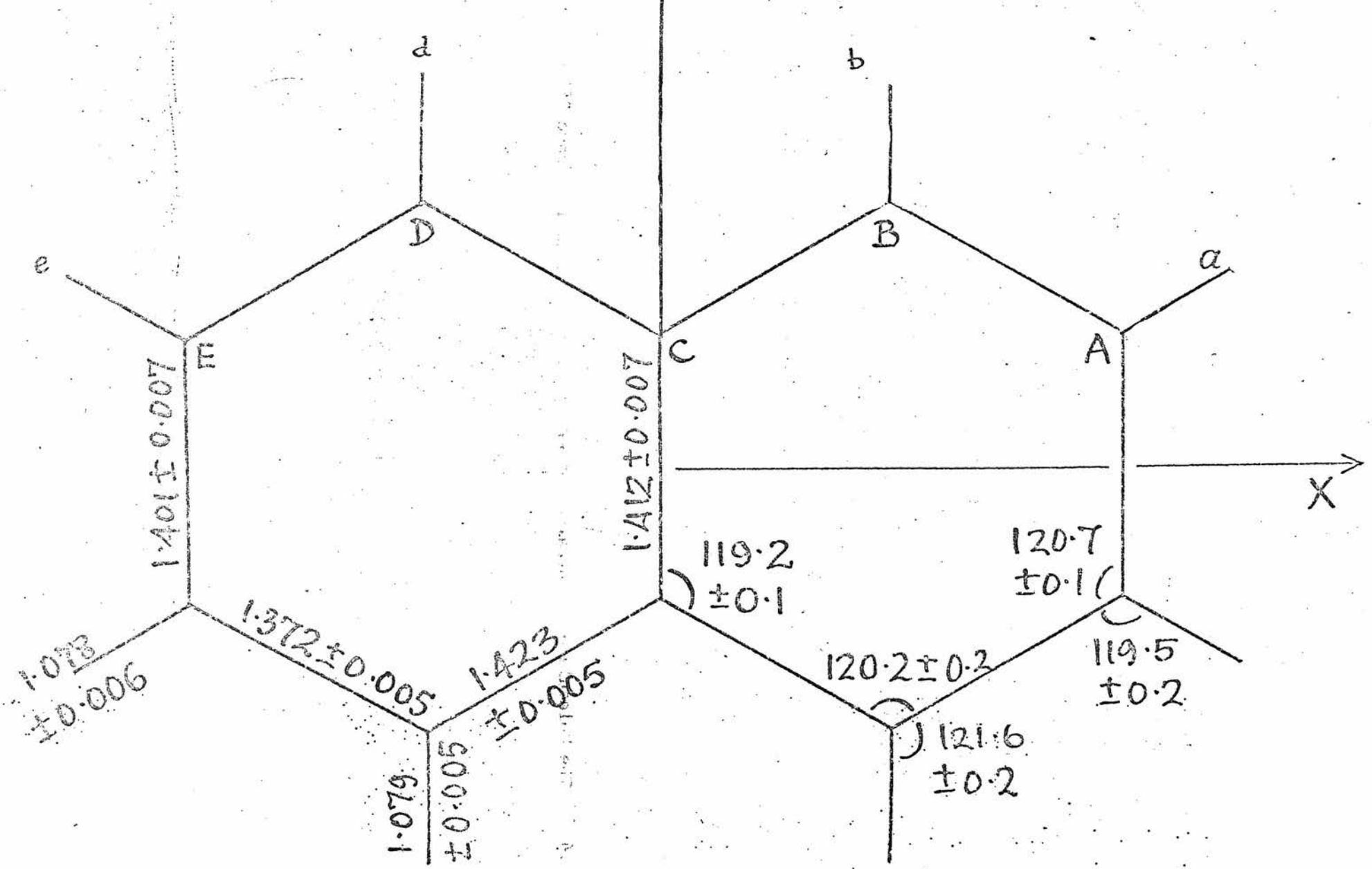
d
b
e
D
B
a
E
C
A
X
1·401±0·007
1·412±0·007
119·2
±0·1
120·7
±0·1
1·073
±0·006
1·372±0·005
1·423
±0·005
120·2±0·2
119·5
±0·2
121·6
±0·2
1·079
±0·005

FIGURE

2·4

Figure 2.5 Neutron Scattering Density in the Mean Molecular Plane (page 43)

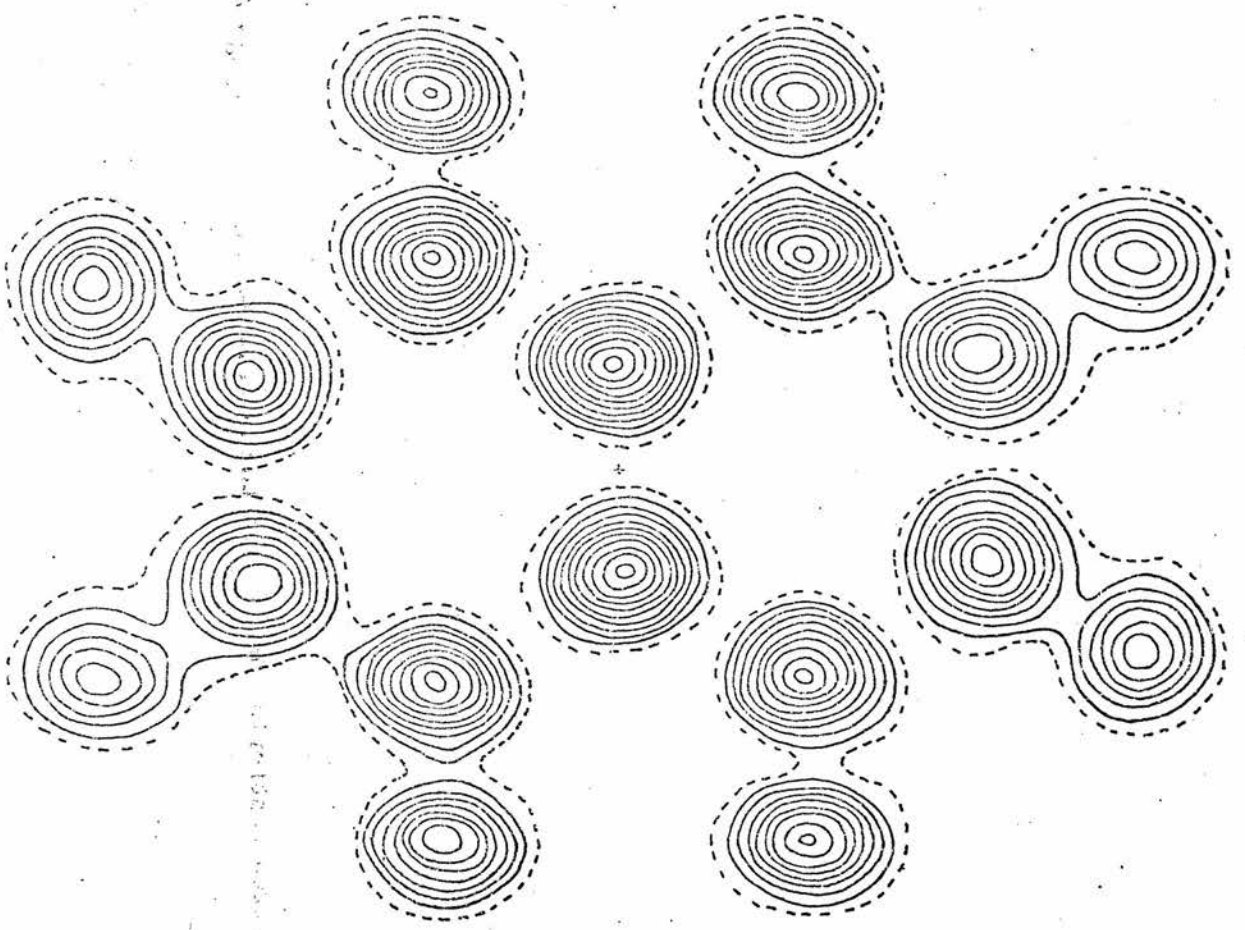

FIGURE
2·5

CHAPTER 3

THE LATTICE DYNAMICS OF NAPHTHALENE

In this chapter we discuss the application of the theory of lattice dynamics to molecular crystals, with particular reference to naphthalene. We describe the measurement of phonon frequencies in deuterated naphthalene, and compare the results with the predictions of various models. We discuss the effect on the phonon dispersion curves of varying the model parameters, and conclude with a discussion of the measurements which might be made to resolve the discrepancies between the calculated and experimental dispersion curves.

In molecular crystals the intra-molecular forces are considerably stronger than those between different molecules. Consequently, some of the crystal normal modes involve only relative motions between molecules, with individual molecules behaving as almost rigid units. We shall refer to these modes as external modes.

3.1 Theoretical Introduction

At present we assume that the molecule vibrates as a completely rigid unit in the external modes. Cochran and Pawley[44] have shown that a general mode has translational and rotational components, and for a centrosymmetrical molecule these components are $\frac{\pi}{2}$ out of phase. The k^{th} molecule in the ℓ^{th} unit cell, situated at $\underline{R}(\ell k)$, is given a translational displacement (expressed as a travelling wave)

$$\underline{u}(\ell k) = \underline{U}(\underline{q}k) \exp\left\{ i(\underline{q}.\underline{R}(\ell k) - \omega(\underline{q})t) \right\} \qquad (3.1)$$

and a rotational displacement

$$\underline{\theta}(\ell k) = \Theta(\underline{q}k) \exp\left\{ i(\underline{q}.\underline{R}(\ell k) - \omega(\underline{q})t) \right\} . \qquad (3.2)$$

The displacement of the p^{th} atom in the k^{th} molecule is

$$\underline{u}(\ell k p) = \left[\underline{U}(\underline{q} k) + \underline{\textcircled{M}}\,(\underline{q}\, k) \times \underline{R}(p) \right] \times \exp\left\{ i(\underline{q}.\underline{R}(\ell k) - \omega(\underline{q}) t) \right\} \qquad (3.3)$$

and

$\underline{R}(p)$ is the position of the atom, p, relative to the centre of the k^{th} molecule.

If we combine equations (3.1) and (3.2) to give a six-component vector $\underline{u}(\ell k)$ $(u_x\ u_y\ u_z\ u_\alpha\ u_\beta\ u_\gamma)$, the inter-molecular force and couple constants are

$$\Phi_{ij}(\ell k \ell' k') = \frac{\partial^2 \Phi}{\partial u_i(\ell k)\, \partial u_j(\ell' k')} \quad ; \qquad (3.4)$$

u_x is a translational displacement along x and u_β a rotational displacement about the y-direction. There is no restriction on the choice of axes, and we choose to express the displacements relative to the principal inertia system of the corresponding molecule. This will avoid products of inertia in the equations of motion. These equations of motion are, for example,

$$m \ddot{u}_x(\ell k) = -\sum_{\ell' k' i} \Phi_{xi}(\ell k \ell' k') u_i(\ell' k')$$

$$I_\alpha \ddot{u}_\alpha(\ell k) = -\sum_{\ell' k' i} \Phi_{\alpha i}(\ell k \ell' k') u_i(\ell' k')$$

$$\text{or} \quad M_j \ddot{u}_j(\ell k) = -\sum_{\ell' k' i} \Phi_{ji}(\ell k \ell' k') u_i(\ell' k') \qquad (3.5)$$

where $M_j = (m\ m\ m\ I_\alpha\ I_\beta\ I_\gamma)$, and the j specifies an x or β, not a particular mode. Substituting equations (3.1) and (3.2) in equation (3.5) we obtain

$$\omega^2(\underline{q})M_j U_j(\underline{q}k) = \sum_{\ell' k' i} \Phi_{ji}(\ell k \ell' k') U_i(\underline{q}k) \times$$

$$\exp i\,\underline{q}.(\underline{R}(\ell' k') - \underline{R}(\ell k))$$

or

$$\omega^2(\underline{q})\xi'_j(\underline{q}k) = \sum_{k' i} \xi'_i(\underline{q}k) \sum_{\ell'} \frac{\Phi_{ji}}{\sqrt{M_i M_j}} \exp i\underline{q}.(\underline{R}(\ell' k') - \underline{R}(\ell k)) \quad (3.6)$$

where $\xi'_j(\underline{q}k)$ replaces $\sqrt{M_j}\, U_j(\underline{q}k)$.

Equation (3.6) defines an element of the dynamical matrix

$$M_{ji}(kk'\underline{q}) = \sum_{\ell'} \Phi_{ji}(\ell k \ell' k') \exp i\,\underline{q}.(\underline{R}(\ell' k') - \underline{R}(\ell k)) \quad . \quad (3.7)$$

Naphthalene has two molecules in the unit cell, one at the origin and the diad related one at $(\frac{1}{2}\ \frac{1}{2}\ 0)$. Following Pawley, we label these E and D respectively. The $\xi'(\underline{q}k)$ have therefore twelve components and the dynamical matrix is Hermitian, in general. Using the $\frac{\pi}{2}$ phase relationship between the translational and rotational components of an eigenvector reduces this to a real 12 x 12 matrix, giving twelve values of $\omega^2(\underline{q}j)$ and twelve eigenvectors $\underline{\xi}(\underline{q}\ k\ j)$, with components

$$\begin{aligned} \xi_1 &= \xi'_x(\underline{q}E) & \xi_7 &= \xi'(\underline{q}\ D) \\ \xi_4 &= i\xi'_\alpha(\underline{q}E) & \xi_{10} &= i\xi'(\underline{q}\ D) \end{aligned} \quad . \quad (3.8)$$

Cochran and Pawley[44] and Pawley[45] have expressed the dynamical matrix for external vibrations in the molecular crystal hexamethylene tetramine (H.M.T.), in terms of only four parameters, and obtained sets of dispersion curves for

various values of these parameters. The high crystal symmetry reduced the number of independent parameters specifying the interactions to eight, and half of these could be deduced from experimental Raman frequencies and elastic constants. Experimental phonon frequencies have now been used to determine all the parameters[46].

We now consider how symmetry restricts the number of independent parameters specifying intermolecular interactions in naphthalene. Let k denote the E-molecule at the origin, k_1 a D-molecule at say, $(\frac{1}{2}\ \frac{1}{2}\ 0)$, k_2 a D-molecule at $(-\frac{1}{2}\ \frac{1}{2}\ 0)$. Then, crystal symmetry requires $\underline{\Phi}(k\ k_1)$ and $\underline{\tilde{\Phi}}(k\ k_2)$ to have components of the same magnitude with signs differing for $x\beta$ and αy terms. In addition symmetry requires the same relation between components of $\underline{\Phi}(k'\ k'')$ and $\underline{\Phi}(k'\ k''')$, where the molecule k''' is related to k'' by inversion, and k' is an E molecule if k'' is E, and D if k'' is D. The derivation of these relations is given by Pawley[8].

For the naphthalene crystal, in contrast to H.M.T., symmetry requirements on the Φ_{ij}'s do not reduce the independent elements of the dynamical matrix to a reasonable number. A different approach is required. Pawley has calculated phonon dispersion curves in naphthalene and anthracene by considering the interatomic potential in parametric form. A suitable potential is the Buckingham potential

$$V_i(\underline{r}) = -\frac{A_i}{r^6} + B_i \exp(-\alpha_i r) \qquad (3.9)$$

where i denotes a particular type of atom pair. This form of potential has been used to discuss the crystal potential in some aromatic hydrocarbons[47]. The results of phonon

fitting in H.M.T. starting from a potential of this type are expected soon[48].

For naphthalene there are three types of atom pair, C - C, C - H and H - H, giving nine parameters to specify $V(\underline{r})$. The Φ_{ji}'s are double differentials of the crystal energy, Φ, and may be calculated analytically by summing forces and couples between all atom pairs in the molecules (ℓk) and $(\ell' k')$.

3.2 The Preliminary Calculation and its Results

In naphthalene there is only one symmetry direction, [0 1 0]. In this direction there is a difference between symmetric and antisymmetric branches of the phonon dispersion curves. In a symmetric mode of vibration, the space group symmetry is maintained. Consequently, all our calculations had $\underline{q}$ in this direction. The axis of greatest inertia (I_1), is that perpendicular to the plane of the molecule. Axes (2) and (3) lie in the molecular plane. For $C_{10}D_8$ $I_1 = 1072$, $I_2 = 754$, $I_3 = 317$ in units of 10^{-40} gm. cm.^{2}. The direction cosines of these inertia axes relative to the orthogonal axes $[\underline{a}, \underline{b}, \hat{\underline{n}}\ c\sin\beta]$ are

-0.8539	0.3964	-0.3371	:	Axis 1
-0.2793	-0.8957	-0.3459	:	Axis 2
-0.4391	-0.2012	0.8756	:	Axis 3

(3.10)

for the E molecule.

The first differentials were performed analytically, and the molecules were allowed to rotate slightly so that there were no resultant forces or couples on them. Kitaigorodskii[49] has shown that there is a minimum in Φ,

close to the true lattice spacings and orientations of the molecules. The slight rotation to obtain a minimum in $\underline{\Phi}$ ensures equilibrium for the initial structure.

The second differentials were obtained numerically. By giving the molecule (k') a small displacement, either translational or rotational, the changes in the forces and couples on the molecule (k) were computed by summing over all atom pairs in the two molecules. The $\underline{\Phi}_{ji}$'s were calculated for interactions between the molecule at the origin and those at (0 0 1), (0 1 0), ($\frac{1}{2}$ $\frac{1}{2}$ 0), ($-\frac{1}{2}$ $\frac{1}{2}$ 0), ($\frac{1}{2}$ $\frac{1}{2}$ 1) and ($-\frac{1}{2}$ $\frac{1}{2}$ -1). Following Pawley's calculations[8] only atom-atom contacts of less than 5.5Å were included, since it was found that only a 1% variation in the mode frequencies occurred when the interaction limit was increased from 5.0Å to 5.5Å, compared with a 7% variation in the range 3.5Å to 4.0Å.

To satisfy the required symmetry, the interaction tensors between the molecules at (0 0 0):(0 0 1) and (0 0 0):(0 1 0) were "symmetrised" after numerical differentiation, since computer round-off errors caused slight discrepancies between symmetry related elements. The appropriate elements of $\underline{\Phi}$(0 0 0 ; $\frac{1}{2}$ $\frac{1}{2}$ 0) and S$\underline{\Phi}$(0 0 0 ; $-\frac{1}{2}$ $\frac{1}{2}$ 0) as well as $\underline{\Phi}$(0 0 0 ; $\frac{1}{2}$ $\frac{1}{2}$ 1) and S$\underline{\Phi}$(0 0 0 ; $-\frac{1}{2}$ $\frac{1}{2}$ -1) were averaged to satisfy the symmetry restrictions on the $\underline{\Phi}$'s. (S is -1 for $x\beta$ and αy terms and +1 for terms such as xx, $\beta\beta$). Pawley has written a computer program which performs these calculations for naphthalene and this has been used throughout.

The results of the initial calculation for $\underline{q} = 0$ are given in Table 3.1. The model parameters are those used by Pawley[8]. Pawley has pointed out that eigenvectors do not

depend strongly on the model parameters, although the frequencies do. We may therefore use the eigenvectors of Table (3.1) to discuss the general properties of the different vibrational modes. We do not expect these properties to alter much during the course of our calculations.

We have labelled the modes as S or A to correspond to symmetric and antisymmetric vibrations. For an S mode

$$\xi_{I+6} = +\xi_I \quad \text{and} \quad \xi_{I+6} = -\xi_I \quad \text{in an A}$$

mode. For $\underline{q} = 0$, the modes have either purely translational or purely rotational character. The branches ST(10), AT(11) and AT(12) have $\omega \rightarrow 0$ as $\underline{q} \rightarrow 0$, and are acoustic branches They represent pure translations, which, for $\underline{q} = 0$, are longitudinal with respect to $\underline{b}$ for ST(10) and transverse to $\underline{b}$ for AT(11) and AT(12). The other three translational branches are infra-red active optic branches.

The six pure rotational modes are Raman active, and the form of their eigenvectors at $\underline{q} = 0$ ascribes them to lines observed in the Raman spectrum. Three belong to the symmetry species Ag (or S in our notation), the others are Bg or A modes. The polarisability tensors for the different species have different components which are non-zero[51], and so the symmetry of the Raman lines may be determined. For fairly weak intermolecular forces, the energies of the S and A modes for librations about the same inertia axis should be similar, and the six modes will occur in pairs. If the restoring forces are the same for all three modes, then the highest frequency pair should correspond to libration about the axis of least inertia, and the lowest frequency pair to libration about the axis of greatest inertia.

Ito et al.[51] have measured Raman frequencies in $C_{10}H_8$ and $C_{10}D_8$ at various temperatures, and their results are given in Table (3.2). Since the convention is to quote Raman frequencies in cm^{-1}, we have used these units in this table. It is usual to quote phonon frequencies obtained by neutron inelastic scattering in THz., and we shall use these units when appropriate. The conversion is 100 $cm^{-1} \equiv 3.03$THz. SR(3) and AR(5) are separated by about 40 cm^{-1} from SR(1) and AR(2). By considering the intensities of the Raman lines in various polarization spectra, Ito has shown that the high frequency modes correspond to librations predominantly about axis 3 but the others are for coupled librations* about the axes 1 and 2. The calculated eigenvectors for modes SR(3), AR(5), SR(6) and AR(8) agree with these conclusions although there is considerably more coupling in the A modes than in the S modes.* In both the calculated and experimental sets of frequencies, the S species lie above the A, except for the experimental pair SR(1) and AR(2).

As $\underline{q}$ increases from zero, the branches remain S or A and at the zone boundary, where $|\underline{q}| = 0.5$ along $[0\ 1\ 0]$, the modes are degenerate with one mode from the S representation having the same frequency as one from the A representation. The eigenvectors at $|\underline{q}| = 0.5$ may be any linear combinations of the degenerate mode eigenvector pairs, and are indeterminate. For all values of $\underline{q}$ other than zero, the modes are partly translational and partly rotational.

*Footnote

The term "coupled librations" is used in the sense of reference (51) and does not imply that we consider anharmonicity.

3.3 The Effect of Molecular Distortion on the Phonon Frequencies

In many molecular crystals the lowest intramolecular frequencies are typically ten times those of the highest external mode frequencies. For these crystals, the treatment of Section 3.1 should be expected to give the external mode frequencies very accurately. However, in naphthalene, the highest external mode is at 141 cm^{-1} at $\underline{q} = 0$, compared with 176 cm^{-1} for the lowest intramolecular mode. This result indicates that there will be some molecular distortion in the low frequency modes. We should, therefore, set up the equations of motion in terms of displacements of each of the 36 atoms in the unit cell, and solve the (108 x 108) Hermitian dynamical matrix to obtain eigenfrequencies and eigenvectors. (2 x 48) of these frequencies will be close to, but greater than, the non-zero frequencies obtained from a calculation of the vibrations of a free molecule of naphthalene. The other (2 x 6) frequencies correspond to the external modes. These calculations have been performed for naphthalene by Pawley and Cyvin[52], and details are given in their paper.

Pawley and Cyvin find that all branches corresponding to external modes are decreased in frequency throughout the zone, with frequency shifts of up to 15%. The fractional shifts vary from branch to branch, and with $\underline{q}$. Experimental phonon frequencies are for a deformable molecule, and in any attempt to fit these to a model we should compare them with the results of the calculation for a non-rigid molecule. Alternatively we may follow Pawley and Cyvin's suggestion that experimental frequencies may be altered systematically

before comparing them with model calculations. This is the approach which we have adopted, since it simplifies the computing considerably. Before altering the experimental frequencies they must be assigned to the correct branch of the dispersion curves. This requires a knowledge of the mode structure factors, and we consider these in the next section. The Raman frequencies may be altered systematically, since we have already identified them with particular branches.

Pawley and Cyvin publish their results in the form of dispersion curves for both rigid molecule and deformable molecule calculations. To alter the experimental results we identify these with the deformable molecule curves, and alter these proportionately to give frequencies which correspond to the rigid molecule results.

3.4 The One-Phonon Structure Factors for Naphthalene

For scattering of neutrons from the mode $(\underline{q}j)$, the structure factor is

$$G(\underline{K}j) = \underline{K}.\sum_{k}\sum_{p} f(\underline{K}p)\exp\left[i\underline{K}.\underline{R}(p)\right] \left[\underline{U}(\underline{q}kj) + \underline{\Theta}(\underline{q}kj) \times \underline{R}(p)\right] \exp\left\{i\underline{\tau}.\underline{R}(k)\right\} \quad (3.11)$$

This corresponds to the X-Ray structure factor given by Cochran and Pawley[44], and is obtained from it by replacing the $\underline{K}$-dependent scattering factor for X-Rays by a neutron coherent scattering length. The summation is over all atoms, p, in the molecule, and over all molecules in the unit cell; in this case, one E-molecule and one D-molecule. $f(\underline{K}p)$ includes the scattering length, b_p, and the Debye-Waller factor, $e^{-W_p(\underline{K})}$. The factor $\left[\underline{U}(\underline{q}kj) + \underline{\Theta}(qkj)x\underline{R}(p)\right]$ arises

from the displacement of atom p, in molecule k, under the mode ($\underline{q}j$). This is easily obtained in terms of the mode eigenvector, $\underline{\xi}(\underline{q}kj)$, using equations (3.8). Equation (3.11) may be written

$$G(\underline{K}j) = \sum_p \left[\underline{K}.\underline{t}(Ej) + i\underline{K}.\underline{r}(Ejp)\right]\left[\cos\theta(Ep) + i\sin\theta(Ep)\right]$$

$$+ \left[\underline{K}.\underline{t}(Dj) + i\underline{K}.\underline{r}(Djp)\right]\left[\cos\theta(Dp) + i\sin\theta(Dp)\right] \quad (3.12)$$

where the sines and cosines incorporate the exponentials, and $f(\underline{K}p)$, and depend on the value of $\underline{\tau}$. The summation is now over the atoms in one molecule only,

$$\underline{t}(Ej) = (\xi(1j); \xi(2j); \xi(3j))_F$$

$$\underline{r}(Ejp) = (\underline{\xi}(j) \times \underline{R}(p))_F$$

using components 4, 5 and 6 of $\underline{\xi}$, with similar relations for atoms in the D-molecule. These will involve the components 7 to 12 of $\underline{\xi}(j)$. The F denotes a transformation from the appropriate molecular axes to the orthogonal set $[\underline{a}, \underline{b}, \hat{\underline{n}}c \sin\beta]$, so that atomic displacements are expressed as fractions of the cell dimensions. The cross-section is proportional to $((G_R)^2 + (G_I)^2)$ where G_R and G_I are the real and imaginary parts of (3.12).

3.5 The Measurement of Phonon Frequencies in $C_{10}D_8$.

Using the $\underline{\xi}(\underline{q}j)$ of reference (8), and Table 3.1, we may calculate the one-phonon structure factors. These allow us to plan the experiment, deciding the $\underline{\tau}$ at which to observe scattering from the branch j.

We have performed a neutron inelastic scattering experiment

at 295°K on a crystal of 98°/o deuterated naphthalene, using the PLUTO triple-axis spectrometer. Our crystal was a cylinder of length 3 cm. and diameter 1.7 cm., with a mosaic spread 1°, measured relative to an aluminium monochromator of mosaic 0.2°. We used $(\underline{b}^* - \underline{c}^*)$ as the scattering plane and searched for phonons with $\underline{q}$ along $\underline{b}^*$. Throughout, the spectrometer was operated in the "constant-$\underline{K}$" mode.

We have reported the measurement of some anomalously low frequency phonons[53]. We now believe that many of the corresponding peaks in the count rate, N_D, were caused by spurious Bragg intensity, by a process described in detail in Chapter 5 (p. 98). This process is particularly troublesome in crystals of large mosaic spread. The 2°/o hydrogen gave us a very high incoherent background of about 20 counts/minute, on average. We observed several weak peaks, which appeared to be due to scattering from some of the lower optic branches, but were unable to obtain complete branches.

We concluded that it would be necessary to obtain a better single crystal of more highly deuterated naphthalene before continuing our measurements.

Dietrich and Pawley (unpublished) have measured phonon frequencies in $C_{10}D_8$ at 77°K, using a good single crystal of 99.5°/o deuterated material. Seven almost complete branches of the dispersion curves have been measured, including the three acoustic branches. The incoherent background was only 2 counts/minute, but the peak to background ratio for scattering from the higher frequency optical branches was still too small to allow measurement.

We have altered these experimental phonon frequencies to correspond to the results for a completely rigid molecule, and

these are presented in Figure (3.1). The assignments are due to Dietrich and Pawley, who have used the cross-sections predicted from the eigenvectors of reference (8). Figure (3.1) also includes Raman frequencies from Table 3.2.

These dispersion curves show that a knowledge of the cross-sections is essential to assign experimental frequencies to the correct branch.

3.6 The Dependence of Phonon Frequencies on the Model Parameters

Our aim is to fit the phonon frequencies in $C_{10}D_8$ by varying the nine parameters of equation (3.9). Rather than perform a full least-squares refinement at this stage, it was decided to vary the parameters independently, and catalogue their effect on the different branches of the dispersion curves. One difficulty in programming a least squares refinement of the data, is the inclusion of some selection process which picks the correct calculated frequency, $\omega_{calc}(j)$, to compare with an experimental frequency $\omega_{exp}(n)$. The $\omega^2_{calc}(j)$ are obtained as eigenvalues of the dynamical matrix, and the corresponding eigenvectors must be used to pair them with an $\omega_{exp}(n)$, labelled perhaps "ST" or "AR". In Figure (3.2a, b) we illustrate the branches SR(3) and ST(4), obtained for slightly different potential parameters. These branches belong to the same symmetry species, S, and therefore cannot cross. As $\underline{q}$ increases from zero, branch (3) takes on translational character, and branch (4) rotational. For model (a), the lower branch is ST, but it is the higher for model (b). This shows that the order of the branches may alter during a least-squares refinement, and experimental and calculated

frequencies cannot be paired correctly, without considering the eigenvectors at each stage. The significant properties of the $\underline{\xi}(j)$ are their symmetry and degree of translational and rotational character. The structure factor is continuous along the broken curve in Figure (3.2a), and it is this ω-$\underline{q}$ relation which is followed in a series of experimental measurements.

For each of our model calculations we identified the different branches by considering the form of the $\underline{\xi}(\underline{q}j)$. In Table 3.3 we list the percentage change in the $\omega^2(j)$ for 25°/o changes in the A_i's and 3°/o changes in the α_i's. The relative effect, on the ω^2, of changing the B_i's follows that of the corresponding α_i, and need not be tabulated separately. However we include B(3) in Table 3.3, for reference.

All changes are relative to the model of Table 3.1.

The long-range C - C forces affect the (T) modes more than the (R) modes. The long-range D - D forces have their main effect on the (R) modes, with the effect increasing with decreasing frequency. The long-range C - D forces affect AR(8) predominately, but otherwise have more effect on the (T) modes than the (R) modes. The short-range C - C forces mainly affect the (T) modes, whereas the short-range D - D forces shift the branches SR(3), AR(5) and AR(8) relative to the others. The short-range C - D forces alter the frequencies of SR(3) and AR(5) much less than those of the other branches.

In general, we note that different parameters affect the rotational branches by varying amounts, and it is possible to raise or lower them, relative to the translational branches. However, it is not possible to move the acoustic branches

independently of ST(4).

3.7 Comparison of Experimental and Calculated Phonon Dispersion Curves

We now discuss the results of various calculations and compare them with the experimental results of Figure (3.1). Harada and Shimanouchi[54] have assigned three weak absorptions, observed in the low frequency region of the infra-red spectra of naphthalene crystals, to the three infra-red active translational modes of that crystal. These are ungerade modes ($2A_u$ and $1B_u$) in the spectroscopists' notation, and are the modes ST(4), ST(9) and AT(7) of Table (3.1). These infra-red peaks have also been observed by Hadni[55], and we include them (again altered to correspond to the results for a rigid molecule) in Figure (3.1). Harada and Shimanouchi have fitted the Raman and infra-red data available to them[56, 57] by determining a set of interatomic force constants for all H-H and C-H bonds of less than 3.3Å. However, their treatment assumes that the force is the same for the three C-H bonds in the range 3.026 → 3.049Å, (and those in the range 3.14 → 3.29 Å (five C-H bonds).) Using the parameters of Table 3.1 to calculate these force constants, we find that the long range change by 30°/o and the short-range by 50°/o as r increases from 3.14Å to 3.29Å. This suggests that the approximation is not valid. Harada and Shimanouchi conclude that the C-H interaction is important in a consideration of the vibrational problem of crystalline hydrocarbons with short C-H intermolecular distances. These C-H interactions must be included as well as the H-H interaction of a De Boer type[58].

All our calculations, which were to be compared with the neutron data, incorporated cell dimensions, measured at 77°K. These represent a 3.5°/o increase in a^*, a 1.5°/o increase in c^* and a 0.5°/o increase in b^*. These calculated ω^2 showed, on average, a 50°/o increase over the ω^2 for the room temperature cell.

We describe our comparison of experimental and calculated frequencies in terms of a χ^2 defined by,

$$\chi^2 = \frac{1}{n-p} \sum_i \frac{(\omega_{calc}(i) - \omega_{exp}(i))^2}{(\sigma(i))^2} \qquad (3.13)$$

for n observations and p parameters. There are 40 observations and 9 parameters and 26 of the observed frequencies belong to optical branches. The $\sigma(i)$ are the estimated experimental errors. These are 0.03 THz. for acoustic branches and (0.05 → 0.06)THz. for optic branches. The Raman measurements for AR(5) and SR(6) are in excellent agreement with the neutron measurements, and so these were given errors of only 0.03 THz., at $\underline{q} = 0$. The agreement is not so good for AR(8), and so this experimental point was given an error of 0.06 THz. We have not included infra-red frequencies in our χ^2-calculations, as contradictory results have been obtained for some molecular crystals, and there is some support for ascribing several bands to impurity or defect-induced absorption[55].

We have used various sets of potential parameters to calculate the phonon dispersion curves, and found it impossible to fit the experimental acoustic branches, and the branch ST(4), simultaneously. Several of the models fitted either the optic or the acoustic branches satisfactorily. To emphasize this we have calculated separate χ^2's for the

acoustic and optic branches, as well as the overall χ^2 of equation (3.13). The optic and acoustic χ^2's we call χ^2_{optic} and χ^2_{acoustic}, and for these there are 26 and 14 observations, n. The summation over i of equation (3.13) is taken over the appropriate observations. The results for several models are given in Table 3.4. For reference we quote the corresponding χ's for the potential parameters of Table 3.1.

The best overall fit is given by model III, and a list of observed and calculated frequencies, with the value of $\frac{(\omega_{\text{calc}}(i) - \omega_{\text{exp}}(i))^2}{\sigma(i)^2}$ for each observation, is given as Table 3.5. The main contribution to χ^2 arises from the acoustic branches, and the branch ST(4). The rather high value of χ_{acoustic} is a result of choosing the potential parameters to give a low overall χ^2 by obtaining the best simultaneous fit to ST(4), ST(10), AT(11) and AT(12).

The values in Table 3.5 also show that the Raman measurements for SR(1) and AR(2) are not fitted well by the model. This was a characteristic of every model that we have tried. The calculated separation of these branches is always much less than experiment suggests, and calculations always give SR(1) above AR(2). Raman measurements on anthracene[51] show that the S and A modes, corresponding to librations about the axis of least inertia, have frequencies of 131 $cm.^{-1}$ and 139 $cm.^{-1}$ at 77°K. The separation of these branches in anthracene is much less than in naphthalene. Our model appears to be unable to account for the order of this pair of modes, as well as their relatively large separation in naphthalene. The solution to this problem may lie in the introduction of anisotropic forces, and further measurements would be

helpful, for example tracing the branches SR(1) and AR(2) out to the zone boundary.

The experimental results show that the branch AR(5) is almost flat, but this is not a characteristic of our model calculations. We can fit the ω_{exp} for this branch for values of $|\underline{q}|$ out to 0.25, but the ω_{calc} for $|\underline{q}| > 0.25$ increase more rapidly than is found experimentally. This suggests that, for large $|\underline{q}|$, our model overestimates the restoring forces for this particular mode of vibration.

The striking discrepancy between theory and experiment for the branch ST(4) merits further investigation. The infra-red data give the frequency of this branch at $\underline{q} = 0$ as about 3 THz., compared with the neutron estimate of (2.44 ± 0.06)THz. Although we do not wish to place too much importance on the infra-red measurements, we should like to point out that this particular result is in better agreement with the predictions of our model calculations. The assignment of Figure (3.1) may be in error, and the neutron results, labelled by ST(4), may in fact belong to some other branch of the dispersion curves. If we omit ST(4) from our calculations, model II gives the best fit to the experimental data. Its χ for the optic branches is now 2.5, and the overall χ is 2.0.

In a future experiment the assignment to ST(4) could be investigated by measuring the corresponding intensity at a series of reciprocal lattice points. Once the experimental data had been corrected to allow for the $(\frac{k_1}{k_o})$ factor appearing in the cross-section (equation (1.11)), the least-squares program, described in Section 6.1c, could be adapted to determine the eigenvector $\underline{\xi}(j)$ for this mode. The structure factor of equation (3.11) differs from that of equation (6.12) in having a real and imaginary part. These must be computed

separately, and squared before adding them to obtain an intensity. The $\underline{\xi}(j)$ for naphthalene is described by seven parameters. These are the six components, $\xi(j1) \rightarrow \xi(j6)$, and an additional parameter, (+1 or -1), which determines the symmetry of $\underline{\xi}(j)$ as "A" or "S". Intensity data would have to be obtained for some twenty values of $\underline{\tau}$.

We have presented the results of several model calculations, and compared them with data from neutron inelastic scattering, Raman and infra-red spectra. Although we have used a χ^2 to describe the fit between experimental and calculated phonon frequencies, we have not attempted a least-squares refinement of the data. Rather, we have pointed out the discrepancies which exist and suggested how they may be resolved. We await, with interest, further experimental measurements of phonon frequencies and cross-sections.

Mode	ξ_1	ξ_2	ξ_3	ξ_4	ξ_5	ξ_6
SR(1)	0	0	0	594	-1828	6805
AR(2)	0	0	0	312	668	-7033
SR(3)	0	0	0	753	6806	1763
ST(4)	6325	3027	-913	0	0	0
AR(5)	0	0	0	3529	6084	734
SR(6)	0	0	0	7006	-577	-767
AT(7)	-2714	6370	1435	0	0	0
AR(8)	0	0	0	6120	-3542	-65
ST(9)	1431	-921	6863	0	0	0
ST(10)	-2818	6324	1437	0	0	0
AT(11)	-3011	159	-6396	0	0	0
AT(12)	-5794	-3065	2652	0	0	0

	A	B	α
C-C	358	42000	3.58
C-D	154	42000	4.12
D-D	57	42000	4.86

Eigenvectors, $\underline{\xi}(j)$, and Potential Parameters of Reference 8.

TABLE 3.1

Mode	$C_{10}H_8$ (cm.$^{-1}$)		$C_{10}D_8$ (cm.$^{-1}$)		
	290°K	77°K	290°K	77°K	
Bg(3)	125	141	118	128	AR(2)
Ag(3)	109	121	102	110	SR(1)
Ag(2 & 1)	74	88	69	82	SR(3)
Bg(2 & 1)	71	83	66	78	AR(5)
Ag(1 & 2)	51	67	49	62	SR(6)
Bg(1 & 2)	46	56	42	53	AR(8)

Raman Frequencies in $C_{10}D_8$
and $C_{10}H_8$ from Reference (51).

TABLE 3.2.

Mode	A(1)	A(2)	A(3)	α(1)	α(2)	α(3)	B(3)
SR(1)	2	11	4	2	34	15	-9
AR(2)	2	14	6	7	39	17	-10
SR(3)	4	10	9	10	24	40	-18
ST(4)	12	19	5	30	41	17	-6
AR(5)	4	15	12	12	24	49	-21
SR(6)	2	11	12	5	42	28	-17
AT(7)	8	10	9	24	30	26	-12
AR(8)	3	26	16	11	48	40	-13
ST(9)	10	17	8	22	35	25	-12
ST(10)	11	22	6	26	45	20	-8
AT(11)	12	24	6	26	45	23	-6
AT(12)	10	21	7	28	45	20	-5

Percentage increase in $(\omega)^2$ for a 25°/o decrease in the A_i's and B(3) and a 3°/o decrease in the α_i's.

TABLE 3.3

Model	A(i)	B(i)	α(i)	χ optic	χ acoustic	χ overall
I C-C	358	42000	3.58			
C-D	154	42000	4.12	10.15	4.87	7.76
D-D	57	42000	4.86			
II	236	27720	3.52			
	61	27720	4.18	4.12	3.23	3.31
	26	23760	4.80			
III	239	28000	3.58			
	103	28000	4.12	2.67	5.72	3.03
	31	28000	4.86			
IV	286	33600	3.58			
	124	33600	4.21	2.40	8.42	3.82
	47	33600	4.78			
V	215	25200	3.58			
	69	25200	4.12	3.17	5.57	3.24
	34	25200	4.86			
VI	156	21840	3.58			
	50	21840	4.18	2.87	6.84	3.48
	21	21840	4.77			
VII	239	28200	3.52			
	63	28200	4.18	3.64	3.87	3.12
	27	20000	4.80			

Values of χ for Various Models

TABLE 3.4

ω_{exp}	ω_{calc}	Δ^2	branch	q
4.1	3.72	22.56	AR(2)	0.0
3.5	3.83	17.00	SR(1)	0.0
2.6	2.68	1.00	SR(3)	0.0
2.44	2.74	25.00	ST(4)	0.0
2.46	2.66	11.11	"	0.1
2.48	2.70	13.44	"	0.2
2.45	2.60	6.25	"	0.3
2.40	2.38	0.11	"	0.4
2.15	1.84	26.70	"	0.5
2.34	2.24	6.25	AR(5)	0.0
2.37	2.25	4.00	"	0.1
2.41	2.33	1.78	"	0.2
2.48	2.44	0.44	"	0.3
2.53	2.55	0.11	"	0.4
2.59	2.64	0.69	"	0.5
1.91	1.89	0.25	SR(6)	0.0
1.90	1.89	0.04	"	0.1
1.86	1.87	0.04	"	0.2
1.82	1.82	0.00	"	0.3
1.78	1.78	0.00	"	0.4
1.84	1.74	2.78	"	0.5
1.62	1.60	0.08	AR(8)	0.0
1.58	1.57	0.03	"	0.1
1.53	1.48	1.00	"	0.2
1.59	1.66	1.36	"	0.3
1.67	1.69	0.11	"	0.4
0.61	0.61	0.00	ST(10)	0.1
1.13	1.03	11.11	"	0.2
1.55	1.36	22.56	"	0.3
1.64	1.54	4.00	"	0.4

ω_{exp}	ω_{calc}	Δ^2	branch	q
0.41	0.40	0.09	AT(11)	0.1
0.78	0.74	1.78	"	0.2
1.17	1.00	32.11	"	0.3
1.51	1.34	18.06	"	0.4
1.69	1.54	9.00	"	0.5
0.29	0.29	0.00	AT(12)	0.1
0.59	0.60	0.11	"	0.2
0.91	0.84	5.44	"	0.3
1.21	1.05	16.00	"	0.4
1.51	1.18	43.56	"	0.5

Frequencies in Thz.

$$\Delta^2 = \frac{(\omega_{exp}(i) - \omega_{calc}(i))^2}{\sigma(i)^2}$$

Observed and Calculated Frequencies

For $C_{10}D_8$ (Model III)

TABLE 3.5

Figure 3.1 Experimental Phonon Frequencies in C_{10} D_8 Altered to Correspond to results for a completely rigid molecule (page 59)

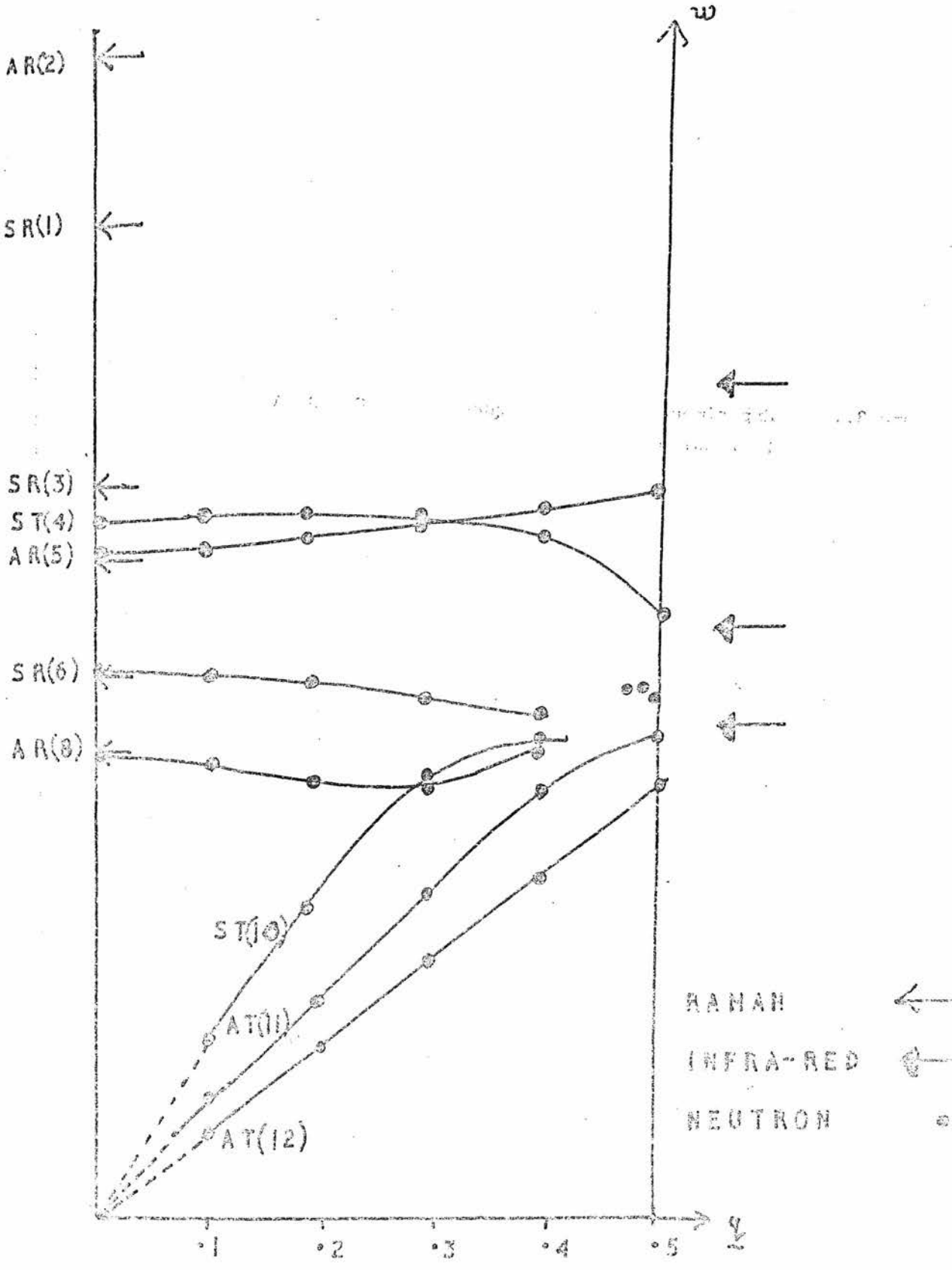
ω
AR(2)
SR(1)
SR(3)
ST(4)
AR(5)
SR(6)
AR(8)
ST(10)
AT(11)
AT(12)
RAMAN
INFRA-RED
NEUTRON
·1
·2
·3
·4
·5
q

FIGURE 3·1

Figure 3.2 The Effect of altering potential parameters on calculated branches of the dispersion curves (page 59)

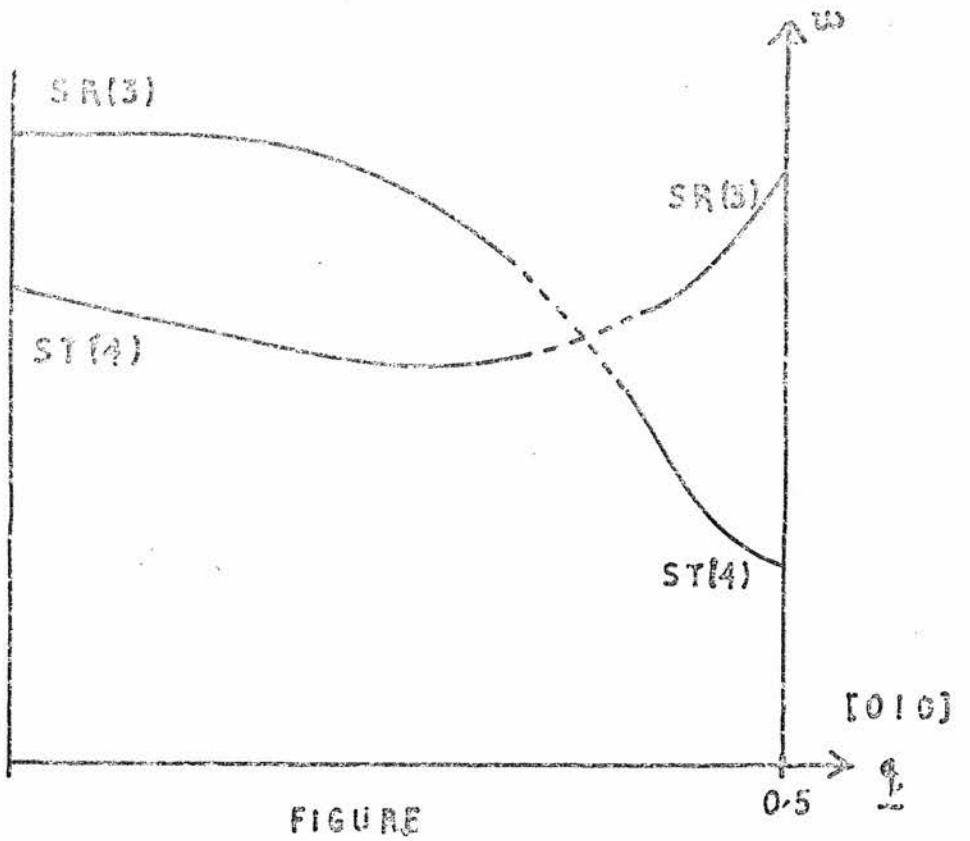

FIGURE
3·2 a

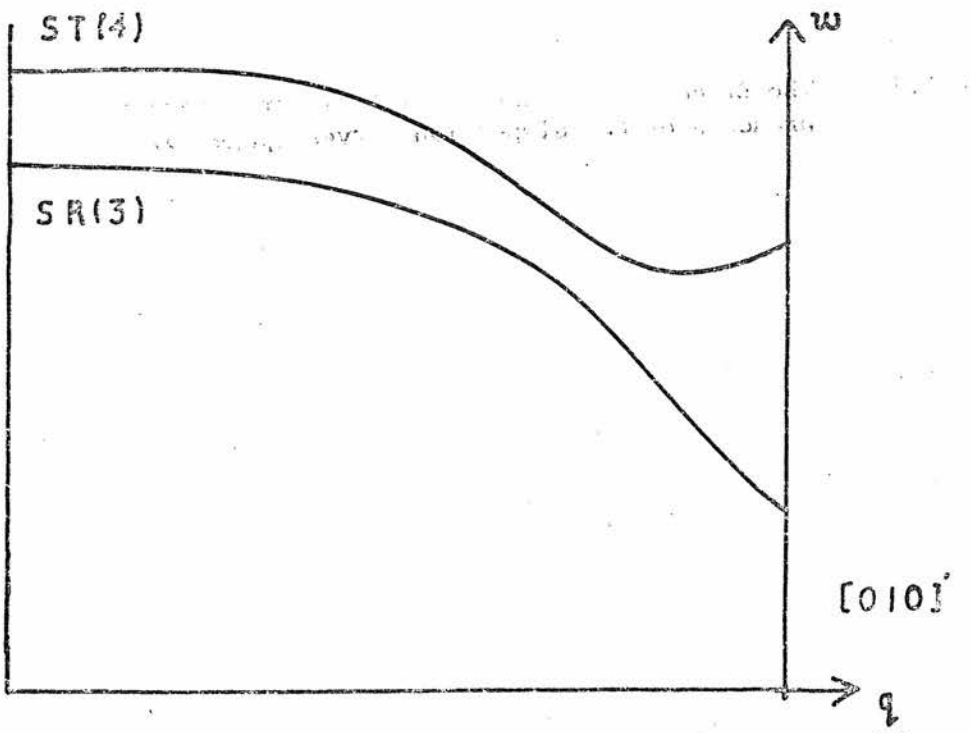

FIGURE
3·2 b

CHAPTER 4

FERRO-ELECTRICITY AND ANTIFERRO-ELECTRICITY IN KH_2PO_4 AND $NH_4H_2PO_4$.

4.1 Introduction

In this chapter we describe the properties of the ferro-electric potassium dihydrogen phosphate (KH_2PO_4) and the anti-ferro-electric ammonium dihydrogen phosphate ($NH_4H_2PO_4$). These materials, along with many other examples of ferro-electrics, have been considered by Kanzig[59] and Megaw[60], and later, from a lattice dynamical view-point, by Cochran[61,62]. It is with Cochran's approach that we are mainly concerned, and this, along with a treatment of the scattering properties of ferroelectric crystals, has been the subject of a review article[63]. The reader is referred to these articles to supplement the necessarily restricted review presented in this chapter.

Ferroelectric crystals exhibit a reversible spontaneous polarization under an applied field, and the direction in the crystal along which the spontaneous polarization occurs is called the polar axis.

As the temperature is increased, the thermal motion of the ions may become sufficient to destroy this spontaneous polarization, and the crystal will revert to normal dielectric behaviour. This high temperature phase is often referred to as the para-electric phase, by analogy with magnetism.

Any phase transition in a ferroelectric may be expected to be accompanied by an anomaly in the static dielectric constant, $\varepsilon(0)$. In some ferro-electrics its behaviour fits the Curie-Weiss relation;

$$\varepsilon(0) = \varepsilon(\infty) + \frac{C}{T-T_c} \qquad (4.1)$$

where $\varepsilon(\infty)$ includes the electronic contribution, and the contribution from the lattice modes whose frequencies retain normal values as $T \rightarrow T_c$ (see Section 4.4 for details). C is the Curie constant, and T_c the Curie temperature. However, many ferroelectric transitions occur for which there is no such hyperbolic increase in $\varepsilon(0)$.

If T_c coincides with the temperature of the structural transition, T_o, then it is a second-order phase transition with a continuous onset of polarization. Otherwise, the transition is first order and has an associated latent heat. In this case the crystal jumps from a state in which the polarization is zero, to one with a finite value for the polarization. These aspects are considered in a thermodynamic theory (see, for example, Devonshire[64]).

We may consider a ferroelectric crystal as an arrangement of parallel dipoles situated at lattice points, but sometimes an anti-parallel arrangement may correspond to a configuration of lower energy. This gives a low temperature phase which is anti-polar. Such a transition may not always be detected by dielectric measurements, and careful structural analysis is required. If the coupling of these anti-parallel dipoles has an energy comparable with that of a polar state, then the crystal is referred to as an anti-ferroelectric. In this case the free energies of the ferroelectric and the antiferroelectric are very similar and applying external stresses, in the form of a very strong electric field, may reduce the polar state free energy to a value below that of the anti-polar state. The crystal would then become a ferroelectric, although the polar

axis may not be in the same direction as the anti-polar.

4.2 The Crystal Structures

a) KH_2PO_4

The structure of KH_2PO_4 both above and below its transition has been investigated, using X-Ray diffraction, by West[65], de Quervain[66] and more recently by Frazer and Pepinsky[67]. In this work, the positions of the hydrogen atoms had to be inferred from those of the oxygens to which they were bonded. It was not possible to confirm the basic hypothesis of Slater's theory of ferroelectricity in KH_2PO_4 - that the hydrogens became ordered in the low temperature phase. Later Bacon and Pease[68] used neutron diffraction to locate the hydrogen atoms in both phases, and established that they did indeed order in the ferroelectric phase.

The room temperature paraelectric phase is illustrated in Figure 4.1. Its space group is $I\bar{4}2d$ with four molecules in the body-centred tetragonal unit cell. Each PO_4 group has its oxygens arranged almost tetrahedrally around the phosphorous atom, and is spaced $\frac{c}{4}$ along the c-direction from neighbouring groups. These are linked through a system of hydrogen bonds, very closely perpendicular to the c-axis. The (0 0 1) Fourier projection obtained from the room temperature data shows the hydrogen nuclei as contours elongated along the O-H-O bond. However, on viewing these contours in the (0 1 0) projection, they are seen to be circular. Bacon and Pease conclude from this that, in the paraelectric phase, the hydrogens either have highly anisotropic vibrations along the bond, or are distributed statistically off-centre in a double potential well with minima

separated by about 0.35Å.

In the low temperature phase, the tetragonal section on (0 0 1) undergoes a shear to become a rhombus. The structure is now described by axes a'b'c' of Figure 4.1, relative to which it has space group Fdd2. (The paraelectric phase has space group $F\bar{4}2d$ relative to the primed axes.) There are now eight molecules in the face-centred unit cell, but the primitive cells of both phases contain the same number of atoms.

The (0 0 1) Fourier projection now shows reduced symmetry for the hydrogen positions. These atoms are now ordered by being displaced asymmetrically towards one of the oxygens in the O-H-O bond. O-H distances are now 1.04Å or 1.41Å, but the distance O-O is almost unchanged. This ordering is accompanied by a slight shear of the oxygen network and K and P atoms move in opposite directions along the c-axis by 0.04Å and 0.08Å.

b) $NH_4H_2PO_4$-

The paraelectric phase of $NH_4H_2PO_4$ has been studied using X-Rays[69] and neutrons[70]. Its space group is $I\bar{4}2d$. The main features of the structure are the same as in KH_2PO_4 with ammonium groups substituted for the potassiums. The NH_4 groups are tetrahedrally connected to four PO_4 groups by N-H-O bonds.

The low temperature antiferroelectric phase has only been studied with X-Rays[71], and great difficulty is caused by the shattering of the crystal, which occurs on passing through the transition. However, the space group has been found to be $P2_12_12_1$. The transition results in a slight orthorhombic distortion of the unit cell of the paraelectric phase. The primitive cell has no longer any body-centred conditions on the

Bragg reflections, and additional reflections appear in the low temperature phase. Some general conclusions on the difference between the two phases can be drawn from the results. The oxygen tetrahedra are greatly distorted on going to the low temperature phase. The nitrogens have large displacements perpendicular to the c-axis, although the corresponding phosphorous displacement is negligible. The hydrogen atoms have not been located, but it may be assumed that they order according to the scheme proposed by Nagamiya[72] and Mason[73], which is illustrated in Figure (4.2).

4.3 The Dielectric Constants as Functions of Temperature

The a-axis and c-axis dielectric constants (ε_a and ε_c) for KH_2PO_4 have values of about 50 at room temperature, but ε_c increases hyperbolically as the temperature approaches the structural transition temperature, T_o. It then drops sharply but continuously on further cooling. ε_a also shows an anomaly at T_o, but this is much less pronounced and is merely a subsidiary effect. The behaviour of ε_c within 50^oK above the transition may be described by a Curie-Weiss Law,

$$\varepsilon_c = \frac{C}{T-T_c}$$

where T_c, the Curie temperature, is identical to T_o.

These dielectric constants show similar anomalies for KD_2PO_4, for which the transition temperature is 213^oK.

In $NH_4H_2PO_4$, a transition occurs at 148^oK which shatters the crystal. Dielectric measurements show that this is not a ferroelectric transition, but leads to an anti-polar phase with the anti-polar direction parallel to one of the a-axes of the

room temperature phase. A large isotope effect is observed, the transition occurring at 245°K in $ND_4D_2PO_4$.

ε_a follows a Curie-Weiss law, with a T_c of - 55°K for $NH_4H_2PO_4$. Measurements allowing us to obtain the value of T_c for the deuterated material have not yet been made. In both materials the on-set of the antiferroelectric transition prevents the ferroelectric phase being reached.

4.4 Ferroelectricity and Low Frequency Modes in Perovskites

To introduce the concept of low frequency modes in ferroelectrics, we consider the perovskite group of ferroelectrics. Since these compounds are not central to our work, we do not include details of various calculations, but refer the reader to the articles quoted. Perovskites all have symmetry m 3 m in their non-polar phase. The perovskite, barium titanate ($BaTiO_3$), makes a ferroelectric transition at 120°C to a tetragonal phase, with point group 4 m m. There are two further transitions; to an orthorhombic phase at 5°C, and to a rhombohedral phase at -90°C. These phases are also ferroelectric, and all three may be described in terms of distortions from the cubic phase.

The tetragonal phase results from an elongation of one edge of the original cube and a compression of the other two. The polar axis is parallel to one of the cubic $\langle 100 \rangle$ directions. The elongation of one face diagonal and compression of the other gives the orthorhombic phase, and an elongation of the body diagonal results in the rhombohedral phase. In these phases the polar directions are along one of the original cubic phase $\langle 110 \rangle$'s and $\langle 111 \rangle$'s respectively.

These phase transitions differ from those in KH_2PO_4 and $NH_4H_2PO_4$ in that the changes in atomic position between the phases are small compared with the unit cell dimensions, and the atoms are ordered in all phases. These are often called displacive transitions.

It was suggested by Cochran[74] that a ferroelectric transition may be accounted for by investigating the lattice dynamics of the crystal concerned. The condition for crystal stability is that the normal modes should have real frequencies, and if the frequency of one normal mode were to approach zero, this would be sufficient to explain the onset of a phase transition.

By considering lattice vibrations in cubic ionic crystals, with N atoms in the unit cell, Cochran[75] has obtained a generalization of the Lyddane-Sachs-Teller relation,

$$\frac{\prod_{n=1}^{N-1} (\omega_n^2)_L}{\prod_{n=1}^{N-1} (\omega_n^2)_T} = \frac{\varepsilon(0)}{\varepsilon(\infty)} \qquad (4.2)$$

where $(\omega_n)_L$ and $(\omega_n)_T$ are the frequencies of the n^{th} longitudinal and transverse optical phonons at $q = 0$. The derivation was made for the rigid ion model, in which the short-range ionic interactions are assumed independent of the polarization of the ions and vice versa.

Equation (4.2) shows that $\varepsilon(0) \rightarrow \infty$ if one transverse optic mode has a frequency which tends to zero as $|\underline{q}| \rightarrow 0$, all other optic mode frequencies retaining normal values.

To discuss the onset of ferroelectricity in $BaTiO_3$, its lattice dynamics should be solved for the shell model[76], which treats each ion as a charged core coupled to a massless charged

shell, representing the outer electrons. This includes the effect of ionic polarization on short-range forces. However, the results are similar to those of the rigid ion model. The transition may be caused by instability against a transverse optic mode of long wavelength. This requires an almost exact cancellation of the short and long-range forces when the atoms vibrate in that particular mode. Suitable choice of the temperature dependence of these lattice dynamical parameters will give the correct behaviour of, for example, the dielectric constant of $BaTiO_3$ as the crystal approaches the transition to the tetragonal phase.

From equation (4.2), it may be seen that, if the frequencies of all other optic modes remain normal, the anomalous phonon mode should have a frequency obeying the relation

$$\omega_T^2 = A(T - T_c)$$

to give a Curie-Weiss behaviour of the static dielectric constant, of the form of equation (4.1). The lattice contribution arises from those modes with frequencies which retain normal values as $T \rightarrow T_c$.

Measurements of the lowest T.O. mode frequency have been made for strontium titanate ($SrTiO_3$)[77] and potassium tantalate ($KTaO_3$)[78] using coherent neutron scattering techniques. We describe the former measurements in more detail in Chapter 6. These, along with infra-red data on additional perovskite crystals, confirm the temperature dependence of $\varepsilon(0)$.

4.5 The Significance of the Eigenvectors

In addition to locating a particular mode in a crystal as it approaches a ferroelectric transition, and measuring the temperature dependence of its frequency, it is of interest to determine the mode eigenvectors.

It has been shown[79] that, if the transition is second-order, there are restrictions on the symmetry of the low temperature phase. The change in any function which is invariant under the crystal space group in each of the two phases must correspond to an irreducible representation of the symmetry group of the high temperature phase. If we consider the electron density as an example, it may be shown[80] that the atomic displacements in the ferroelectric mode are closely the same as the changes in atomic position on going from the non-polar to the polar phase.

If one mode (the ferroelectric mode) has a frequency considerably lower than that of the other modes for which $\underline{q} = 0$, it is reasonable to assume that the relative atomic displacements under an applied electric field should be similar to those in that particular mode. The polarization of the crystal in the ferroelectric phase may then be estimated to compare with the measured value. Methods of deducing these eigenvectors from scattered neutron intensities are described in Chapter 6. Such measurements are an important part of the experimental work on ferroelectrics, as they lead to the actual pattern of vibration in the ferroelectric mode. This is fundamental to many theoretical approaches which attempt to explain the phenomenon of ferroelectricity.

4.6 The Use of Group Theory

The use of group theory considerably simplifies the solution of general lattice dynamical problems. To determine the crystal normal modes requires the finding of the eigenvalues and eigenvectors of an $n \times n$ dimensional dynamical matrix (Section 1.1). One of the basic tenures is that the effect of applying one of the space group operations to a crystal vibrating in a particular normal mode is to produce a crystal displaced through that specific operation with its atoms vibrating in such a pattern, that the new system is identical to the undisplaced crystal vibrating under a linear combination of normal modes, degenerate in energy with the original mode. This allows us to choose normal modes which transform according to the irreducible representations of the crystal space-group.

For a vibration with wave vector at a symmetry point, $\underline{q}$, use of the group irreducible character table allows us to determine the number of normal modes in each irreducible representation. Since sets of basis vectors for these irreducible subspaces have been listed for many of the thirty-two point groups, the normal modes are easily expressed as linear combinations of these vectors. In particular the dynamical matrix is automatically block diagonalized when referred to these vectors as basis. These blocks are of dimension c_s, the number of occurrences of each irreducible representation. Since this is usually small, it is a relatively simple matter to obtain the eigenvalues and eigenvectors.

For a crystal making a ferroelectric or antiferroelectric transition as a result of a "condensed" or soft mode, the results of group theory allow us to deduce useful

information without solving the complete lattice dynamical problem. Since the soft mode must occur for a q-value with point group symmetry permitting more than the identity operator, it cannot occur at a general point of the Brillouin zone. It may be shown that a ferroelectric mode must occur at the zone centre and an antiferroelectric mode at the zone boundary. If the symmetry of the low temperature phase is known, since the soft mode in the high temperature phase must be compatible with this, it is possible to deduce the irreducible representation to which the mode belongs. Without actually finding the explicit combination of basis vectors which gives the soft mode eigenvector, restrictions on the atomic motions may be deduced from the list of basis vectors.

Montgomery[81] treats the 3r-dimensional space spanned by the normal modes as the product of an r-dimensional "cell-space", S_C, and a 3-dimensional Euclidean space, S_E. He then finds the irreducible representations (ir's) of these separate spaces and hence those of the product space, $S_C \times S_E$. The effect of a symmetry operation is to rotate the polarization vectors as well as to attach them to different sites in the crystal, and this treatment allows rotation of the vectors in Euclidean Space, accompanied by the permutation of atoms in cell space with the addition of phase factors. It is then often immediately obvious which atoms vibrate and what is the nature of their vibration in the soft mode.

We now consider a specific example - the ferroelectric mode in KH_2PO_4, treated by Shur[82] and also Montgomery[83]. The transition is associated with an ordering of the hydrogens only, this suggests they may be treated as a pseudo-spin system and all other atomic motions in terms of phonon

co-ordinates. It is for those atoms experiencing phonon-like displacements that the factorization into S_E and S_C is useful.

$$S_V = (S_P + S_K + S_O) \times S_E \quad . \qquad (4.3)$$

The S_P, S_K, S_O are invariant subspaces each of which is spanned by vectors belonging to equivalent atomic sites. Their dimensions are two, two and eight respectively, there being twelve heavy atoms in the unit cell.

The character of each subspace is

$$\chi_o(\gamma) = \sum_K \delta_{K,\gamma K} \exp -i \; \underline{K}_{\gamma^{-1}} \cdot \underline{X}_K \quad ;$$

$\underline{K}_{\gamma^{-1}} = \gamma^{-1} \underline{q} - \underline{q}$, a reciprocal lattice vector, γ the rotation caused by operation of a space group element, and translation $\underline{X}_\gamma$ shifts an atom from site K to γK, the summation being over all atoms of the same chemical species. For $\underline{q}$ at a symmetry point, the number of occurrences, c_s, of each of the s irreducible representations in the decomposition of the subspace with characters $\chi_o(\gamma)$ is

$$c_s = \frac{1}{h} \sum_\gamma \overline{\chi_o^s}(\gamma) \chi_o(\gamma) \quad .$$

The $\overline{\chi_o^s}(\gamma)$ are the irreducible characters of the point symmetry group concerned, and h the number of its members.

For the $\Gamma(0, 0, 0)$ point in KH_2PO_4 there are five irreducible representations

For S_K and S_P, $c_1 = c_2 = 1$, $c_3 = c_4 = c_5 = 0$

and for S_O, $c_1 = c_2 = c_3 = c_4 = 1$, $c_5 = 2$.

The decomposition of S_E under the various symmetry groups is found by studying the transformation properties of functions x, y, z, In this case S_E transforms as $\Gamma_4 + \Gamma_5$. So $(S_C \times S_E)(\Gamma)$ transforms as:-

$$((\Gamma_1 + \Gamma_2)_K + (\Gamma_1 + \Gamma_2)_P + (\Gamma_1 + \Gamma_3 + \Gamma_4 + 2\Gamma_5)_O) \times (\Gamma_4 + \Gamma_5)$$

$$= 3\Gamma_1 + 3\Gamma_2 + 5\Gamma_3 + 5\Gamma_4 + 10\Gamma_5 \quad .$$

Since Γ_1 and Γ_2 result from the product $S_O \times S_E$ only, they correspond to modes in which only oxygens move, whereas Γ_3, Γ_4 and Γ_5 involve motions of all the heavy atoms. Γ_3 and Γ_4 involve the products of S_K and S_P with the Γ_4 i.r. of S_E only, the z-direction, and in these modes K and P are constrained by symmetry to vibrate along z only. Similarly in modes belonging to Γ_5 K and P atoms vibrate in the x-y plane only, which corresponds to the Γ_5 i.r. of S_E. Since Γ_3, Γ_4 and Γ_5 turn up in products of S_O with $\Gamma_4 + \Gamma_5$, the oxygens have perfectly general motions. These restrictions could have been expected "intuitively" since K and P occupy special positions in the unit cell space, whereas oxygens are in general positions.

The hydrogen atoms are treated independently and Montgomery shows by considering the eigenvectors of the proton Hamiltonian,

$$\mathcal{H} = -2\Omega \sum_i X_i + \tfrac{1}{2} \sum_{ij} J_{ij} Z_i Z_j$$

where Ω is the "tunnelling integral" and J_{ij} represents interaction between the various hydrogen sites, that they span the irreducible subspaces:-

$$\Gamma = \Gamma_2 + \Gamma_4 + \Gamma_5 \quad .$$

At the M-point the i.r.'s are

$$M = M_{34} + M_5 ,$$

At both Γ and M these are unique representations and the symmetry of the proton tunnelling modes is completely determined.

The coupling of these tunnelling modes to the lattice modes involving the heavy atoms has been considered by Kobayashi[84] and is described in Section 4.8. However, in (83) the result that coupling can only occur between modes of the same symmetry is used to find which coupled mode corresponds to the ferroelectric mode. This restriction is a consequence of demanding that the composite modes transform irreducibly under the crystal space group.

The pattern of proton displacements in the mode Γ_2 has all four hydrogens approaching a PO_4 group simultaneously. This must have a high frequency and cannot be a candidate for the ferroelectric mode. Some Γ_4 and Γ_5 modes in which K and P atoms vibrate with an accompanying polarization have their frequencies affected by depolarizing fields. However, the Γ_4 mode with $\underline{q} \to 0$ along x has polarization along z and will be unaffected by a depolarizing field. Montgomery argues on stability grounds that it is this mode which becomes unstable, and the arguments above determine the pattern of atomic vibrations in this mode. The hydrogen displacements in Γ_4 are illustrated in Figure (4.3).

In $NH_4H_2PO_4$ Sirotin[85] has argued that the antiferroelectric mode has M_{34} symmetry and the motion of the heavy atoms will be described by modes spanning the i.r. M_{34}. We consider the product space $(S_N + S_P + S_O) \times S_E$

where S_N and S_P transform as M_5 and S_O as $(M_{12} + M_{34} + 2M_5)$. S_E transforms as $\Gamma_4 + \Gamma_5$. Since M_{34} in $S_C \times S_E$ arises from products of $(M_5)_N$ and $(M_5)_P$ with Γ_5 only, the atoms N and P vibrate in the x-y plane in M_{34} modes. The oxygen atoms must be allowed general motions.

The hydrogens of the ammonium group should be treated along with the heavy atoms, since they are ordered in both phases, by introducing an 8-dimensional subspace, S_D. However, since they are in general positions crystal symmetry cannot place any restrictions on their motion in the M_{34} modes. The hydrogen motions in the antiferroelectric mode follow the pattern illustrated by Montgomery[83] or that postulated by Nagamiya[72]. We use these results in Chapter 6.

4.7 Experimental Evidence for Low Frequency Modes in KH_2PO_4.

a) Raman measurements

The first quantitative measurements of the predicted low frequency temperature dependent mode in KH_2PO_4 were reported by Kaminov and Damen[86]. They recorded the Raman spectral density, $J(\omega)$, over a temperature range extending from well above the transition temperature to 40^oK below T_c. In addition to the normal Rayleigh line, these spectra showed a temperature dependent part which increased in strength and became narrower in ω as $T \rightarrow T_c$ (see Figure 4.4). Below T_c this part broadened and quickly weakened to virtually disappear at 82^oK.

The experimental arrangement allowed only contributions

to $J(\omega)$ from modes of the same symmetry as the polarization, P_Z. The complex susceptibility derived from $J(\omega)$ was fitted satisfactorily to a damped oscillator function and is

$$\chi_Z(\omega) = \frac{\omega_o^2 \chi(0)}{\omega_o^2 - \omega^2 + 2i\Gamma\omega} \quad .$$

Γ was independent of temperature and $\chi(0)$ and ω_o were simple functions of temperature

$$\chi(0) = \frac{C}{T-T_c} \quad , \qquad \omega_o = A\left(\frac{T-T_c}{T}\right)^{\frac{1}{2}} \quad .$$

This temperature dependence of ω_o is consistent with the soft-mode model described in Section 4.4 or with a pseudo-spin tunnelling model. The soft mode frequency predicted by Cochran[62] from the atomic displacements measured by Bacon and Pease[68] is identical to the ω_o which fits $\chi_z(\omega)$ at room temperature. The uncoupled tunnelling frequency should correspond to the fitted ω_o at high temperatures. Measurements on various samples showed that all frequencies are reduced with increasing deuteration, although the behaviour is qualitatively the same as in KH_2PO_4. For high damping, the peak in the imaginary part of $\chi_z(\omega)$ occurs at $\omega_o^2/2\Gamma$ which has the value $0.7\ cm^{-1}$ at room temperature.

b) Coherent Neutron Scattering Data

These measurements, using a triple-axis crystal spectrometer, were made on KD_2PO_4 almost simultaneously by groups at Chalk River[87] and Brookhaven[88]. The results of[87]

showed that there was no well-defined peak in the phonon spectrum whose frequency had the required temperature dependence for a ferroelectric mode. This was in complete contrast to the results for $SrTiO_3$[77] and $KTaO_3$[78], but was consistent with the conclusions of (86).

Strongly temperature dependent quasi-elastic scattering was detected in the $\underline{a}^* - \underline{c}^*$ plane around the Γ-point. We shall describe this type of scattering in more detail in Chapter 5. From the shape of its intensity contours it could be deduced that this scattering was from ferro-electric fluctuations and it had an energy spread less than the instrumental resolution. This corresponded to a $1/\tau$ of less than 0.02 THz. and so had a longer time scale than all but the very long wavelength acoustic phonons. The temperature dependence of the intensity was

$$I = BT/(T-T_c)$$ down to the transition and fell

rapidly below the transition. This can be interpreted as scattering from an overdamped mode whose undamped frequency varies as $(T-T_c)^{\frac{1}{2}}$.

Skalyo et al.[88] measured this intensity at some sixty points in reciprocal space and used the results of Section 4.6 to fit the atomic displacements in the ferroelectric mode, by finding the linear combination of the seven basis vectors of the Γ_4 representation. This work confirmed that the ferroelectric mode has the symmetry predicted by Montgomery[83]. However, they showed that the displacements did not correspond to the differences in atomic position between the structure immediately above and below the transition, although these provided a good starting point for the model refinement.

4.8 Coupled Phonon and Tunnelling Modes in KH_2PO_4 and Kobayashi's Theory

It is completely artificial to consider the protons in KH_2PO_4 tunnelling in isolation, unaffected by the other atoms in the lattice. In Section 4.6 we considered only the symmetry of coupled modes; in this section we extend our discussion.

It was suggested by Cochran[62] that the tunnelling mode couples to a low frequency optic phonon mode, which behaves as the ferroelectric mode in perovskites. Further work has shown that it is likely that it is the tunnelling mode which has the expected temperature dependence, and the phonon mode, to which it couples, which gives the c-axis electric moment. Since the proton ordering is almost completely in the a - b plane this could not give any polarization along c .

Kobayashi[90] has considered the coupling of a proton tunnelling mode to an optical phonon mode in which $K - PO_4$ groups vibrate along c, and this is included in a review article[63]. The Hamiltonian consists of three terms

$$\mathcal{H} = H_P + H_{P,L} + H_L \quad .$$

H_P is the tunnelling model Hamiltonian. In the pseudo-spin model of de Gennes[91]

$$H_P = -2\Omega \sum_\ell X_\ell - \tfrac{1}{2} \sum_{\ell\ell'} J_{\ell\ell'} Z_\ell Z_{\ell'}$$

where X_ℓ, Z_ℓ are components of pseudo-spin and the "field" 2Ω is the separation of the energy levels in the ground state of the proton tunnelling system. In terms of Fourier components,

$$S(\underline{q}) = 2N^{-\frac{1}{2}} \sum_{\ell} Z_{\ell} \exp(-i\underline{q}.\underline{r}_{\ell})$$

$$S^{o}(\underline{q}) = N^{-\frac{1}{2}} \sum_{\ell} X_{\ell} \exp(-i\underline{q}.\underline{r}_{\ell}) \quad .$$

This may be written

$$H_P = -2\Omega N^{\frac{1}{2}} S^{o}(0) - \frac{1}{8} \sum_{\underline{q}} J(\underline{q}) S(\underline{q}) S(-\underline{q}) \quad .$$

In mean-field and random phase approximations it may be shown that $S(\underline{q})$ has a time dependence, with characteristic frequency $\Omega_o(\underline{q})$ where

$$\hbar^2 \Omega_o^2(\underline{q}) = 2\Omega(2\Omega - J(\underline{q}) \langle S^{o} \rangle) \qquad (4.4)$$

and $\langle S^{o} \rangle = \frac{1}{2} \tanh \beta\Omega$.

It is postulated that

$$H_{PL} = \sum_{\underline{q}j} G_j(\underline{q}) S(-\underline{q}) Q_j(\underline{q})$$

for coupling to several lattice modes. H_L has the usual form (equation (1.7)). The tunnelling mode frequency, for small Ω, becomes zero at the transition temperature

$$T_o' \quad \text{where} \quad k_B T_o' = \frac{1}{4} J(0) \quad .$$

The coupled mode frequencies may be shown to satisfy

$$\hbar^2(\omega^2 - \Omega_o^2(\underline{q}))(\omega^2 - \omega_j^2(\underline{q})) = 8\Omega |G_j(\underline{q})|^2 \langle S^{o} \rangle \qquad (4.5)$$

where $\omega_j(\underline{q})$ is the uncoupled frequency of the single lattice mode to which we assume the tunnelling mode couples. The solutions, $\omega_+(\underline{q})$ and $\omega_-(\underline{q})$, say, satisfy $\omega_+(\underline{q}) > \omega_j(\underline{q})$ and $\omega_-(\underline{q}) < \Omega_o(\underline{q})$. Since $\omega_j(\underline{q}) \gg \Omega_o(\underline{q})$ near T_o',

$\omega_j(\underline{q}) \gg \omega_-(\underline{q})$ so that $\omega_+(\underline{q}) \approx \omega_j(\underline{q})$, and is mainly phonon-like. The ω_- mode is a predominately tunnelling-like mode and we may set $\omega_-(\underline{q}) = \Omega(\underline{q})$. If the transition occurs for a mode with $\underline{q} = 0$, at $T = T_c$, then equations (4.4) and (4.5) combine to give

$$4\Omega - J(0) \tanh \frac{\Omega}{k_B T_c} - \frac{4G_j^2(0)}{\omega_j^2(0)} \tanh \frac{\Omega}{k_B T_c} = 0 \quad .$$

If Ω is small enough, this gives

$$k_B(T_c - T_o') = \frac{G_j^2(0)}{\omega_j^2(0)} \quad .$$

T_o' is the Curie temperature for an isolated proton system, and the proton-lattice interaction raises this to T_c, the "system" Curie temperature. The coupled frequency $\Omega(0)$ tends to zero as $(\frac{T-T_c}{T})^{1/2}$.

This $\Omega(0)$ mode is that illustrated by Cochran[62] and shown in Figure (4.5), and is the ferroelectric mode. The ω_+ mode remains almost unchanged as $T \to T_c$ and has the same pattern of proton motion as $\Omega(0)$ but K and P approach each other and so this mode has a much higher frequency.

Kobayashi makes a rough calculation to estimate $T_c - T_o'$, including only Coulomb interactions between protons and lattice, and obtains a value of 10^oK for KH_2PO_4. He concludes that the isotope effect on T_c occurs from T_o' through a change in Ω on deuteration. The small changes in T_c on replacing K by Rb or Cs, he attributes to changes in the term $\frac{G_j^2(0)}{k_B\omega_j^2(0)}$ which he has shown to be small.

However, Cochran estimates $T_o' \approx 0^oK$ for KH_2PO_4 and Buyers

et al.[87] obtain a value - 700°K for KD_2PO_4. The latter estimate is expected to be inaccurate by a factor of $2 \rightarrow 3$ as it is evaluated through the dielectric constant, assuming, for example, that the deuteriums move perpendicular to c. Both of these results disagree strongly with Kobayashi's estimates. The difference between T_o' for tunnelling and no tunnelling is only 14°/o, which implies, in contradiction to Kobayashi's results, that it is the proton-lattice interaction which mainly determines T_c.

It is easily seen what is wrong with Kobayashi's estimates. The Coulomb contribution to the proton-lattice interaction summed over all proton sites should be zero, and it is the short-range interactions which govern the value of $G_j(0)$ and hence $T_c - T_o'$.*

* Private communication from Professor R.A. Cowley.

Figure 4.1 The room temperature paraelectric phase of KH_2PO_4 (page 68)

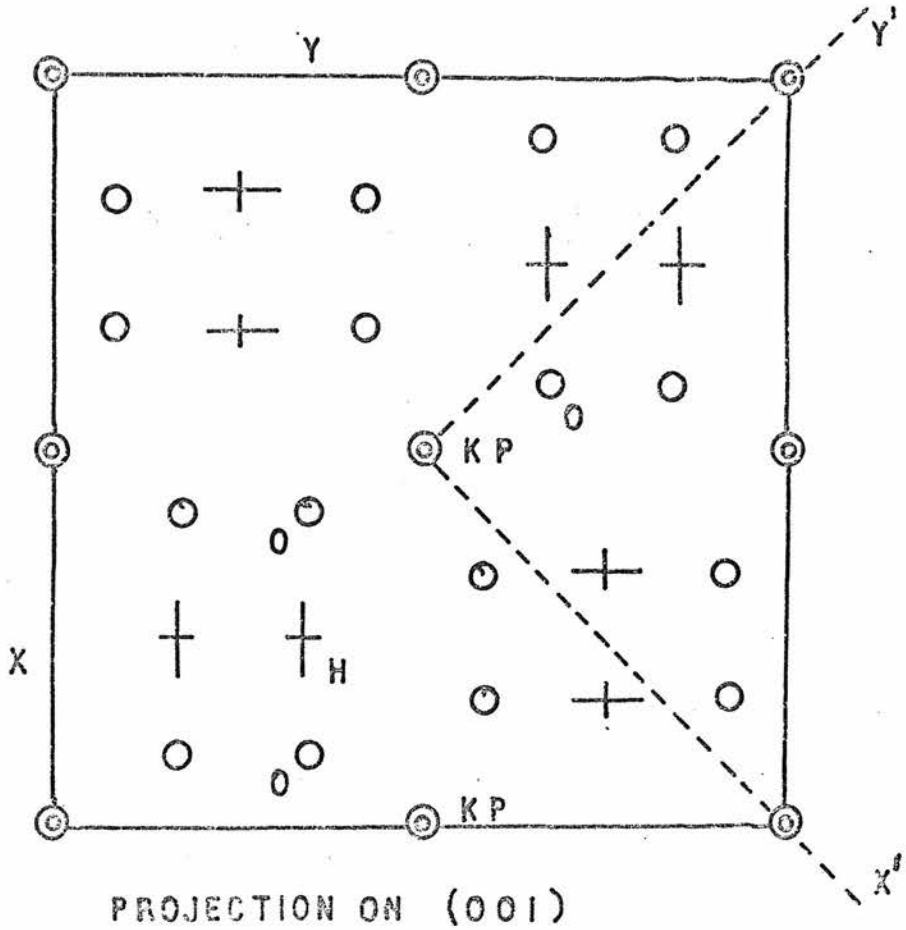

PROJECTION ON (001)

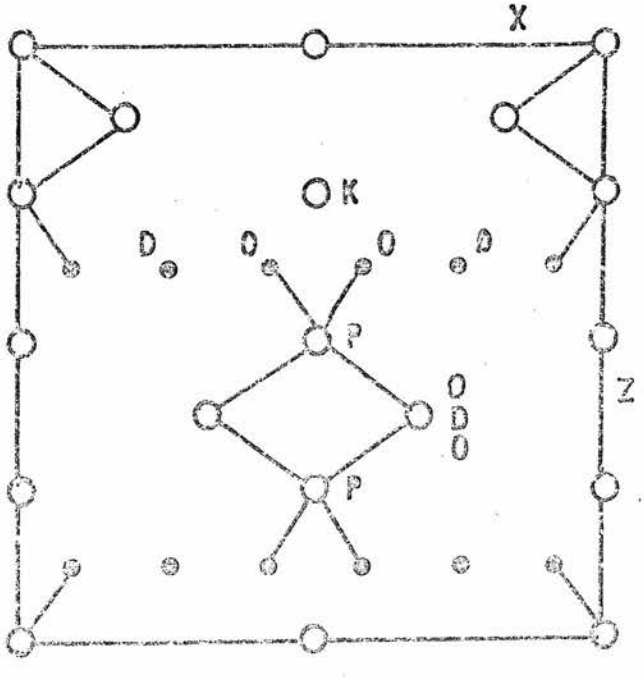

PROJECTION ON (010)

FIGURE 4-1

Figure 4.2 Ordering Scheme for hydrogen atoms in anti-ferroelectric mode (page 70)

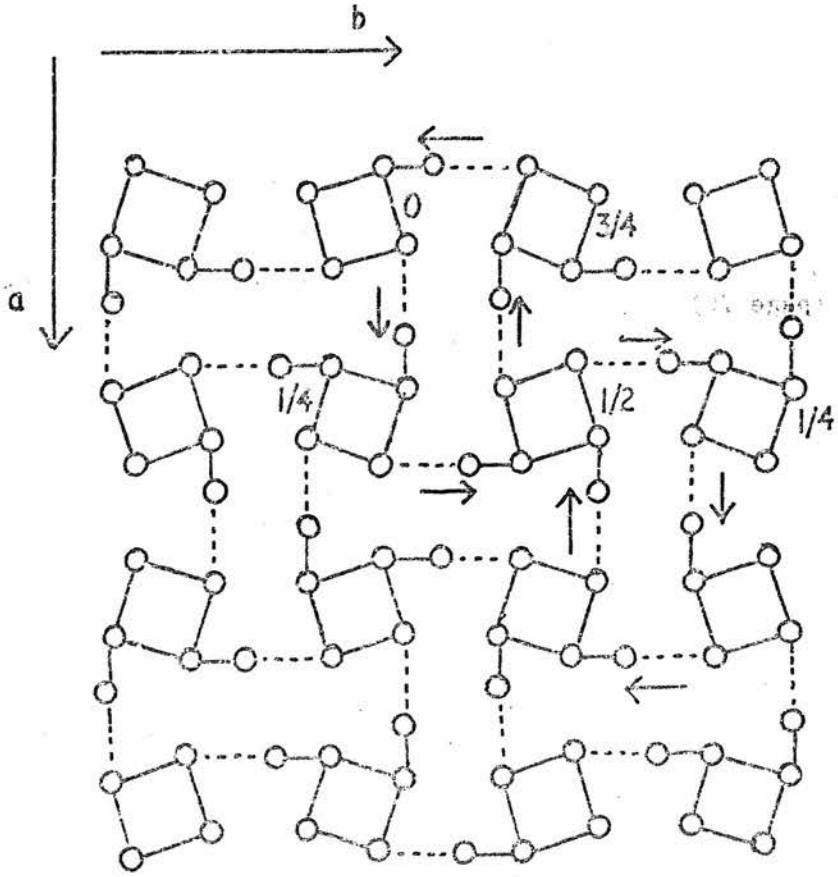

arrows show displacement of hydrogens
heights of PO_4 groups shown

FIGURE 4-2

Figure 4.3 Ordering scheme for hydrogen atoms in ferroelectric mode (page 79)

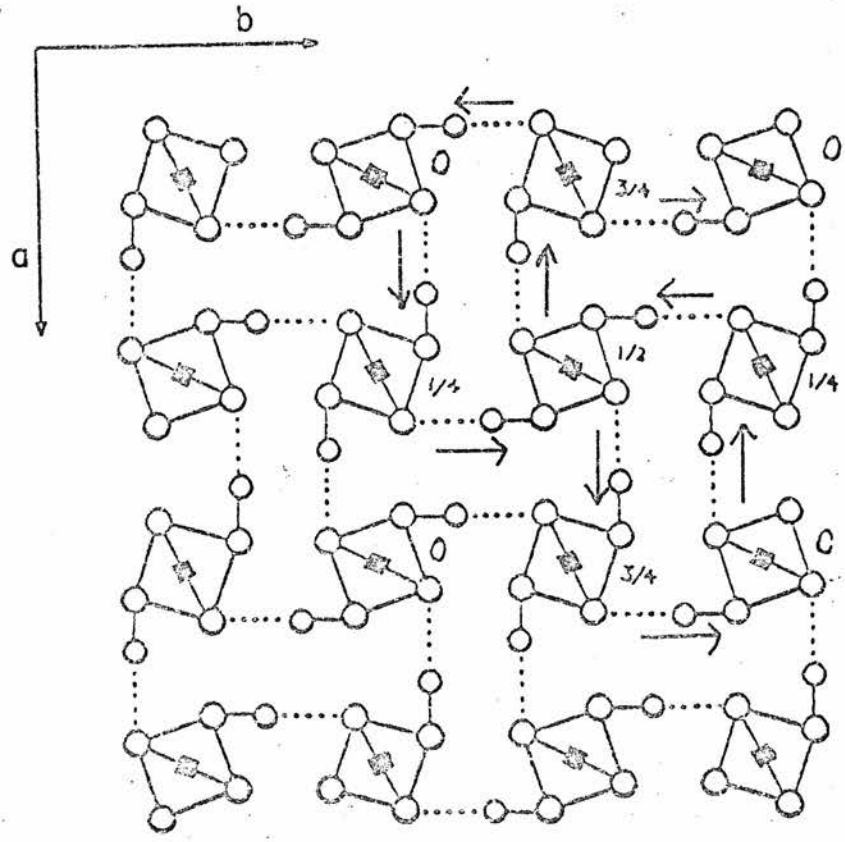

FIGURE 4.3

Figure 4.4 Raman Spectral Density ($J(\omega)$) for KH_2PO_4 (page 80)

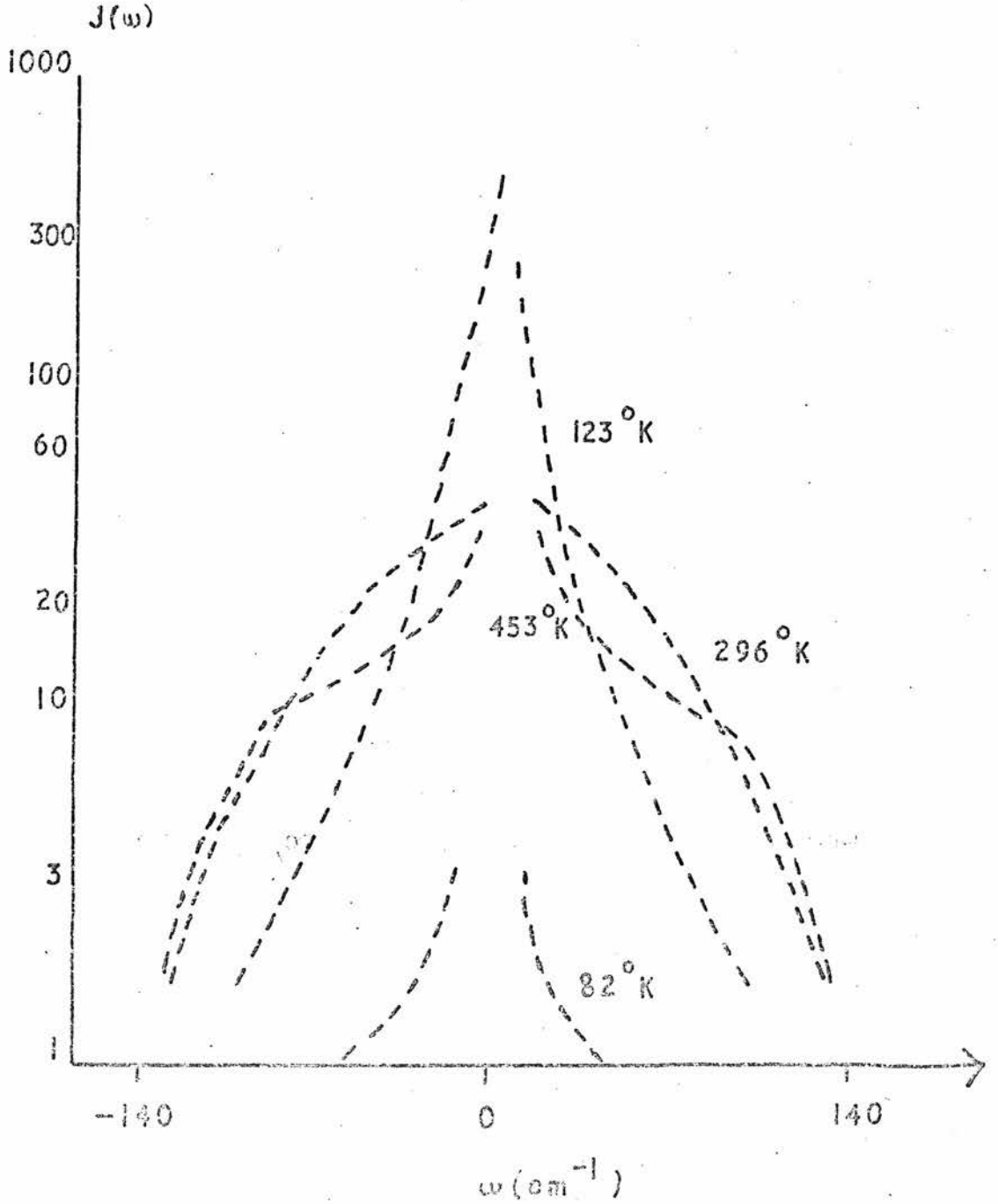

FIGURE 4·4

Figure 4.5 Displacements of atoms in the ferroelectric mode in KH_2PO_4 (page 85)

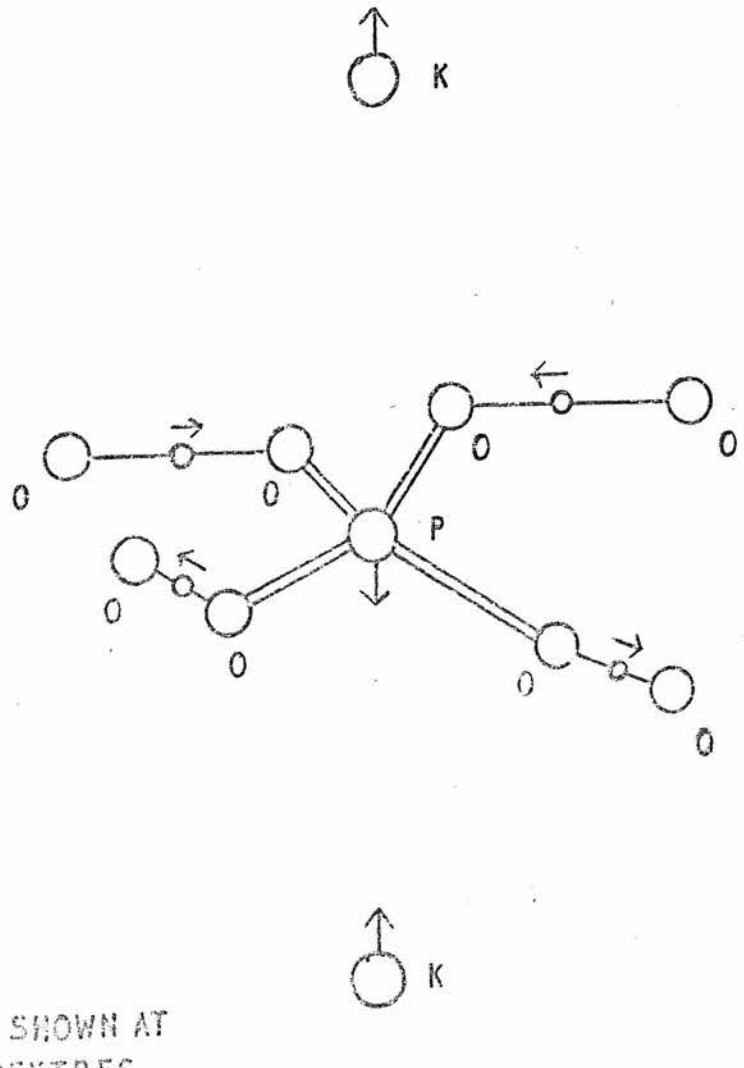

FIGURE

4·5

CHAPTER 5

EXPERIMENTAL MEASUREMENTS ON DEUTERATED AMMONIUM DIHYDROGEN PHOSPHATE ($ND_4D_2PO_4$)

Although complete dispersion curves have not yet been obtained for $ND_4D_2PO_4$, some neutron scattering measurements have been reported[92], and we now describe our experimental results for that material.

Acoustic modes have been located with $\underline{q}$ along $\underline{a}^*$ and $\underline{c}^*$ in independent investigations - by Meister et al.[92], and by the present author. No well-defined soft phonon mode has been found, but critical scattering in the form of quasi-elastic intensity from an overdamped mode has been detected[92] at the M-points of 29 Brillouin Zones, and we have extended these measurements. In addition, we have found evidence of quasi-elastic scattering by a zone-centre mode.

5.1 Experimental

The neutron scattering measurements on $ND_4D_2PO_4$ were all made using the Pluto triple-axis crystal spectrometer. The tetragonal structure of this crystal makes the $\underline{a}$ and $\underline{b}$ axes equivalent, and the $\underline{a}^* - \underline{c}^*$ plane was used as the scattering plane throughout by mounting the crystal with one of the equivalent $\underline{a}^*$ axes vertical, say (0 1 0). We illustrate this plane in Figure 5.1 where one Brillouin zone has been drawn to show the Γ -point ($(h+\ell)$ even) and an M-point ($(h+\ell)$ odd). We have measured phonon frequencies for $\underline{q}$-values throughout the zone, but the majority of our results were for $\underline{q}$ close to a Γ or M-point, i.e. around the zone centre or the zone

boundary.

The crystal on which all our measurements were made was supplied with a specified 98% deuteration, although data on other crystals from the same source has suggested that this level may only be 93%. The crystal was a rectangular parallelepiped of volume 30 cc. To prevent deuterium exchange with hydrogen in the atmosphere the sample was initially mounted in an aluminium can. Unfortunately it was found that, with the spectrometer set to observe quasi-elastic scattering, the aluminium Debye-Scherrer lines were sufficiently strong to give a significant counting rate in the detector. For the later experiments the crystal was wrapped in thin aluminium foil for which the Debye-Scherrer lines were of negligible intensity compared with the scattered intensity from processes of interest in the crystal.

It was known from structure work that the lengths a and c are almost identical in $NH_4H_2PO_4$ and that it would be difficult to distinguish between them when orientating the crystal. However the crystal symmetry causes Bragg absences for (0 0 2), (0 0 6) .... and with the incident neutron wavelength chosen so that second order processes were negligible, these systematic absences were sufficient to distinguish between the axes. A calculation of expected Bragg intensities showed that (2 0 0) and (6 0 0) should be strong and could not be confused with second order (0 0 4) and (0 0 12) reflections. The lattice parameters were determined accurately by stepping the crystal table for many values of detector angle, 2θ, round the approximate Bragg positions. The peak heights for these scans were plotted against 2θ, and the best value of θ was found from the half width. The corresponding lattice

parameters were found to be $a = (7.485 \pm 0.005)$ and $c = (7.50 \pm 0.005)$Å. The crystal had a mosaic spread of 0.35° half width at half maximum (H.W.H.M.) against the (1 1 1) planes of an aluminium monochromator.

The spectrometer had aluminium monochromator and analyser with a Soller slit collimation of 0.8° F.W.H.M. between monochromator and sample and 0.6° F.W.H.M. between sample and analyser. The collimation of the analysed beam was 4°, and that of the incident beam on the monochromator was relaxed.

With this collimation, the energy resolution of the instrument was found by energy analysing the incoherent elastic scattering from a vanadium sample with the same vertical cross-section as the $ND_4D_2PO_4$ crystal. A least-squares fit of these scans to a Gaussian gave (0.55 ± 0.02) THz. F.W.H.M. for 1.4Å neutrons reflected from the (3 1 1) planes of analyser and monochromator, and (0.35 ± 0.02) THz. for 1.4Å neutrons from the (3 3 1) planes. Since these values are in very good agreement with equation (1.19), this expression can be used to find the energy resolution for any other sets of parameters.

As $(h^2 + k^2 + \ell^2)$ of the aluminium planes increased, their reflectivity of neutrons decreased so that the number scattered in unit time from the (1 1 1), (3 1 1) and (3 3 1) planes was in the ratio 8 : 4 : 1. This considerably increases the time required to obtain a given number of counts in the detector under better resolution, but there is an accompanying increase in the peak to background ratio.

There was a germanium analyser available which gave (0.54 ± 0.02)THz resolution with 2Å neutrons reflected from the (1 1 1) planes of an aluminium monochromator and analysed

by the germanium (1 1 1)'s. The reflectivity of these germanium planes was one quarter that of the aluminium (3 1 1) planes, and so no benefit could be obtained by using this particular germanium crystal.

Considerable difficulty was caused by the insufficient deuteration of the sample, as the few percent hydrogen present gave a strong incoherent background. Although its K-dependence enabled us to subtract the incoherent intensity, it did cause uncertainty in the measurement of the intensity of coherent scattering processes in the crystal.

The instrumental resolution chosen depended on the type of measurement in progress. Low resolution could be used for quick preliminary scans, and to energy integrate quasi-elastic scattering. High resolution was necessary in making detailed measurements close to Bragg reflections, and for energy analysis of the scattering. In all our measurements λ was sufficiently low so that the number of $\lambda/2$ neutrons arriving at the sample was negligible.

5.2 Measurement of Quasi-elastic Intensity round the M-point in $ND_4D_2PO_4$.

We now describe the additional measurements which we have made of scattered neutron intensity from the $ND_4D_2PO_4$ anti-ferroelectric mode. The triple-axis spectrometer was used in the constant-E mode, with the energy transfer set at zero to measure only quasi-elastic intensity. Since the scattering has q at the zone boundary, all other phonons have energies greater than 1 THz, and there is no Bragg scattering to be subtracted. Consequently, there was no need to use high K

or ω resolution, and we chose the experimental conditions to maximise the scattered intensity. Most of the measurements used 1.3Å neutrons reflected from the (3 1 1) planes of the aluminium monochromator and analyser. In all, 9 M-points were investigated, two of these being repeats of measurements by Meister et al. to allow both sets of intensities to be put on the same scale.

Intensity measurements for a net around six of these M-points were sufficient to draw a complete set of intensity contours in these regions of the $\underline{a}^*$ - $\underline{c}^*$ plane. The net was constructed by measuring intensity at intervals of $0.1\underline{c}^*$ or $0.05\underline{c}^*$ along lines parallel to $\underline{c}^*$ and spaced by $0.025\underline{a}^*$. These measurements were typically over the region $(\xi$ -0.2, 0, η -0.5); $(\xi$ -0.2, 0, η +0.5); $(\xi$ +0.2, 0, η -0.5); $(\xi$ +0.2, 0, η +0.5). At the remaining M-points, the intensity was recorded along a line, parallel to $\underline{c}^*$ and passing through the M-point.

The contours around (5 0 4) and (5 0 8) may be taken as typical of our scans and we illustrate these in Figures 5.2a and b. Figure 5.2a is of interest since it may be compared with the measurements of reference (92). These were at 244°K with 0.17 THz. resolution and our data were obtained at 297°K with energy resolution 0.55 THz. The quasi-elastic contours, with their strong $\underline{q}$-dependence, are superposed on a high background, mainly incoherent elastic scattering. This background was measured at $(\xi$ -0.5, 0, $\eta)$ and $(\xi$ +0.5, 0, $\eta)$, i.e. halfway between quasi-elastic contours of $(\xi$, 0, $\eta)$ and Bragg contours of $(\xi+1, 0, \eta)$ and $(\xi$ -1, 0, $\eta)$. From these measurements, the background close to $(\xi$, 0, $\eta)$ could be estimated.

The finite energy resolution of the spectrometer could be assumed to perform the energy integration, and the relative intensities of the mode at different M points could be obtained by comparing measured intensities for a particular $\underline{q}$. It may be seen from Figures 5.2a and b that the scattering around a given M point does not vary rapidly with $\underline{q}$, and the shape of the contours is the same at different M-points. The inner contours approximate to ellipses, and the outer have a slight dumb-bell shape.

The half-widths at half maximum of the ellipse along $\underline{a}^*$ and $\underline{c}^*$ (x_o and y_o respectively) were found to depend on the instrumental resolution. As λ decreased from 1.3Å to 1.1Å, x_o increased from 0.075 to 0.095 reciprocal lattice units, and y_o from 0.4 to 0.5. The ratio x_o/y_o remained independent of resolution.

These results show that the intensity contours of the quasi-elastic scattering are, as expected, elongated along $\underline{c}^*$ with very little intensity perpendicular to $\underline{c}^*$, i.e. they are consistent with scattering from fluctuations polarized predominantly in the $\underline{a}^* - \underline{b}^*$ plane. The ratio y_o/x_o was $16/3$.

The intensity, integrated over $\underline{q}$, is given for several M points in Table 5.1. These values may be compared with column 2 of the same table, which gives the intensity at $\underline{q}' = 0$ (measured from the M point), to show that the peak intensity is proportional to the integrated intensity (within experimental error). This merely shows that the mode eigenvectors do not vary rapidly with $\underline{q}$ near $\underline{q}' = 0$.

5.3 The $ND_4D_2PO_4$ Γ -point Scattering

Dielectric constant measurements on $NH_4H_2PO_4$ [93] have shown that ε_a has a temperature dependence of the form $A/(T - T_c)$ with $T_c = -55^oK$. As this cannot be attributed to a temperature dependent phonon mode, there must be some neutron scattering from Γ_5 tunnelling modes in $NH_4H_2PO_4$. In the deuterated crystal the mode Curie Temperature will rise, but will still be below the structural transition temperature. However, we may still expect to detect scattering from Γ-point modes at temperatures above the antiferro-electric transition. It has been shown[83] that the scattering will contain a contribution from one branch (transverse) whose frequency as $\underline{q} \rightarrow 0$ is unaffected by depolarizing fields in addition to one which has an anomaly due to the electric field set up in the $\underline{a}$-direction. Since this Coulomb interaction causes the undamped frequency to vary with the direction of $\underline{q}$, we may expect the scattering to be strongly anisotropic in $\underline{q}$. Since it is the mode with $\underline{q} \rightarrow 0$ along $\underline{a}^*$ which has its frequency raised by depolarizing fields, the scattering will be reduced in this direction.

The Curie temperature for this mode at $\underline{q} = 0$ in $ND_4D_2PO_4$ has not yet been found, although measurements of $\varepsilon_a(T)$ are in progress (White - private communication). Comparison with the deuteration shifts for KH_2PO_4, KH_2AsO_4, RbH_2PO_4, shows that T_c is unlikely to exceed 50^oK. Since quasi-elastic intensity is proportional to $T/(T - T_c)$, the value from the ferro-electric fluctuations, at 245^oK is only $\lesssim 5\%$ higher than that at 295^oK. It was decided that this gain in intensity would be more than cancelled by absorption in the walls of a crysostat, and all

measurements were made at room temperature.

5.4 Resolution Considerations

a) For $\Delta E = 0$.

Round the Γ-points of $ND_4D_2PO_4$ we expect intensity from Bragg reflected neutrons as well as those scattered by low frequency phonons. To observe quasi-elastic intensity the $\underline{K}$ and ω resolution must be very good so that the Bragg intensity is concentrated over a small region of $\underline{K}$-space, and only acoustic phonons of very small wave vector have energies falling within the instrumental energy resolution. Although quasi-elastic scattering is considerably less localised in $\underline{K}$-space than most phonon scattering, it is only strong within ≈ 0.25 reciprocal lattice units of the Γ-point, and so the Bragg resolution ellipsoid should be confined to 0.1 or 0.15 reciprocal lattice units from Γ. Similarly, phonons with $\underline{q} \geqslant 0.15$ should have energies outside the half width of the energy resolution function. For $\underline{q} = 0.15$ along $\underline{a}^*$ and $\underline{c}^*$ the corresponding energies are 0.45 and 0.5 THz.; which demands an energy resolution of, at most, 0.75 THz. F.W.H.M.

Changes in energy resolution are accompanied by changes in the Bragg resolution function. In general, this has a planar section which is ellipsoidal, with axes which increase in length with $\underline{K}$, and whose shape alters as the resolution is changed. At low resolution the major axis lies along the scattering vector, and it becomes almost perpendicular under high resolution. These changes are illustrated in Figures 1.2. Since quasi-elastic scattering was expected to be observed as intensity extending along $\underline{c}^*$, it was essential to have the

major axis of the resolution ellipse tilted away from $\underline{c}^*$. This could be arranged by making low resolution measurements at Γ-points with large h and small ℓ, ideally with $\ell = 0$; or else with high resolution at Γ-points close to the $\underline{c}^*$-axis.

There is another process which can give intensity extending along $\underline{c}^*$, and this is illustrated in Figure 5.3. Most of the Bragg intensity is concentrated within an ellipse, corresponding to the shaded area, and the scattered vector $\underline{k}'$ is drawn to a point outside this area. However, due to the finite instrumental resolution, neutrons with wave vector $\underline{k}' + \underline{dk}'$, which have been elastically scattered from the sample, may be counted in the detector. Possible values of $\underline{dk}'$ lie within the cone illustrated, and for $\underline{dk}'$ lying along $\underline{k}'$, $|\underline{dk}'|$ can be as much as 0.25 reciprocal lattice units (under the lowest resolution used). Such a $\underline{dk}' + \underline{k}'$ falls well within the shaded area and under these scattering conditions will give intensity which tends to concentrate about a line perpendicular to the major axis of the ellipse. Under low resolution with $\underline{K}$ around (2 0 0) or (6 0 0) this intensity will extend along $\underline{c}^*$ and may be confused with quasi-elastic zone centre scattering. With high resolution, at points close to $\underline{c}^*$, some intensity will extend along $\underline{c}^*$, but it will be confined to within 0.05 reciprocal lattice units of the Γ-point.

A convenient method of estimating the $\underline{K}$-space distribution of Bragg intensity round the Γ-points (h, 0, 0) is to compare their measured intensity with that round the points (0,0,h). The symmetry of the mode causes the structure factors $F(h,0,\ell)$,

for $h = 0$, ℓ even, to be identically zero; and, neglecting phonon contributions, all intensity measured round points $(0\ 0\ \ell)$ must be from Bragg scattering. This immediately gives the shape of the Bragg resolution function for these points. By rotating this function through 90°, and scaling it suitably, the spatial distribution of Bragg intensity at points along $\underline{a}^*$ may be obtained. This distribution will contain the intensity spread of Figure 5.3. The method adopted for this scaling depends on the actual Bragg intensities of the reflection pair $(h\ 0\ 0)$ and $(0\ 0\ h)$. If both are strong, i.e. $>$ 10,000 counts/sec., the quasi-elastic contribution to the $(h\ 0\ 0)$ peak could be considered negligible, and the scaling factor taken as the ratio of the peak heights. Before scaling, the general background was subtracted by comparing the background counting rates midway between the Γ-point and neighbouring M-points. If the Bragg intensities are both below 2,000 counts/sec. the scaling factor must be taken as $|F_{h00}|^2 / |F_{00h}|^2$ where the F's are calculated structure factors. In both cases, all of the Bragg contribution could be subtracted from the distribution round (h, 0,0), and the remaining intensity attributed to quasi-elastic scattering. Ignoring phonon contributions could only overestimate the Bragg contribution, and with an energy resolution better than 0.75 THz. there can be no phonon intensity outside the range $r = 0.1$ reciprocal lattice units round the Γ-point. This method is then sufficient to decide whether or not there is any quasi-elastic intensity around most points like $(h\ 0\ 0)$. For points with Bragg intensity in the intermediate range $((2 \rightarrow 10) \times 10^3$ counts/sec.), some will be affected by extinction. This depresses the peak intensity, as well as

broadening the half width of the Bragg peak, and could lead to errors in estimating Bragg contributions by comparing a reflection affected by extinction with one not affected. Although expressions exist, which give the correction which should be applied to the integrated Bragg intensity to take account of extinction, it is not possible to estimate the half width increases at all accurately.

At Γ -points (h, 0, ℓ), the Bragg intensity had to be estimated by comparison with that at points along $\underline{c}^*$. In ND_2PO_4 (0 0 2) and (0 0 6) are systematic absences, and the (2 0 0) and (6 0 0) Bragg intensities had to be estimated from those for (0 0 4) and (0 0 8).

Quantitative measurements of the quasi-elastic scattering for $\underline{q}$ close to zero would require detailed measurements of phonon cross-sections and line shapes for $\underline{q}$ in the range $0.05 \rightarrow 0.25\ \underline{c}^*$ from the Γ-point, with extrapolation to calculate the actual contribution for phonons with $\underline{q} \rightarrow 0$. The Bragg peaks give typical counting rates of $(10 \rightarrow 100 \times 10^3)$/100 secs., and we know that the M-point quasi-elastic scattering from the same crystal gave typically 50 counts$_\Lambda$ (/100secs). Since the average atomic displacements in the Γ -point and M-point modes should be similar near their respective Curie Temperatures, and our measurements were made considerably closer to the antiferroelectric Curie temperature than to the ferro-electric, 50 counts$_\Lambda$ (/100secs) is an upper estimate of the Γ-point intensity. To measure the Γ -point quasi-elastic scattering at $\underline{q} = 0$ to 10% would require an 0.05% accuracy in the peak Bragg intensity. This precludes measurement of the mode intensities for $\underline{q}$ very close to zero. However, the relative intensities at a given $\underline{q}$,

measured from the Γ -point, should be sufficient to determine the mode eigenvectors. From our measurements, the most suitable point is 0.15 reciprocal lattice units along $\underline{c}^*$, since it is the nearest point to Γ at which there is definitely no phonon scattered intensity.

b) For Energy Analysis

Scans in which the energy transfer to the crystal is varied will be affected by instrumental resolution. Peaks in these scans may be caused by incoherent elastic scattering, coherent elastic scattering, phonons, quasi-elastic scattering and various spurious processes. For neutron energy transfers less than 1 THz., with $\underline{K}$ close to a Γ-point, the latter are limited to spurious intensity from the elastic scattering at that particular Γ -point, which, under neutron energy loss, with $\underline{q}$ positive along $\underline{c}^*$, gives a peak on the positive ω side of zero. (see Figure 5.4) This peak can have a maximum intensity one or two orders of magnitude higher than that of low wave vector acoustic phonons, and the poorer the resolution the closer its centre approaches $\omega = 0$. Thus a typical energy scan at $q = 0.1\underline{c}^*$, with the spectrometer in the configuration with left scattering at the sample and right scattering at the analyser, will be of the form shown in Figure 5.4. The degree of overlap of the individual peaks will increase as the resolution becomes poorer.

To observe any quasi-elastic broadening of the incoherent elastic peak, the resolution must be high enough to exclude acoustic phonon contributions. The incoherent elastic scattering width must be small so that the quasi-elastic broadening (of the incoherent elastic peak) is not negligible.

By using the methods described, to estimate contributions from Bragg and phonon scattering, we have found evidence of quasi-

elastic scattering at five Γ-points. Measurements were made with a range of instrumental resolutions, for several values of $\underline{q}$, and the results are summarised in Table 5.2 and illustrated in Figure 5.5. The most extensive data are for (2 0 0). Under low resolution it was found that the intensity decreased less rapidly on going along $\underline{c}^*$ from (2 0 0) than along $\underline{a}^*$ from (0 0 4). Under improved resolution there remained 17 ± 4 counts/10 monitor counts above background at $0.2\underline{c}^*$ compared with zero at $0.2\underline{a}^*$. To find how much of this intensity was quasi-elastic, it was energy analysed and its half-width compared with that of the energy distribution of the elastic incoherent scattering from vanadium. Under resolutions of 0.55 ± 0.02 THz. and 0.35 ± 0.02 THz. there was no spurious Bragg contribution to the scattering centred at zero energy transfer, and there was either no overlap with focussed or defocussed acoustic phonons, or else it was so small that it was possible to subtract their contribution. For all values of $\underline{q}$, under both resolutions, the energy distribution caused by purely incoherent elastic scattering was computed as

$$N(x) = N_o \exp\left(-\frac{(x - x_o)}{2\sigma^2}\right) \quad \text{with } N_o \text{ the background count}$$

close to the Γ-point, and x_o and σ the parameters obtained from the appropriate vanadium-scan least-squares fit. In all cases, the height and half-width of the actual scattering exceeded those for incoherent elastic scattering. The widths increased with $|\underline{q}|$ and the two values for $|\underline{q}| = 0.2$, obtained under energy resolutions of 0.55 and 0.35 THz. (ΔE_2), are (0.7 ± 0.05)THz. and (0.60 ± 0.03) THz. (ΔE_1) respectively. These give inelasticities $(\Delta E_1^2 - \Delta E_2^2)^{\frac{1}{2}}$ of (0.43 ± 0.07)THz. and (0.48 ± 0.05)THz. At $|\underline{q}| = 0.3$, the width under 0.55 THz.

resolution is (0.83 ± 0.08) THz., which implies an inelasticity of (0.63 ± 0.07) THz.

These intensity measurements in K-space with $\Delta E = 0$ show that there is neutron scattering near Γ-points in $ND_4D_2PO_4$ from processes of so low an energy that it cannot be resolved from the incoherent elastic peak at $\Delta E = 0$. This scattering is elongated along the c^*-direction, and the energy analysis has confirmed that spurious Bragg processes and low energy phonons cannot account for the scattering observed. Some measurements of its inelasticity have been presented.

Our results show that, whereas it is a relatively simple matter to obtain structure factors for the M-point mode, this is not the case for the Γ-point mode. It would be of considerable interest to obtain detailed information on its eigenvectors by measuring structure factors at many different Γ-points. However, our chances of success would be greatly enhanced if we were to use a crystal with a smaller mosaic spread (that used for the KD_2PO_4 measurements of reference (87) was 0.2° compared with our 0.83°). In addition, it would be useful to have squeezed germanium monochromators and analysers of high reflectivity. It might then be possible to obtain intensity data at different temperatures, which could be extrapolated to give an estimate of T_c.

h	k	ℓ	$N_o(\underline{q}' = 0)$	Σ I	$\Sigma I/N_o$
5	0	4	520 ± 60	5000 ± 800	9.6 ± 1.2
2	0	7	450 ± 60	4850 ± 600	11.0 ± 1.4
6	0	5	90 ± 30	870 ± 200	9.6 ± 2.0
7	0	6	70 ± 30	800 ± 200	11.4 ± 2.0
5	0	8	130 ± 30	1380 ± 300	10.6 ± 1.6
8	0	5	40 ± 20	420 ± 200	10.5 ± 1.5
6	0	7	< 40		
9	0	6	< 30		
1	0	10	< 60		

Quasi-elastic Intensities at M-points in $ND_4D_2PO_4$ and Corresponding Integrated Intensities.

TABLE 5.1

h	0	ℓ	$\lvert q \rvert$	ΔE_1 (THz.)	Resolution (Thz.) ΔE_2	No.	$(\Delta E_1^2 - \Delta E_2^2)^{1/2}$
2	0	0.2	0.2	(0.7 ± 0.05)	(0.55 ± 0.02)	200	0.43 ± 0.04
2.1	0	0.2	0.224	(0.68 ± 0.07)	(0.55 ± 0.02)	75	0.40 ± 0.05
1.9	0	0.2	0.224	(0.73 ± 0.07)	(0.55 ± 0.02)	85	0.47 ± 0.05
1.95	0	0.2	0.206	(0.68 ± 0.04)	(0.55 ± 0.02)	175	0.40 ± 0.05
6	0	0.3	0.3	(0.83 ± 0.08)	(0.55 ± 0.02)	120	0.62 ± 0.05
6	0	0.4	0.4		(0.55 ± 0.02)	0	
2	0	0.2	0.2	(0.60 ± 0.04)	(0.35 ± 0.02)	100	0.49 ± 0.04

ΔE_2 is the F.W.H.M. of vanadium elastic incoherent scattering.

ΔE_1 is the F.W.H.M. of (total intensity - scaled incoherent intensity).

N_o is the maximum of (total intensity - scaled incoherent intensity).

Measurements for $ND_4D_2PO_4$ Γ-points

TABLE 5.2.

h k ℓ	Subtraction of Bragg	Intensity along $\underline{c}^*$	Intensity at $0.075\underline{a}^*$ from Γ
8 0 0	Scaled (0 0 8)	30 $\pm$ 5/1000 monitor counts at $0.2\ \underline{c}^*$	0
3 0 3	(3 0 3) Bragg very sharp, allows direct subtraction	20 $\pm$ 5/1000 monitor counts at $0.1\ \underline{c}^*$	0
5 0 3	(0 0 4) in conjunction with (0 0 8) Bragg gave estimate of shape of (5 0 3) Bragg	90 $\pm$ 5/1000 monitor counts at $0.2\ \underline{c}^*$	20 $\pm$ 10/1000 monitor counts

Measurements for $ND_4D_2PO_4$ Γ-Points

TABLE (5.2a)

Figure 5.1 The $\underline{a}^*$ - $\underline{c}^*$ plane in $ND_4\ D_2\ PO_4$ with one Brillouin Zone shown (page 87)

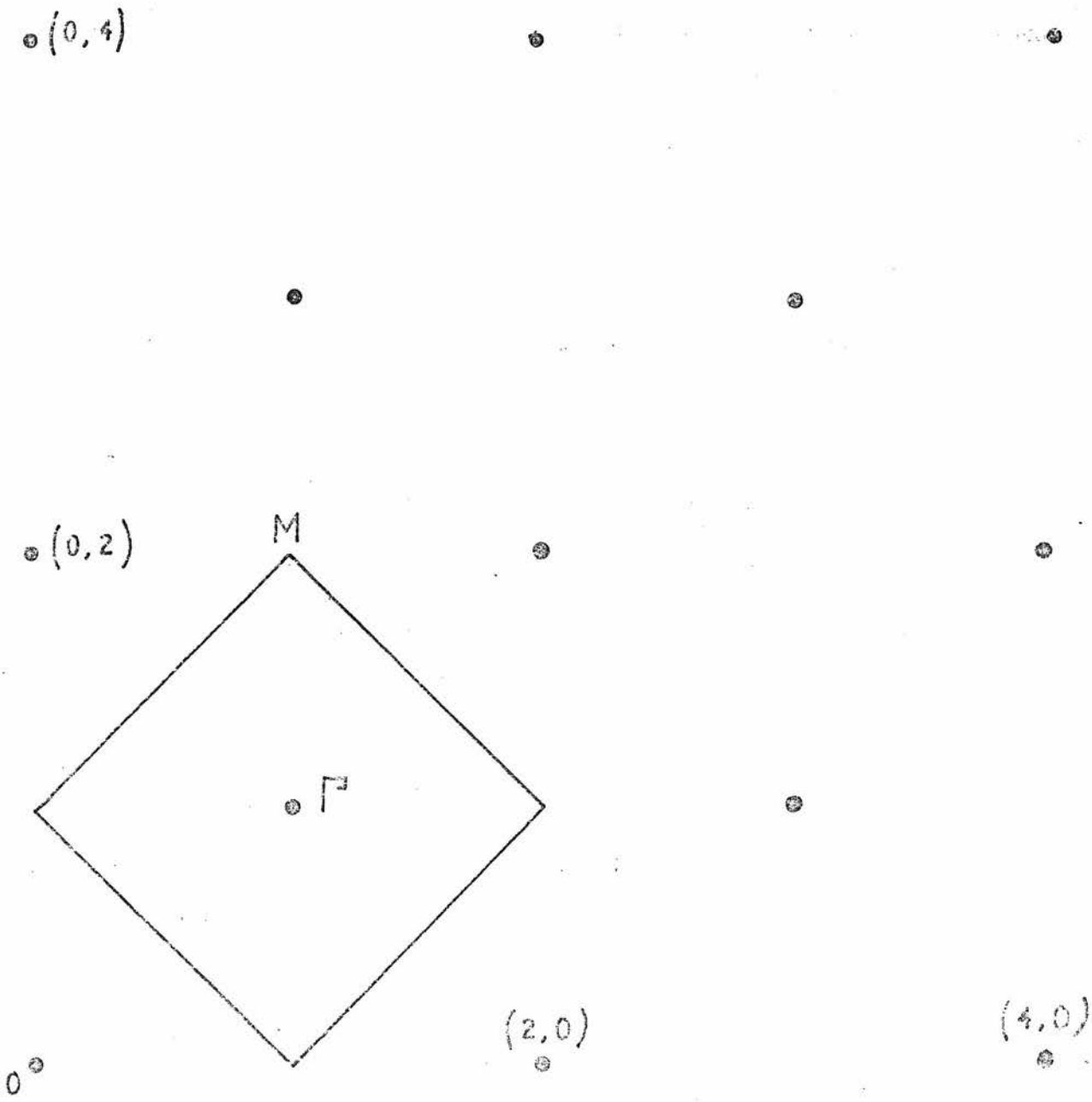

FIGURE
5-1

Figure 5.3 Illustration of a process giving rise to an intensity spread along $\underline{a}^*$ in $ND_4\ D_2\ PO_4$ (page 95)

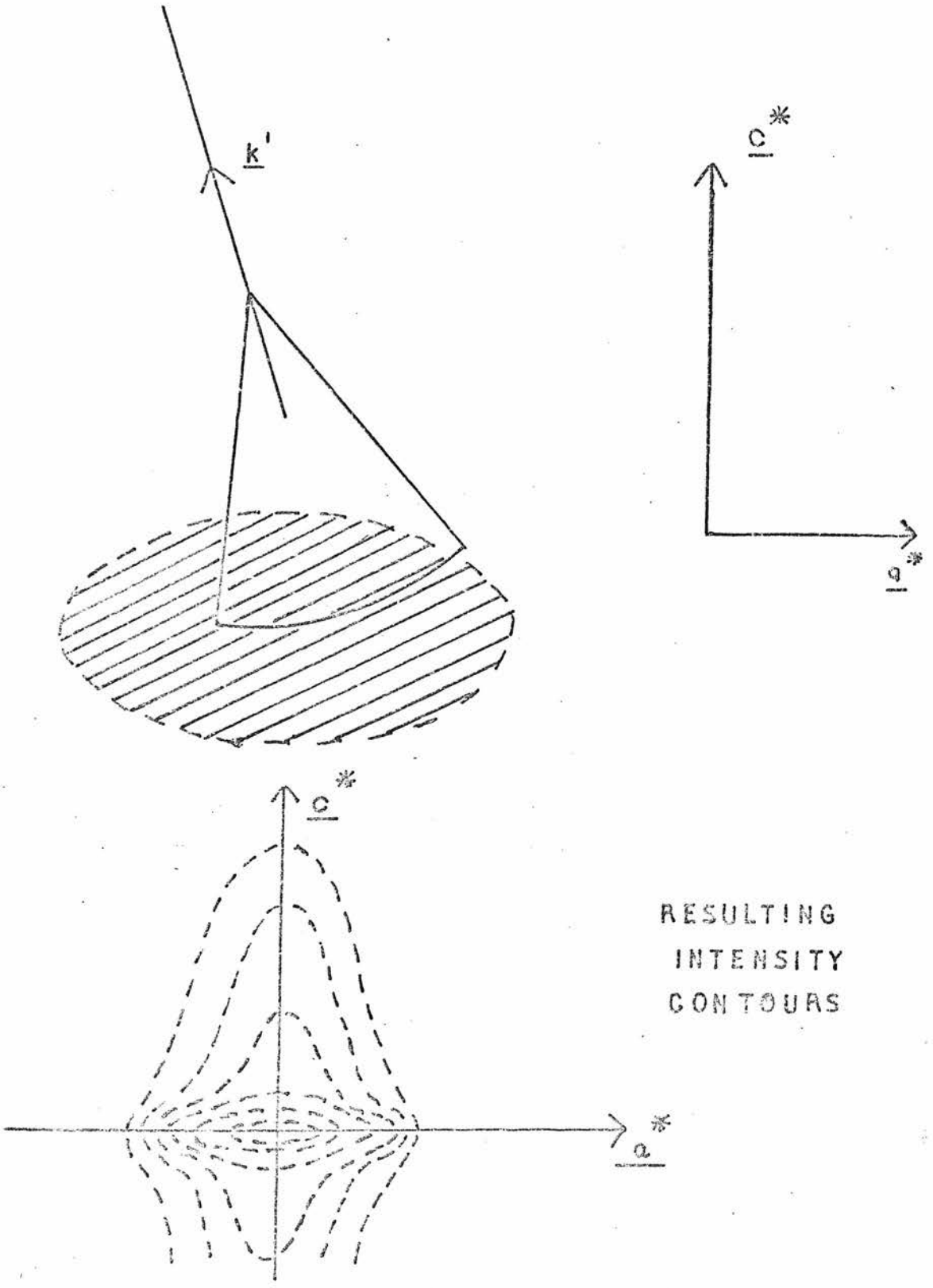

FIGURE 5·3

Figure 5.4 Typical Energy Scan obtained with a Triple Axis Spectrometer (page 98)

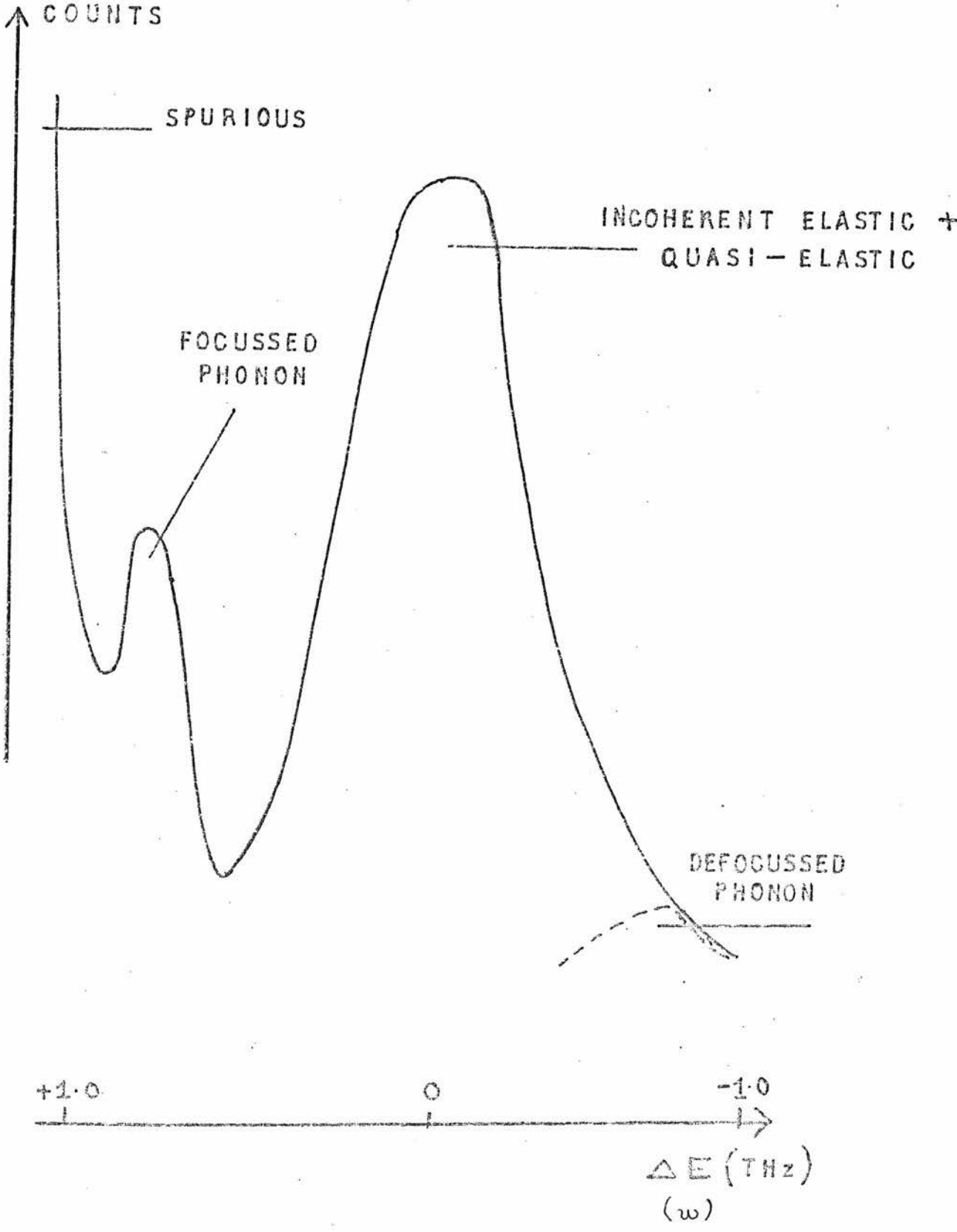
COUNTS
SPURIOUS
INCOHERENT ELASTIC +
QUASI – ELASTIC
FOCUSSED
PHONON
DEFOCUSSED
PHONON
+1·0
0
-1·0
ΔE (THz)
(ω)

FIGURE 5·4

Figure 5.5 Contours in Reciprocal Space and Energy Analysis of Scattered Neutron Intensity around (200) in ND_4 D_2 PO_4 (page 99)

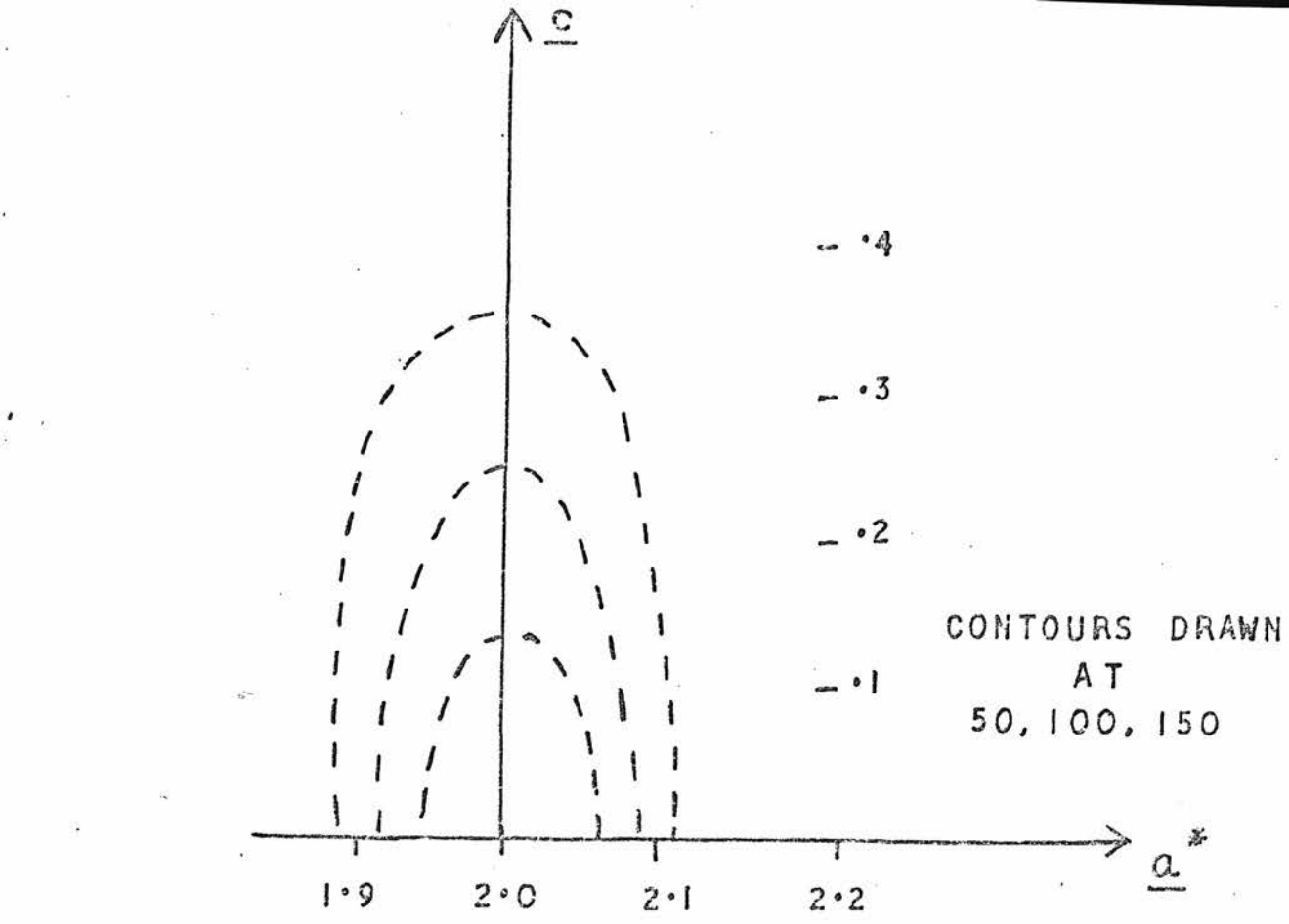

INTENSITY AROUND (200) WITH BRAGG AND INCOHERENT CONTRIBUTIONS SUBTRACTED ($E_0 - E_1 = 0$)

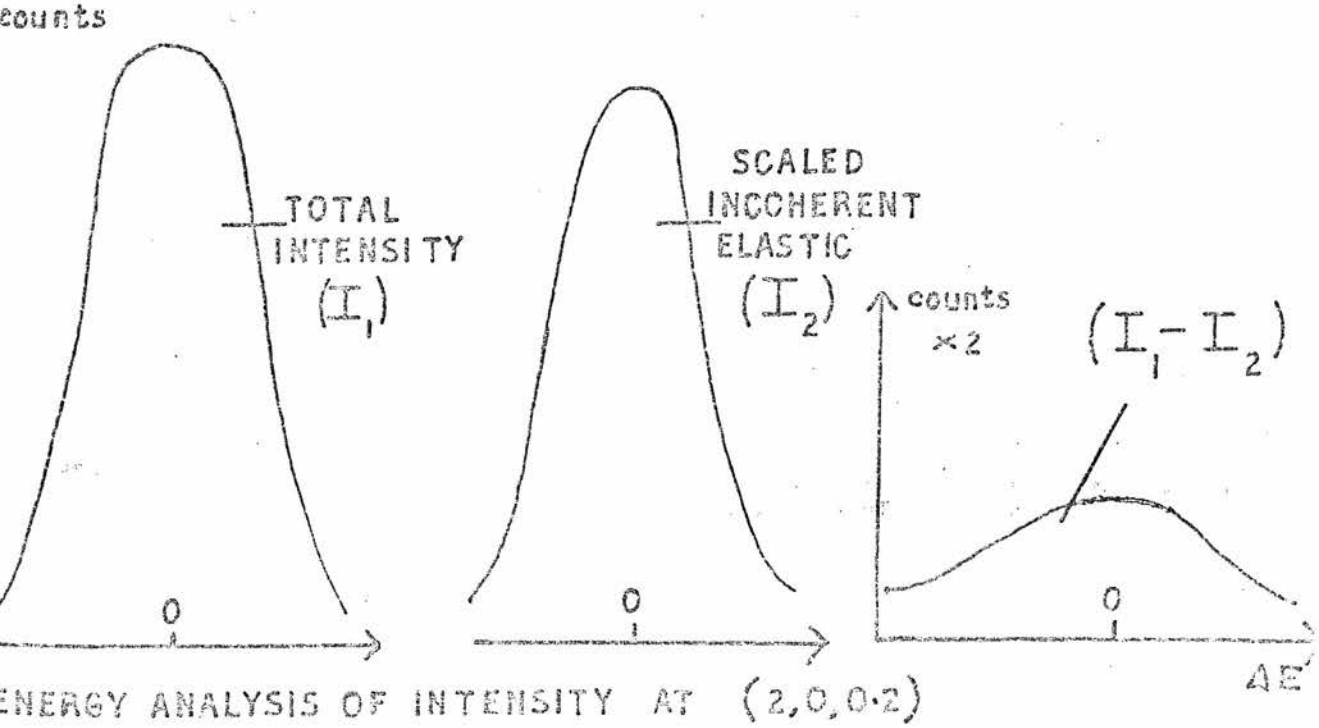

ENERGY ANALYSIS OF INTENSITY AT (2,0,0·2)

FIGURE 5·5

CHAPTER 6

THE EIGENVECTOR DETERMINATION FOR THE ANTIFERROELECTRIC MODE IN $ND_4D_2PO_4$

In this chapter we describe methods which have been used to determine the eigenvectors of anomalous modes of vibrations in crystals which have ferro-electric or anti-ferro-electric phase transitions. We use a least squares procedure to find the eigenvector of the antiferro-electric mode in $ND_4D_2PO_4$. A Fourier synthesis method for determining mode eigenvectors is described and applied to the ferro-electric mode in KD_2PO_4 and the antiferro-electric mode in $ND_4D_2PO_4$.

6.1 Examples of Eigenvector Determination

a) Perovskites

In these materials, the soft mode can often be identified with a particular phonon branch, which has a well defined frequency for $\underline{q} \rightarrow 0$, at temperatures down to within a few degrees of the transition. The mode eigenvector can be obtained through model calculations, since it is one of the normal modes of vibration of the crystal.

This method has been used by Cowley[77] to find the ferro-electric mode eigenvector associated with the cubic to tetragonal phase transition in $SrTiO_3$. There are, in general, 15 branches in the dispersion curves, but crystal symmetry causes degeneracies at particular points of the Brillouin zone. For $\underline{q}$ along $[0\,0\,1]$ the normal modes are either pure transverse or pure longitudinal. Cowley has

measured four T and three L branches at 90°K, and three T and the longitudinal acoustic mode at 296°K. For a particular shell model fit with axially symmetric short-range forces, it was found that quite small changes in the model parameters could account for the large changes which occurred in the frequency, at $\underline{q} = 0$, of the lowest T.O. mode as the temperature ranged from 296°K to 90°K. This was obviously the ferro-electric mode. Its eigenvector, predicted by this model, should give a pattern of atomic displacements similar to that distinguishing the crystal structures above and below the phase transition. The main feature of the eigenvector is a vibration of the Ti atom in antiphase to the other atoms, and the relative displacements are similar to those found in the ferro-electric transition in $Ba\ Ti\ O_3$.

b) The ferro-electric mode in KD_2PO_4.

The mode eigenvector may be determined by fitting mode structure factors. This method may be used when the mode is overdamped as well as when there is an associated well-defined peak in the phonon spectrum. We now consider the ferro-electric mode in KD_2PO_4.

It has been shown (see reference (63), for example) that in a tunnelling model the $m_k^{-1/2}\ \underline{K}.\underline{e}_k(\underline{q}j)$ factor of equation (1.17) should be replaced by $\sin \underline{K}.\underline{u}_k$ for the protons. Here we have written

$$\underline{u}_k = m_k^{-1/2}\ \underline{e}_k(\underline{q}j)$$

so that $\underline{u}_k$ is an actual displacement. The structure factor for the ferro-electric mode in KD_2PO_4 should contain $\sin(\underline{K}.\underline{u}_k)$ for the deuterium contribution; however, for

the $\underline{K}$ values in typical neutron scattering experiments, it is unlikely that the difference between $\underline{K}.\underline{u}_k$ and $\sin(\underline{K}.\underline{u}_k)$ could be detected. We shall therefore replace $\sin(\underline{K}.\underline{u}_k)$ by $\underline{K}.\underline{u}_k$ in our discussions and consider the validity of this in a later section, (Section 6.5). The mode structure factor is,

$$F(\underline{K}) = \sum_k b_k \exp(-W_k(\underline{K}))(\underline{K}.\underline{u}_k)\exp(i\underline{K}.\underline{r}_k) \qquad (6.1)$$

where the summation is over all atoms in the unit cell. The $F(\underline{K})$ for the ferro-electric mode in KD_2PO_4 and the antiferroelectric mode in $ND_4D_2PO_4$ are given explicitly as equations (6.10) and (6.12). By measuring the intensity of the quasi-elastic scattering at many reciprocal lattice points, it may be fitted by the individual atomic displacements, $\underline{u}_k$, using a least squares procedure.

A preliminary fit to these intensities for KD_2PO_4 has been published by Buyers et al.[87], using the displacements obtained by Bacon and Pease[68]. This gave a χ^2 of about 50 for 11 intensity measurements. The results of a full least squares analysis have been given by Skalyo et al.[88]. They fitted 60 intensity measurements with eight parameters with a χ^2 of 2.1. The $\underline{u}_k$ in the ferroelectric mode are a linear combination of the seven basis vectors of the Γ_4 representation, and demanding orthogonality to the Γ_4 acoustic mode reduces the problem to the determination of six independent displacement parameters. Since the deuterium Debye-Waller factors were not considered well enough known in advance, B_{11} and B_{33} for deuterium were obtained as parameters of the refinement. The final displacements are illustrated in Figure (6.1) and their values given in Table

6.1. These are those predicted by Cochran[62] with the addition of a displacement of the deuteriums along $\underline{c}$ in phase with the phosphorous atoms and a distortion of the oxygen tetrahedra. This result shows that the atomic displacements in the ferro-electric mode can only be found by fitting quasi-elastic intensities, not by considering differences in the crystal structure above and below the transition. The observed and calculated intensities are given in Table 6.2.

c) The antiferro-electric mode in $ND_4D_2PO_4$.

We have used the method (b) to find the eigenvector of this mode. Meister et al.[92] have made no attempt to fit their intensity measurements with atomic displacements. They argue "the problem involves determination of 20 amplitude parameters corresponding to a linear combination of the 20 modes $Z_1 + Z_4$." This paper uses a different notation and the $Z_1 + Z_4$ representation does in fact correspond to the M_{34} representation of Chapter 4. These 20 amplitude parameters correspond to a solution of the problem in 3-dimensions. We confine our attention to the (0 1 0) projection, in which the amplitude parameters reduce to ten by using the symmetry restrictions on the displacements of N and P given in Chapter 4, and the ordering scheme for the deuteriums illustrated by Montgomery[83].* These are incorporated in Figure (6.2). The atomic Debye-Waller factors for the heavy atoms may be obtained from the results of Tenzer et al.[94], and those for the ordering deuteriums may be assumed to be the same as for KD_2PO_4. There is no information on the B_{ij}'s for the ammonium group deuteriums.

* See also p 117 and Table (6·3)

We have carried out a least-squares refinement of the 36 available quasi-elastic intensities to fit 11 parameters. These are ten displacement parameters (illustrated in Figure (6.2)) and a Debye-Waller factor for the ammonium deuteriums, which we have assumed is isotropic.

The O-D-O group of atoms at (0.15, 0) have their displacements highly correlated in the [0 1 0] projection, and give one composite term in the structure factor. For these atoms we refined the product of a scattering length and a displacement. Our starting parameters for the heavy atoms were taken from the results of X-Ray diffraction studies[71]. The deuteriums of the ammonium group were initially assumed to follow the nitrogen atom. The other deuteriums were given displacements of the same magnitude as the nitrogen atoms, since there was no evidence, from the intensity data, that the deuterium contribution dominated the scattering. The results for KD_2PO_4 clearly showed that the structure factors were large when the deuterium contributions were in phase.

The data refined after 14 cycles of least-squares to give a χ^2 of 2.9. The final values for the parameters are given in Table 6.3. Table 6.4 gives a list of experimental and calculated intensities. We used a χ^2 defined by

$$\chi^2 = \frac{1}{(n-p)} \sum_i \frac{(I_{obs}(i) - I_{calc}(i))^2}{\sigma(i)^2}$$

where i runs over all n observations, and p is the number of variable parameters. The $\sigma(i)$ are the experimental errors.

The results of Table 6.3 differ from those for KD_2PO_4. The deuterium atoms at $(\frac{1}{4}\ \frac{1}{4})$ and $(-\frac{1}{4}\ \frac{1}{4})$ do not have considerably larger displacements than the other atoms. The

atoms of the ammonium group have relatively large displacements, and these cannot be described by a rigid translation along x with a superimposed rigid rotation of the four deuteriums around the nitrogen. The deuterium framework is greatly distorted; the atoms D_{A1} and D_{A2} do move closely perpendicular to the N-D bond in this projection, but the D_{A3} and D_{A4} displacements are at almost 45° to the bond. The O-D-O composite group has a relatively large displacement along z, but we cannot reach any conclusions on the separate atomic displacements. Our results for the N and P atoms agree with those of Keeling and Pepinsky[71], but we cannot test the distortion of the oxygen tetrahedra which they find.

The elements of the correlation matrix were all around 0.2, except for those between the z-displacement of D_{A3} and the displacements of N and O_1, and between N_x and D_{A1x}. These all have values of approximately 0.5. In the (0 1 0) projection these atoms are separated by less than 0.8 Å. We shall take up this point in Section 6.4(b).

6.2 A Fourier Synthesis Method for Eigenvectors

This method for determining the eigenvector of any crystal mode of vibration has been described by Cochran[95], and we now present the first applications. We illustrate its use by considering the ferro-electric mode in KD_2PO_4. We then apply it to the antiferro-electric mode in $ND_4D_2PO_4$ and use the results in conjunction with our least squares refinement to discuss the validity of our solution of the eigenvector problem.

Following Cochran, we define the quantity

$$D(\underline{r}) = \frac{1}{V} \sum_{\underline{\tau}} G(\underline{\tau}-\underline{q})\exp(-i(\underline{\tau}-\underline{q}).\underline{r}) \quad . \qquad (6.2)$$

The notation is the same as in Chapter 1, and $G(\underline{\tau}-\underline{q})$ and hence $D(\underline{r})$ may be complex quantities. We consider only one phonon branch and drop the suffix j in the structure factor of equation (1.17). $G(\underline{\tau}-\underline{q}) \equiv G(\underline{K})$ may be shown to be the Fourier transform of

$$-\sum_{k} (\underline{u}_k.\text{grad}\, \rho_k(\underline{r}-\underline{r}_k))\exp(i\underline{q}.\underline{r}_k) \quad .$$

Hence

$$D(\underline{r}) = \frac{1}{V} \sum_{\underline{K}} \left(-\sum_{k} \underline{u}_k.\text{grad}\, \rho_k(\underline{r}-\underline{r}_k)\exp\, i\underline{q}.\underline{r}_k\right)_{F.T.} \exp -i(\underline{\tau}-\underline{q}).\underline{r} \qquad (6.3)$$

which, on comparison with

$$\sum_{\ell} \rho(\underline{r}-\underline{r}_\ell) = \frac{1}{V} \sum_{\underline{K}} f(\underline{\tau})\, \exp(-i\underline{\tau}.\underline{r})$$

where $f(\underline{\tau})$ is the Fourier transform of $\rho(\underline{r})$, gives

$$D(\underline{r}) = -\sum_{\ell k} \underline{u}_k\, \text{grad}\, \rho_k(\underline{r}-\underline{r}_{\ell k})\exp\, i\underline{q}.\underline{r}_{\ell k} \quad . \qquad (6.4)$$

Hence, $D(\underline{r})$, expressed as a Fourier series by equation (6.3), is a function of the atomic displacements, $\underline{u}_k$, in the mode considered. The reader should refer to reference (95) for details of this derivation.

To simplify the computation and interpretation of $D(\underline{r})$, we assume that all atoms, k, have the same isotropic Debye-Waller factor, $\exp(-K^2/4p)$. We now introduce

$$D_k(\underline{r}) = -\underline{u}_k.\, \text{grad}\, \rho_k(\underline{r}) \qquad \text{and find}$$

$$\text{grad}\, \rho_k(\underline{r}) = -2p\underline{r}\rho_k(\underline{r})$$

where $\rho_k(\underline{r}) = b_k(p/\pi)^{3/2} \exp(-pr^2)$

and $$D(\underline{r}) = \sum_{\ell k} D_k(\underline{r}-\underline{r}_{\ell k}) \exp(i\underline{g}.\underline{r}_{\ell k}) \qquad (6.5)$$

where $D_k(\underline{r}) = 2p(\underline{r}.\underline{u}_k)\rho_k(\underline{r})$.

$\rho_k(\underline{r}-\underline{r}_{\ell k})$ has appreciable value only when $\underline{r}$ is close to an atomic position, $\underline{r}_{\ell k}$, and so

$$D(\underline{r}) = e^{i\underline{g}.\underline{r}} \sum_{\ell k} D_k(\underline{r}-\underline{r}_{\ell k}) \quad .$$

Hence, using equation (6.2),

$$D'(\underline{r}) = \sum_{\ell k} D_k(\underline{r}-\underline{r}_{\ell k}) = \frac{1}{V} \sum_{\underline{\tau}} G(\underline{\tau}-\underline{g}) \exp -i\,\underline{\tau}.\underline{r} \qquad (6.5')$$

and $D'(\underline{r})$ may be computed by measuring the $|G(\underline{\tau}-\underline{g})|^2$ as the scattered neutron intensity from the particular mode, assigning the correct phase to each term and then summing the Fourier series.

The interpretation of $D'(\underline{r})$ follows from equations (6.5). At $\underline{r} = \underline{r}_{\ell_1 k_1}$, the term in the summation with $\ell = \ell_1$, $k = k_1$ is zero. On moving a small distance $\underline{\delta}$ from $\underline{r}_{\ell_1 k_1}$, $(\underline{r}-\underline{r}_{\ell_1 k_1})$ increases, but ρ_k decreases. $D_k(\underline{r}-\underline{r}_{\ell k})$ will reach a maximum at $\underline{\delta} = \underline{\delta}_{\ell_1 k_1}$, say, and then decrease as $\underline{\delta}$ increases further. Obviously $\rho_k(+\underline{\delta}) = \rho_k(-\underline{\delta})$, and so $D_k(+\underline{\delta}) = -D_k(-\underline{\delta})$; in particular, for $\underline{\delta}$ along a line perpendicular to $\underline{u}_{k_1}$, $D_{k_1}(\underline{\delta}) \equiv 0$. Thus, this term in the

summation gives a positive and negative peak about $\underline{r}_{\ell_1 k_1}$ with a local plane of anti-symmetry perpendicular to $\underline{u}_{k_1}$. The heights of these peaks have equal magnitude, i.e. are proportional to $b_{k_1} |\underline{u}_{k_1}|$, under the assumptions preceding equations (6.5).

The contribution (near $\underline{r}_{\ell_1 k_1}$) of the other terms in the summation over ℓ and k will be small compared with that for $\ell = \ell_1$, $k = k_1$, providing neighbouring atoms are separated by greater than $\dot{\approx}$ 0.85 Å. For this separation, $\exp(-p(r-r_{\ell k})^2)$ has a value of around 0.05, compared with unity for $\underline{r}_{\ell k} = \underline{r}_{\ell_1 k_1}$. This contribution is certainly small compared with fluctuations in $D'(\underline{r})$ caused by errors in the $G(\underline{\tau}-\underline{q})$. This is not the case if the summation, $\sum_{\underline{\tau}}$, is over such a restricted region of reciprocal space that series termination effects are significant. We assume, at present, that the measurements are extensive enough that we may ignore these effects; a method for eliminating series termination effects is discussed in Section 6.3.

In this discussion it has been assumed that the plot of $D'(\underline{r})$ is in a three dimensional space, i.e. both $D'(\underline{r})$ and the $\underline{u}_k$ are real. In general, both are complex and the real parts of the $\underline{u}_k$'s are deduced from the real part of $D'(\underline{r})$, and the imaginary parts from the imaginary part of $D'(\underline{r})$.

Equations (6.5) show that, near $\underline{r}_{\ell k}$

$$D'(\underline{r}) \dot{\approx} D_k(\underline{r}-\underline{r}_{\ell k}) = 2p_k(\underline{r}-\underline{r}_{\ell k}).\underline{u}_k b_k \left(\frac{pk}{\pi}\right)^{3/2} \exp(-p_k(\underline{r}-\underline{r}_{\ell k})^2) . \tag{6.6}$$

For the peak maximum at $\underline{\delta}_k$ from $\underline{r}_{\ell k}$,

$$D_{max}(\underline{r}_{\ell k}) = 2p_k \underline{\delta}_k.\underline{u}_k b_k \left(\frac{pk}{\pi}\right)^{3/2} \exp(-p_k |\underline{\delta}_k|)^2 . \tag{6.7}$$

Under the assumption, $p_k = p$ for all k, this reduces to (const. $\times$ b_k |displ. of atom k|), since $\underline{\delta}_k$ is now δ for all k. In Section 6.4, we shall show that the general expression of equation (6.7) must be used for KD_2PO_4, for which the p_k for deuterium is about one quarter that for the heavy atoms in the

structure. By analogy, the general expression must be used to deduce relative atomic displacements in $ND_4D_2PO_4$.

6.3 Series Termination Effects

$D'(\underline{r})$ is computed as a Fourier series which is, in theory, summed over all reciprocal lattice vectors, $\underline{\tau}$. In practice, the $G(\underline{\tau}-\underline{q})$ are only measured over the region of reciprocal space defined by $|\underline{K}| = S < S_o$. We must consider the errors occurring in $D'(\underline{r})$ when all terms of appreciable magnitude are not included in the summation over $\underline{\tau}$. Since $D'(\underline{r})$ is related to the gradient of $\rho(\underline{r})$, we may consider $\rho_f(\underline{r})$, which is $\rho(\underline{r})$ modified by series termination effects, and take grad $\rho_f(\underline{r})$ as the modified $D'(\underline{r})(D_f(\underline{r}))$. The effect on $\rho(\underline{r})$ has been discussed very fully by Lipson and Cochran[96] and we shall only quote the relevant results.

The function, $\rho_f(\underline{r})$, computed by summing over the limited range of $\underline{K}$, is the sum of two terms. One, peaks at $\underline{r}_{\ell k}$ and falls to zero in a distance of the order of $\frac{2}{S_o}$ Å. The second term, ρ_{f_2}, oscillates as $\frac{J_1(2\pi S_o r)}{2\pi S_o r}$, which has relatively large subsidiary maxima:-

$$J_1(2.262) = 0.5 \quad ; \quad J_1(4.8) = -0.3.$$

The functions $\rho(\underline{r})$, $\rho_f(\underline{r})$ and $D_f(\underline{r})$ are illustrated in Figure (6.3), where we have considered one-dimension for simplicity. $D_f(\underline{r})$ also shows what are termed series termination ripples, but has double the number of subsidiary peaks in a given range of $\underline{r}$. D_{f2} decreases as r increases, but the effect of these series termination "ripples" is to give appreciable contributions to $D'(\underline{r})$ at neighbouring atomic sites. As S_o increases, the range over which D_{f2} is significant, decreases. The effect of using finite S_o is to broaden the individual peaks in $D'(\underline{r})$, and make it almost impossible to estimate the true heights of the peaks, and hence the true magnitudes of the $\underline{u}_k$.

There may also be difficulties in locating the centres of the peaks, and the local planes of anti-symmetry used to obtain the directions of the $\underline{u}_k$.

Obviously some way of eliminating these series termination effects must be found, and the most usual method follows the treatment described by Bragg and West[97]. A converging factor, $\phi(S)$, is introduced, which is included in every Fourier coefficient, and which makes all coefficients with $|\underline{K}| > S_o$ of negligible value compared with those for small $\underline{K}$. One suitable $\phi(S)$ is $\exp(-\alpha S^2)$, where α is a numerical constant, to be chosen according to the particular problem in hand.

To decide on the most suitable value of α, we consider the effect on $D'(\underline{r})$ of including the factor $\phi(S)$. Let $D''(\underline{r})$ be the density calculated by summing the modified structure factors, $G(\underline{K})\phi(S)$. Then

$$D''(\underline{r}) = \int_V D'(\underline{r} + \underline{R})\psi(\underline{R})dV \qquad (6.8)$$

where $\psi(R) \longleftrightarrow \phi(S)$. ($\longleftrightarrow$ denotes Fourier Transformation).

Thus, $\psi(R) = \int e^{-\alpha S^2} e^{2\pi i \underline{R}.\underline{S}} d^3S = (\frac{\pi}{\alpha})^{3/2} \exp(-R^2 (\frac{\pi^2}{\alpha}))$.

For KD_2PO_4, experimental $G(\underline{K})$ exist for $h^2 + \ell^2 \leqslant 148$, and $S_o = 1.63\ A^{-1}$. If $\alpha = 0.6$, the coefficient with $h^2+\ell^2 = 148$ is reduced by a factor 0.2 compared with those with $(h^2 + \ell^2)$ small. However, we see from equation (6.8) that $D''(\underline{r})$ is $D'(\underline{r})$ convoluted with $\psi(R)$, and the peaks of $D''(\underline{r})$ are broadened relative to those of $D'(\underline{r})$. If $\psi(R)$ is sharp, then the effect on the peaks is small. The half-width of $\psi(R)$ is $2 \times (\frac{0.67\alpha}{\pi^2})^{\frac{1}{2}}$, and so as α is increased to reduce series termination ripples $\psi(R)$ becomes broader. This in turn broadens the peaks of $D''(\underline{r})$. If the atomic separation is small, α must be chosen

to reduce the subsidiary peaks of J_1 without broadening the main peaks sufficiently to cause overlap of peaks from neighbouring atoms.

6.4 Applications of the Fourier Synthesis Method

We now apply this method to the KD_2PO_4 and $ND_4D_2PO_4$ soft mode eigenvectors. In both these examples we show that $D'(\underline{r})$ is purely real.

a) $D'(\underline{r})$ for the KD_2PO_4 ferro-electric mode

The quasi-elastic structure factor for $\underline{q} = 0$ is, from equation (6.1),

$$F(\underline{K}) = \sum_k b_k \, e^{-W_k(K)} \, (\underline{\tau} \cdot \underline{u}_k) e^{i\underline{\tau}.\underline{r}_k} \quad . \qquad (6.9)$$

In the (0 1 0) projection, $\underline{u}_k = u_k\underline{i} + w_k \underline{k}$, and the summation is over all atoms in the unit cell. Taking the origin of the unit cell at $(0\ 0\ -\frac{1}{8})$ we consider the symmetry of the displacements. An atom at $\underline{r}_k$ is displaced to $\underline{r}_k + \underline{u}_k$ in the ferro-electric mode, and that at $-\underline{r}_k$ goes to $-\underline{r}_k + \underline{u}_k$. The atoms at $-\underline{r}_k + (\frac{1}{2}\ \frac{1}{2}\ \frac{1}{2})$ and $\underline{r}_k - (\frac{1}{2}\ \frac{1}{2}\ \frac{1}{2})$ have the same displacement, $\underline{u}_k$. The unit cell contains two molecular units and equation (6.9) becomes

$$F(\underline{K}) = \sum_k b_k \, e^{-W_k(\underline{K})} \quad \underline{K}.\underline{u}_k \quad (e^{i\underline{K}.\underline{r}_k} + e^{i\underline{K}.\underline{r}_k})$$

where the summation is over all atoms in the asymmetric unit. This is ringed in Figure (6.1). In the (0 1 0) projection, the expression for $F(\underline{K})$, incorporating its symmetry (mirror line parallel to z, and centre of symmetry), reduces to

$$\underline{F}(\underline{K}) = b_P P_z \ell \cos 2\pi\ell z_P - b_K K_z \ell \cos 2\pi\ell z_K$$
$$+ b_O O_z \ell (2 \cos 2\pi h(x_{O1}) + 2 \cos 2\pi h(x_{O2}) \cos 2\pi\ell z_{O2})$$
$$- b_D D_{1x} h \sin 2\pi h(x_{D1}) \sin 2\pi\ell(z_{D1})$$
$$+ b_D D_{1z} (\cos 2\pi h(z_{D2}) + \cos 2\pi h(x_{D1}) \cos 2\pi\ell(z_{D1})) \quad . \tag{6.10}$$

We now calculate $D(\underline{r})$, using equations (6.10) and (6.5), but dropping the prime on $D(\underline{r})$, since it is no longer necessary. Writing $F(\underline{K})$ as $F(h,\ell)$ and using equation (6.10) we have

$$F(+h, +\ell) = -F(-h, -\ell) = -F(h, -\ell) = F(-h, \ell) \quad .$$

These relations give

$$D(\underline{r}) = \sum_{h\ell} \mu F(h, \ell) \cos 2\pi hx \sin 2\pi \ell z \quad . \tag{6.11}$$

The summation is over values of h and ℓ in the first quadrant, and μ, the multiplicity, is $1/2$ for $h = 0$ and 1 otherwise. $D(\underline{r})$ is entirely real for this mode, and it follows that the $\underline{u}_k$ are entirely real and in phase.

$D(\underline{r})$ is computed using equation (6.11). The $|F(h,\ell)|$ are the square-rooted intensities, given in reference (88), and the signs of the F's are those of the calculated structure factors (obtained by substituting the $\underline{u}_k$ of Table 6.1 ineq. (6.1)).

The results of this calculation are shown in Fig. (6.4). Each term in the Fourier expansion contained a factor $\exp(-0.01(h^2+\ell^2))$, to reduce series termination ripples. With this overall temperature factor included, the individual peaks in $D(\underline{r})$ are still well separated. Throughout these calculations

a circular cut-off was used for the Fourier summation, i.e. all terms with $(h^2 + \ell^2) \leqslant 148$ were included. If an intensity, for a $\underline{K}$ in this range, had not been measured, then the calculated $F(\underline{K})$ was substituted. This required the inclusion of eight calculated values out of a total of sixty terms. The calculated structure factors must be on the same scale as the observed values. We followed Skalyo et al. in choosing a scaling factor which gave the deuterium atoms a displacement similar to the x displacement which the hydrogens experience at the transition in KH_2PO_4. This scaling factor does not result in giving

$$\sum |F_{obs}| = \sum |F_{calc}| \quad \text{or} \quad \sum I_{obs} = \sum I_{calc}$$

and we shall discuss this in Section 6.6(a).

We have calculated the relative values of the $\underline{u}_k$, assuming that the peak heights (in $D(\underline{r})$) are proportional to $b_k |\underline{u}_k|$. The results are listed in column 2 of Table (6.5). Column three of this table lists the ratio $b_k |u'_{-k}|/N_k$. N_k is the peak height, calculated as the average of the magnitudes of the positive and negative peaks, around $\underline{r} = \underline{r}_{\ell k}$, and the $\underline{u}'_k$ are the displacements of Table 6.1. If the assumption of $p_k = p =$ constant, for all atoms, is valid, then these ratios should be constant. The results of Table 6.5 show that this assumption is invalid. The full expression for the peak heights in $D(\underline{r})$ (equation (6.7)) should be used, with the δ_k deduced from the plot in Figure(6.4). The combined effect of the different Debye-Waller factors and series termination errors makes this method a rather unsatisfactory way of deducing accurate $\underline{u}_k$'s.

We have found that the $\underline{u}_k$ may be found with high

accuracy, by comparing two different density functions. The $D(\underline{r})$, computed by including experimental values for the $|F|$'s, we call $D_{\underline{r}}(F_{obs})$. The corresponding function, with calculated F's replacing experimental values, we call $D_{\underline{r}}(F_{calc})$. Since both density functions are calculated by including the same number of Fourier coefficients, with the same cut-off, the series termination errors should be the same in both cases. The corresponding peaks will be modified by the Debye-Waller factors, in the same manner provided the Debye-Waller factors used in the calculations are close to the true values. This will be the situation, if an approximate fit to the intensity data is taken as the starting point for the calculations of the $D(\underline{r})$. Convergence occurs when $(D_{\underline{r}}(F_{obs}) - D_{\underline{r}}(F_{calc})) = \varepsilon(\underline{r})$ tends to zero, for all $\underline{r}$. The $\underline{u}_k$ used to calculate $D_{\underline{r}}(F_{calc})$ are then the correct relative displacements.

The final $\varepsilon(\underline{r})$ for KD_2PO_4 is illustrated in Figure (6.5). The calculations leading to this map of $\varepsilon(\underline{r})$ have used slightly different values of B_{11} and B_{33} from those of Table (6.1), since these parameters were adjusted to give better agreement between $D_{\underline{r}}(F_{obs})$ and $D_{\underline{r}}(F_{calc})$ around the deuterium positions. The final values for B_{11} and B_{33} are 3.2 $\mathring{A}^2$ and 2.47 $\mathring{A}^2$. These agree with the values in Table (6.1), within the quoted errors. These maps of $D(\underline{r})$ and $\varepsilon(\underline{r})$ will prove useful when judging our fit to the $ND_4D_2PO_4$ intensity data. We discuss their main features in Section 6.6.

b) $D(\underline{r})$ for the $ND_4D_2PO_4$ anti-ferroelectric mode

We now compute $D(\underline{r})$ for $ND_4D_2PO_4$. The atomic displacements have been illustrated in Figure (6.2). The structure retains a centre of symmetry in the (0 1 0) projection,

an atom at $\underline{r}_k$ has displacement $\underline{u}_k$

" " " $-\underline{r}_k$ " " $-\underline{u}_k$.

Once again, we need only sum over the atoms in the asymmetric unit which is ringed in Figure (6.2), and find

$$F(\underline{K}) = \sum_k b_k e^{-W_k(\underline{K})} (\underline{K}.\underline{u}_k) \left[\exp(i\underline{K}.\underline{r}_k) - \exp(-i\underline{K}.\underline{r}_k) \right] .$$

For an atom in a general position, this reduces to

$$2b_k e^{-W_k(\underline{K})} hu_k \cos 2\pi h x_k \sin 2\pi \ell z_k$$

$$+ \; 2b_k e^{-W_k(\underline{K})} \ell w_k \sin 2\pi h x_k \cos 2\pi \ell z_k$$

where $\underline{u}_k = u_k \underline{a}^* + w_k \underline{c}^*$.

The coefficients of $K.a^*$ in $F(\underline{K})$ are, with appropriate $e^{-W_k(\underline{K})}$,

$$b_N N_x h \sin 2\pi \ell x_N + b_P P_x h \sin 2\pi x_P$$

$$+ \; b_D h D_{1x} \cos 2\pi h x_{D1} \sin 2\pi \ell z_{D1}$$

$$+ \; 2b_D h D_{A1x} \cos 2\pi h x_{DA1} \sin 2\pi \ell z_{DA1}$$

$$+ \; 2b_D h D_{A3x} \cos 2\pi h x_{DA3} \sin 2\pi \ell z_{DA3}$$

$$+ \; 2b_O h O_{1x} \cos 2\pi h x_{O1} \sin 2\pi \ell z_{O1} .$$

The coefficients of $\underline{K}.\underline{c}^*$ in $F(\underline{K})$ are

$$b_D \ell D_{1z} \sin 2\pi h x_{D1} \cos 2\pi \ell z_{D1}$$

$$+ \quad 2b_O \ell O_{1z} \sin 2\pi h x_{O1} \cos 2\pi \ell z_{O1}$$

$$+ \quad 2b_D \ell D_{A1z} \sin 2\pi h x_{DA1} \cos 2\pi \ell z_{DA1}$$

$$+ \quad 2b_D \ell D_{A3z} \sin 2\pi h x_{DA3} \cos 2\pi \ell z_{DA3}$$

$$+ \quad 2b_O \ell O_{2z} \sin 2\pi h x_{O2} + b_D \ell D_{2z} \sin 2\pi h x_{D2} \quad . \qquad (6.12)$$

Since $x_{O2} \simeq x_{D2}$, the last two terms give one composite term, written $\ell U \sin 2\pi h x_{O2}$. For this mode, $F(h,\ell)$ is an odd function of both h and ℓ, so that

$$D(\underline{r}) = \sum_{+h+\ell} F(h,\ell) \sin 2\pi hx \sin 2\pi \ell z \quad . \qquad (6.13)$$

$D(\underline{r})$ is again purely real, and has the periodicity of the lattice, with the asymmetric unit that of Figure (6.2). The rest of the cell is built up by reflecting $D(\underline{r})$ in lines of anti-symmetry along $\underline{a}$ and $\underline{c}$, which meet at $(0, 0, -\frac{1}{8})$ - the origin chosen for Figure (6.2). This is in contrast to Figure (6.4), where there is a line of anti-symmetry along $\underline{a}$ and one of symmetry along $\underline{c}$. Hence, atoms situated on a line of anti-symmetry may only have a displacement perpendicular to this line. Atoms on a line of symmetry have displacements along this line. This is illustrated for the O-D-O atoms at (0.15, 0) in both KD_2PO_4 and $ND_4D_2PO_4$, the N and P atoms in $ND_4D_2PO_4$, and the K and P atoms in KD_2PO_4. Atoms off lines of symmetry or anti-symmetry may have components of displacement along both a and c .

The experimental intensity data of Table (6.4) are complete for all values of (h, ℓ) in the range

$(h^2 + \ell^2) \leqslant 97$. We have computed $D_{\underline{r}}(F_{obs})$ with this cut-off for the Fourier summation and the signs from F_{calc}'s using the parameters of Table(6.3). The best converging factor was found to be $\exp(-0.15\ (h^2 + \ell^2))$. The resulting plot is given in Figure (6.6). In contrast to the plot for KD_2PO_4, this $D_{\underline{r}}(F_{obs})$ contains only experimental structure factors.

The atoms O-D-O at (0.15, 0) give one positive and one negative peak. In this projection, they are completely superimposed. The contributions from N, D_{A3}, D_{A1} and O_1 are not completely resolved. These are the atomic displacements which gave high correlations in the least-squares refinement. Increasing the range of the experimental measurements would improve the resolution, and decrease the correlations, but it is unlikely that it would ever be possible to resolve the N and D_{A3} peaks. We have not attempted to deduce the $\underline{u}_k$ from the peak heights of Figure (6.6).

We have computed $D_{\underline{r}}(F_{calc})$ and $\varepsilon(\underline{r})$ for this mode. When the scaling factor used in the least squares refinement of I(obs) was used to calculate $D_{\underline{r}}(F_{calc})$, the peaks in $D_{\underline{r}}(F_{calc})$ were consistently less than the corresponding peaks in $D_{\underline{r}}(F_{obs})$. The calculated structure factors had to be multiplied by a factor 1.1 to give the best agreement between the two density functions. $\varepsilon(\underline{r})$ is illustrated in Figure (6.7).

6.5 The Approximation Used to Calculate $F(\underline{K})$

In KD_2PO_4, the deuterium atoms at $(\frac{1}{4}, \frac{1}{4})$ and $(-\frac{1}{4}, \frac{1}{4})$ have relatively large displacements in the ferro-electric mode. $D_k(\underline{r})$ is related to the difference in the structure with the

atoms in their equilibrium positions, and that with the atoms displaced in the mode. That is, $D_k(\underline{r} - \underline{r}_k)$ is $\rho_k(\underline{r} - (\underline{r}_k + \underline{u}_k)) - \rho_k(\underline{r} - \underline{r}_k)$, and this may be replaced, for small $\underline{u}_k$, by $-\underline{u}_k.\text{grad}\,\rho_k(\underline{r} - \underline{r}_k)$. This is valid, provided $|\underline{u}_k| \ll$ width of ρ_k. For the deuteriums, we should use the full expression for $D_k(\underline{r} - \underline{r}_k)$. In practice, the best test of the validity of the approximation is to compute $D_{\underline{r}}(F_{calc})$ with the calculated structure factors incorporating the factor $\sin(\underline{K}.\underline{u}_k)$ for the deuteriums, and compare it with $D_{\underline{r}}(F_{obs})$. If this gives better agreement than the $D_{\underline{r}}(F_{calc})$, for which the factor $(\underline{K}.\underline{u}_k)$ was used, then the approximation is invalid.

We have found that, in practice, we cannot separate the effect of replacing $\sin(\underline{K}.\underline{u}_k)$ by $(\underline{K}.\underline{u}_k)$ from the effect of altering the Debye-Waller factors. With the values of B_{11} and B_{33} from Table 6.1 the deuterium peaks around $(\frac{1}{4}, \frac{1}{4})$ had a maximum value 53.5 in $D_{\underline{r}}(F_{calc})$, compared with 51.5 for $D_{\underline{r}}(F_{obs})$. On using the $\sin(\underline{K}.\underline{u}_k)$ factor, the peak in $D_{\underline{r}}(F_{calc})$ fell to 53.3. However, altering the values of B_{11} and B_{33} to 3.2 $\text{A}^{\circ 2}$ and 2.47 $\text{A}^{\circ 2}$ gave a value of 51.5 for the peak in $D_{\underline{r}}(F_{calc})$, exactly the value for $D_{\underline{r}}(F_{obs})$.

6.6 Discussion

We have presented the results of a least square analysis of quasi-elastic intensities for $ND_4D_2PO_4$, and calculated the corresponding density functions, $D_{\underline{r}}(F_{obs})$ and $D_{\underline{r}}(F_{calc})$. The results of Fourier synthesis for KD_2PO_4 have also been obtained. However, it is well known that least squares fits to crystal structures giving R-factors below 20% may

correspond to an incorrect structure, and Fourier synthesis is a notoriously unreliable method of structure determination. These points are discussed by Donohue in relation to the structure of DNA[98], [99].

In DNA, the elastic structure factors have phases which can take on any value between 0 and 2π, whereas the mode structure factors, which we have calculated, can only have phases 0 or π. The phases are of overwhelming importance in obtaining a Fourier map. Donohue illustrates this by considering three possible synthetic structures for DNA, and obtains the corresponding electron density maps. In all cases, the density corresponded, at low resolution, to the structure used to determine the phases. By citing examples of incorrect structures with "good" Fouriers, Donohue decides that low resolution cannot be blamed for these discrepancies.

Donohue suggests that the density function should be inspected for

(i) irregularly shaped contours, corresponding to resolved atoms;

(ii) unequal peak heights for resolved equal atoms;

(iii) false detail.

These tests may be applied to the plots in Figures (6.4) and (6.6), with (ii) replaced by unequal positive and negative peaks about $\underline{r}_k$. The difference of the observed and calculated density functions cannot be relied on to decide the correctness of a particular structure, since the F_{obs} include experimental errors. Donohue concludes that the final test is a comparison of observed and calculated structure factors, looking for any serious and systematic discrepancies. We now examine our results in the light of these arguments.

a) $\underline{KD_2PO_4}$.

The theoretical resolution is $\approx$ 0.36Å and all atoms, except the O-D-O group, are resolved. With the overall temperature factor included in the calculation, $D_{\underline{r}}(F_{calc})$ had equal peak heights, and a background which was almost flat. This indicates that all series termination ripples have been eliminated and cannot give rise to fluctuations in $\varepsilon(\underline{r})$. The contours of $D_{\underline{r}}(F_{obs})$ were regularly shaped. The magnitudes of the positive and negative peaks for the K P and O atoms are given in Table 6.6. These show discrepancies of up to 10°/o. In $\varepsilon(\underline{r})$ the contours are drawn at $\pm$ 5, to be compared with a maximum peak height of 50 in $D_{\underline{r}}(F_{obs})$ for the deuteriums, and an average of 20 for the other four atoms. $\varepsilon(\underline{r})$ shows definite features around the oxygen positions at (0.083, 0.25) and around (0.35, 0.04). This suggests that the oxygen displacements are suspect. We have altered these $\underline{u}_k$, in an attempt to obtain a featureless $\varepsilon(\underline{r})$, but without success. We can only attribute these discrepancies to experimental error.

We now consider further the choice of a scale factor relating observed and calculated structure factors for this mode. Our calculations so far have used the scale factor chosen by Skalyo et al., for which $\sum F_{obs} = 195$ and $\sum F_{calc} = 162.5$. Table 6.7 lists the average of the magnitudes of the positive and negative peaks around the $\underline{r}_{\ell k}$, in $D(F_{obs})$ and $D(F_{calc})$, for which Skalyo's scale factor was used. Under $D(F_{calc})_{\Sigma}$ we have listed the corresponding peak heights, when the scale factor is chosen to make $\sum F_{obs} = \sum F_{calc}$. The peak heights under $D(F_{calc})$ are mostly in good agreement with those of $D(F_{obs})$, whereas those

in $D(F_{calc})_{\Sigma}$ are consistently higher except for the atom O (0.083, 0.25). The difference function,

$\varepsilon(\underline{r}) = D(F_{obs}) - D(F_{calc})$ is of course zero around the atomic peak positions except for the oxygen position at (0.083, 0.25) and shows fluctuations in other regions (where $|D(F_{obs})| > |D(F_{calc})|$). The function $\varepsilon(\underline{r})_{\Sigma} = D(F_{obs}) - D(F_{calc})_{\Sigma}$ would have peaks around the $\underline{r}_{\ell k}$ and the other fluctuations would be slightly decreased in magnitude, since the increased scale factor would increase $D_{\underline{r}}(F_{calc})_{\Sigma}$ relative to $D_{\underline{r}}(F_{obs})$ at all points, $\underline{r}$. $\varepsilon(\underline{r})$ corresponds to a better fit than $\varepsilon(\underline{r})_{\Sigma}$ if we use the criterion that the difference function should be zero around the majority of the atomic positions.

The fit to observed intensities, presented in Table 6.2, corresponds to a conventional R-value of about 30%. The experimental errors are large, but there are discrepancies for points where h is even and ℓ is 4 or 8. The K and P contributions to the structure factor cancel for these values of h and ℓ. We have tried to vary the $\underline{u}_k$, in turn, around the values given in Table 6.1, but do not obtain any significantly better agreement between these observed and calculated structure factors. Since the fit obtained by Skalyo et al. is generally accepted as correct, we can only cite experimental error once again as the cause of these disagreements.

b) $\underline{ND_4D_2PO_4}$.

The theoretical resolution is $\doteqdot$ 0.46Å. Since so many peaks are unresolved, we cannot discuss the shape of the contours for individual atoms, and cannot compare positive and negative

peaks around the $\underline{r}_k$. Our investigation of the Fourier synthesis must be based entirely on $\varepsilon(\underline{r})$. The average peak heights of Figure (6.6) are around 40, i.e. they are almost double those of $D_{\underline{r}}(F_{obs})$ for KD_2PO_4. The plot of $\varepsilon(\underline{r})$ for $ND_4D_2PO_4$ has contours drawn at $\pm$ 5 and $\pm$ 10, and it is the $\pm$ 10 contours which should be considered in a comparison with $\varepsilon(\underline{r})$ for KD_2PO_4 (Figure (6.5)). $\varepsilon(\underline{r})$ for $ND_4D_2PO_4$ has some definite features around the ND_4 group. However, we have been unable to reduce these by varying the $\underline{u}_k$ by small amounts. Unless the values for the $\underline{u}_k$, given in Table 6.3, correspond to a false minimum in the least squares refinement, we must attribute the fluctuations in the $\varepsilon(\underline{r})$ of Figure (6.7) to experimental error. These fluctuations are certainly no more serious than those for the KD_2PO_4 Fourier map, when one takes into account the difference in the scale of the quasi-elastic intensities. (Comparing Tables 6.2 and 6.4, we see that the high intensities for KD_2PO_4 are around 70, compared with values around 250 for $ND_4D_2PO_4$. These correspond to F's of 8 and 16, with errors of 0.3 and 1.0 respectively.)

Finally we compare the observed and calculated intensities for $ND_4D_2PO_4$ (Tables 6.4). The intensities for (2 0 3), (1 0 4), (2 0 5), (5 0 2), (7 0 4), (1 0 8) show discrepancies, but these do not appear to be systematic.

The Fourier synthesis procedure presents a convenient method for deducing mode eigenvectors. When individual atomic peaks are unresolved, conclusions must be based on the difference function, $\varepsilon(\underline{r})$. Using this method, in conjunction with a least squares analysis of quasi-elastic intensities, we have obtained a solution to the $\underline{u}_k$ for the antiferroelectric mode in $ND_4D_2PO_4$. In spite of some discrepancies, the $\underline{u}_k$ provide a reasonable fit to the limited experimental data available to us.

B_{11}	3.4	±	$0.2\text{A}^{\circ 2}$
B_{33}	2.3	±	$0.3\text{A}^{\circ 2}$
* K_Z	+0.0066	±	0.0005
P_Z	+0.0055	±	0.0006
O_{1Z}	+0.0008	±	0.0005
O_{2Z}	+0.0008	±	0.0006
D_{1x}	-0.025	±	0.001
D_{1Z}	+0.011	±	0.001

* *The displacements are fractional co-ordinates.*

Final Parameters From Least Squares Analysis of KD_2PO_4 Intensity Data

TABLE 6.1

(h k ℓ)	I_{obs} (g = 0)	$\|F_{calc}\|^2$
2 0 0	< 1	0
4 0 0	< 1	0
6 0 0	< 1	0
8 0 0	< 1	0
10 0 0	< 2	0
12 0 0	< 2	0
1 0 1	< 3	1
3 0 1	20 ± 2	24
5 0 1	41 ± 2	43
7 0 1	65 ± 4	63
9 0 1	28 ± 3	29
11 0 1	13 ± 9	16
0 0 2	< 1	0
2 0 2	2 ± 1	1
4 0 2	5 ± 2	6
6 0 2	8 ± 4	7
8 0 2	< 2	1
10 0 2	7 ± 6	0
12 0 2	3 ± 6	0
1 0 3	< 2	4
3 0 3	84 ± 3	80
5 0 3	35 ± 3	33
7 0 3	32 ± 3	36
9 0 3	9 ± 4	5
11 0 3	15 ± 6	17
2 0 4	5 ± 5	18
4 0 4	15 ± 3	0
6 0 4	9 ± 4	0
8 0 4	5 ± 3	0
10 0 4	4 ± 6	5
1 0 5	5 ± 5	3
3 0 5	5 ± 5	3
5 0 5	47 ± 10	44
7 0 5	44 ± 6	30
9 0 5	68 ± 8	61
11 0 5	< 6	2

(h k ℓ)	I_{obs} ($\underline{q}$ = 0)	$\lvert F_{calc} \rvert^2$
0 0 6	< 2	0
2 0 6	4 ± 2	2
8 0 6	4 ± 6	3
10 0 6	15 ± 12	2
1 0 7	49 ± 10	42
3 0 7	17 ± 4	18
5 0 7	75 ± 9	61
7 0 7	7 ± 6	0
9 0 7	16 ± 9	6
2 0 8	10 ± 10	19
4 0 8	< 9	0
6 0 8	28 ± 6	1
8 0 8	13 ± 6	0
1 0 9	9 ± 9	20
3 0 9	< 9	2
5 0 9	< 9	2
7 0 9	62 ± 9	57
2 0 10	10 ± 6	1
4 0 10	9 ± 6	15
6 0 10	21 ± 6	29
1 0 11	9	1
3 0 11	50 ± 6	59
1 1 0	< 1	0
3 3 0	< 1	0
5 5 0	< 1	0

Observed and Calculated Intensities
for KD_2PO_4 Ferroelectric Mode

TABLE 6.2

* N_x	-0.050 ± 0.003	
O_{1x}	$+0.005 \pm 0.005$	
O_{1z}	-0.013 ± 0.005	
$(O\text{-}D\text{-}O)_{displ.} \times b_{O\text{-}D\text{-}O}$	$+0.042 \pm 0.005$	
P_x	-0.005 ± 0.005	
D_{1x}	-0.020 ± 0.005	
D_{1z}	0	
D_{A1x}	-0.082 ± 0.005	
D_{A1z}	$+0.058 \pm 0.009$	
D_{A3z}	$+0.051 \pm 0.005$	
B	4.4 ± 0.5	$\text{A}^{\circ 2}$

$D_{A3x} = 2N_x - D_{A1x} = -0.019 \pm 0.007$

(to retain N as centre of mass of ND_4)

* *Displacements again expressed in fractional co-ordinates.*

Final Parameters from Least Squares Analysis of $ND_4D_2PO_4$ Intensity Data

TABLE 6.3

TABLE 6.4

Observed and Calculated Quasi-elastic Intensities for $ND_4D_2PO_4$.

h	o	ℓ	I_{obs}	$\lvert F_{calc} \rvert^2$
1	0	2	185 ± 25	148
2	0	1	40 ± 20	24
2	0	3	60 ± 20	16
3	0	2	110 ± 20	96
1	0	4	120 ± 20	71
4	0	1	110 ± 20	121
3	0	4	50 ± 20	24
4	0	3	60 ± 20	52
2	0	5	40 ± 20	79
5	0	2	50 ± 20	5
1	0	6	60 ± 20	38
6	0	1	< 40	39
4	0	5	< 40	22
5	0	4	270 ± 30	324
3	0	6	< 20	10
6	0	3	< 20	0
2	0	7	230 ± 30	230
7	0	2	165 ± 25	101
5	0	6	175 ± 25	222
4	0	7	90 ± 20	113
7	0	4	60 ± 20	2
1	0	8	< 100	0
8	0	1	270 ± 30	212
3	0	8	50 ± 20	88
8	0	3	70 ± 20	55
2	0	9	110 ± 20	85
9	0	2	220 ± 30	236
4	0	9	70 ± 20	42
9	0	4	120 ± 20	83
5	0	8	70 ± 20	93
7	0	6	35 ± 20	17
6	0	5	50 ± 20	77
8	0	5	20 ± 20	2
9	0	6	< 15	11
6	0	7	< 20	9
1	0	10	< 30	19

Atom	$D(F_{obs})$	$\lvert \underline{u}''_k \rvert$	$b_k \lvert \underline{u}'_k \rvert \sqrt{D(F_{obs})}$
K	14.6	0.0040	1.67×10^{-4}
P	21.0	0.0041	1.34×10^{-4}
D($\frac{1}{4}$, $\frac{1}{4}$)	52.5	0.0084	3.2×10^{-4}
O-D-O(0.15, 0)	27.4	0.0044	2.5×10^{-4}
O(0.083, 0.25)	10.0	0.0017	0.7×10^{-4}

The $\underline{u}''_k$ are on an arbitrary scale and are deduced from $D(F_{obs})$.

TABLE 6.5.

Atom	$D_+(F_{obs})$	$D_-(F_{obs})$
K	+ 13.8	- 14.2
P	+ 18.9	- 17.9
O (0.083, 0.25)	+ 8.9	- 8.6

Positive and Negative Peak Heights in $D_r(F_{obs})$ for KD_2PO_4.

TABLE 6.6.

Atom	$D(F_{obs})$	$D(F_{calc})$	$D(F_{calc})_{\Sigma}$
O-D-O	27.4	27.0	33.7
K	14.6	14.0	16.8
P	21.0	18.4	21.7
O	8.6	3.0	2.7
D	52.5	52.0	64.1

Averaged Peak Heights for KD_2PO_4 in Different $D(\underline{r})$.

TABLE 6.7.

Figure 6.1 Atomic Displacements for the ferroelectric mode of KD_2PO_4 (page 103)

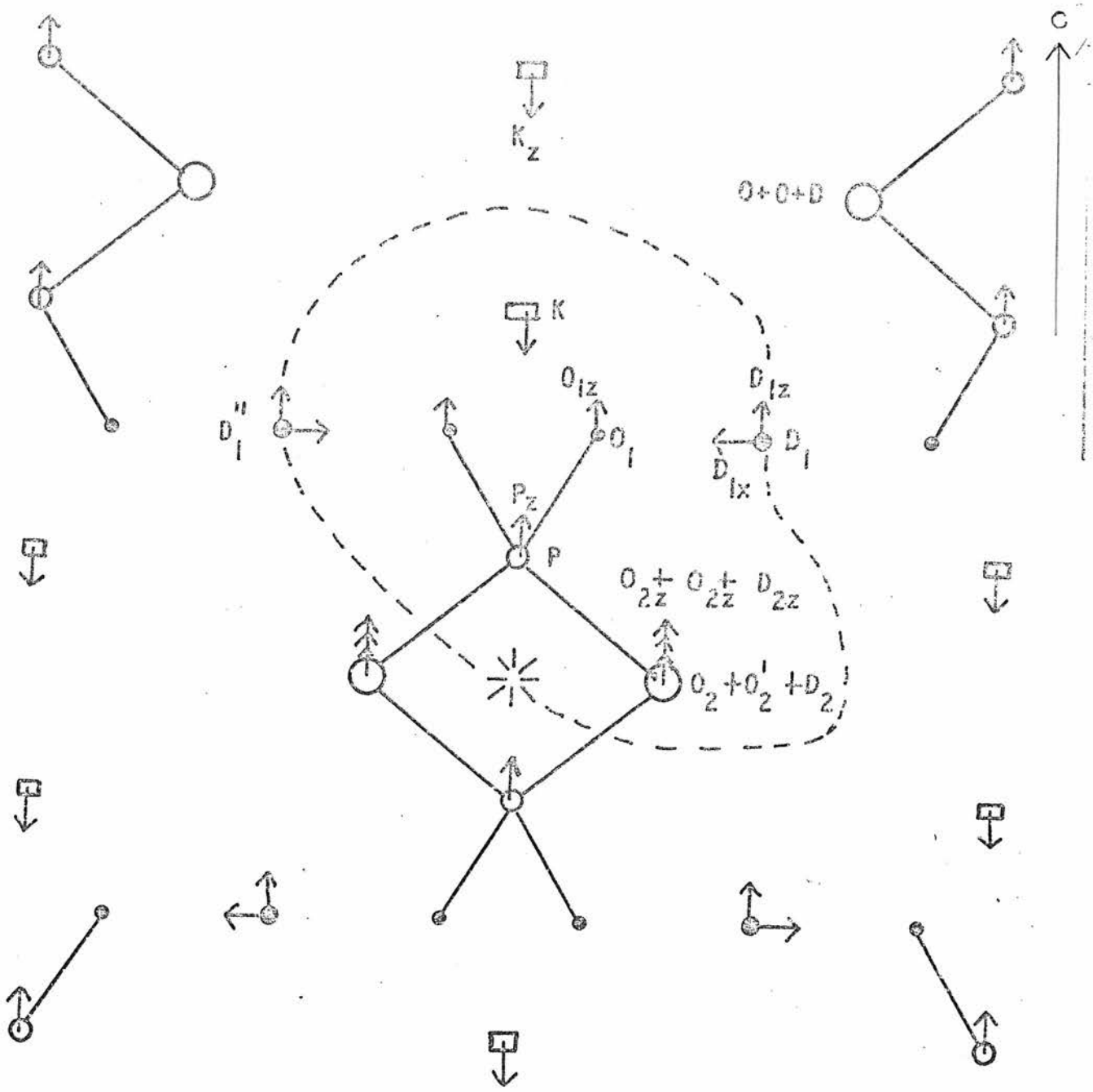

for this mode $D_{1z} = D_{2z}$

and we take $\frac{1}{2} D_1 + \frac{1}{2} D_1''$

FIGURE 6·1

Figure 6.2 Amplitude parameters for the antiferroelectric mode of $ND_4\ D_2\ PO_4$ (page 104)

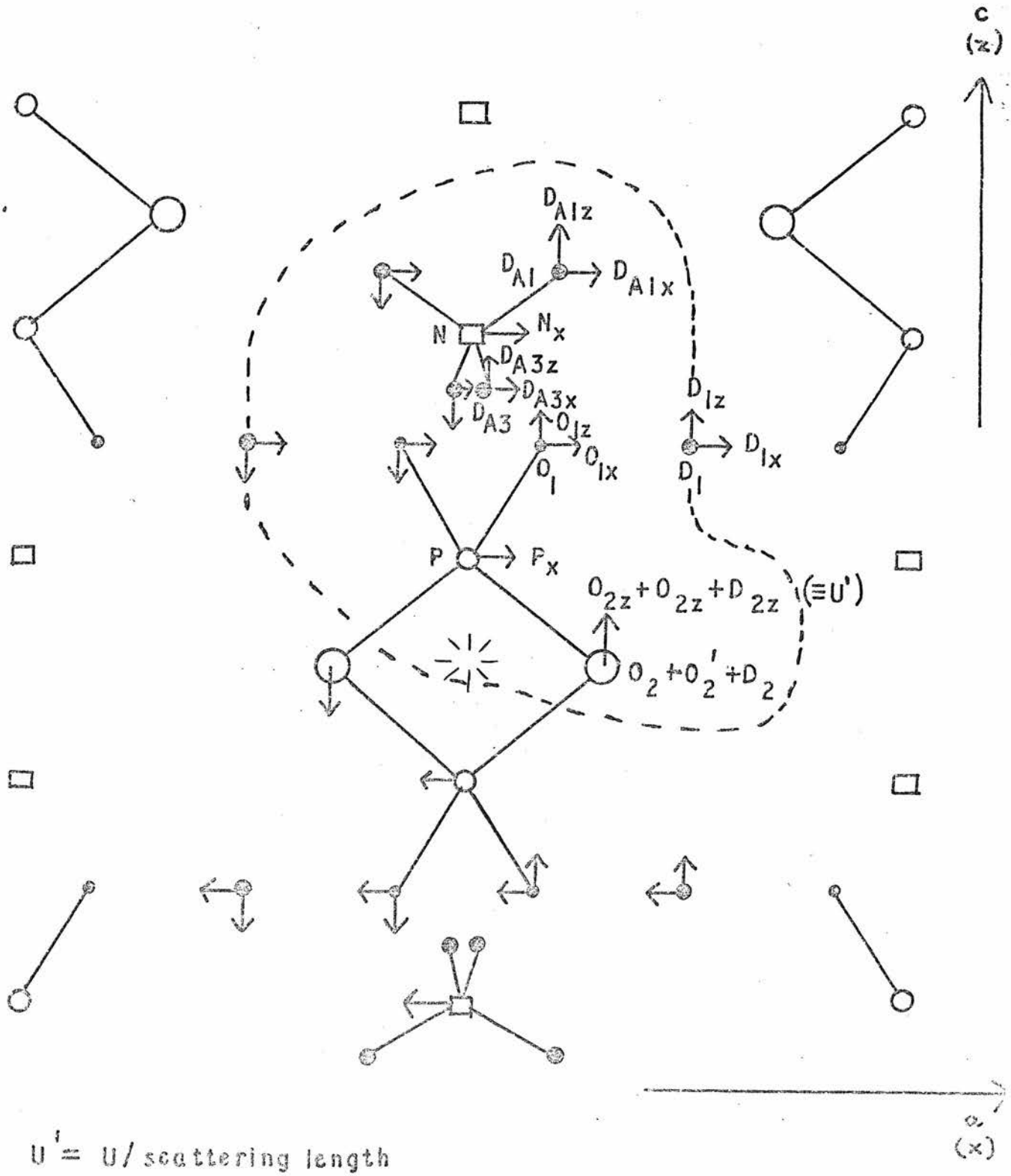

U' = U/scattering length

FIGURE 6·2

Figure 6.3 The functions $\rho(\underline{r})$, $\rho_f(\underline{r})$, $\mathcal{D}'(\underline{r})$ and $\mathcal{D}_f(\underline{r})$ (page 110)

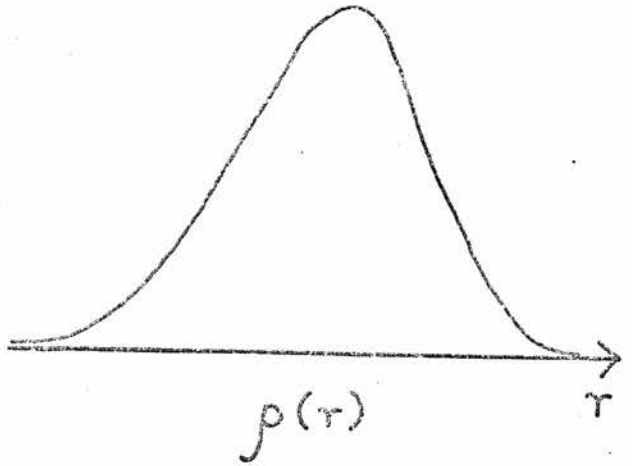

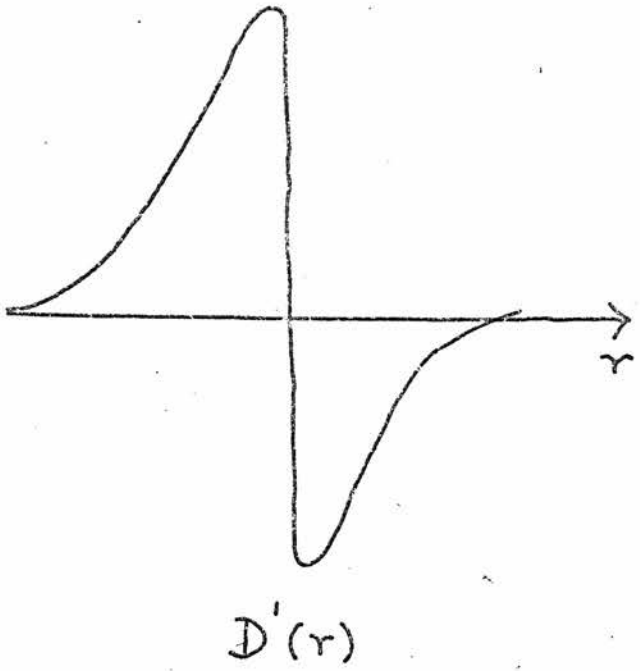

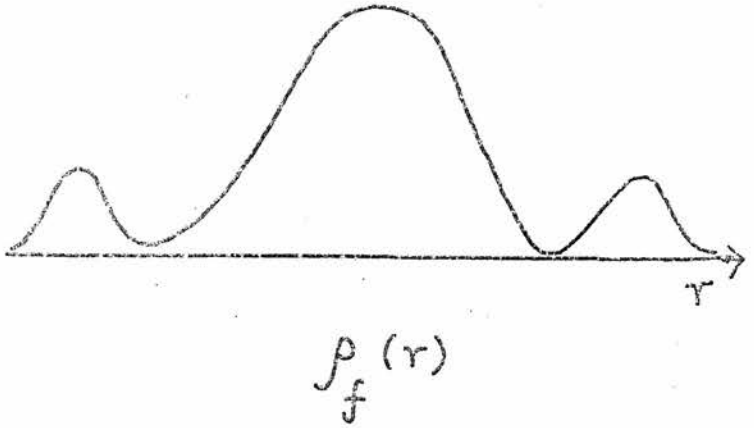

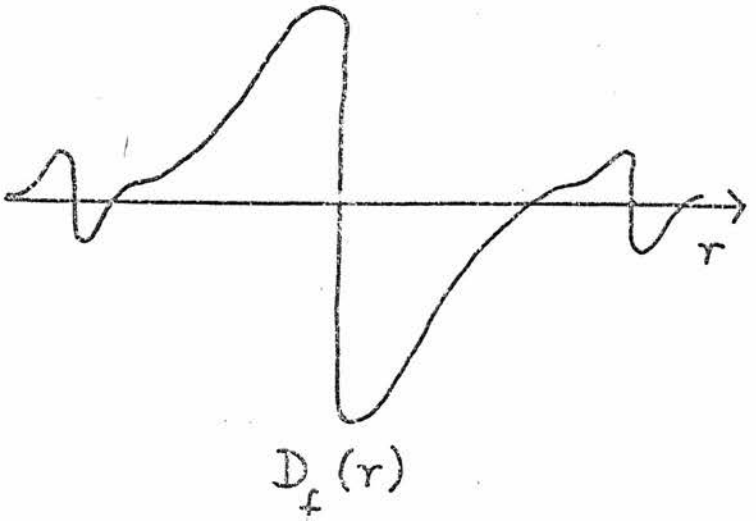

FIGURE 6.3

Figure 6.4 Map of $\mathcal{D}(\underline{r})$ for the ferroelectric mode of KD_2PO_4 (page 113)

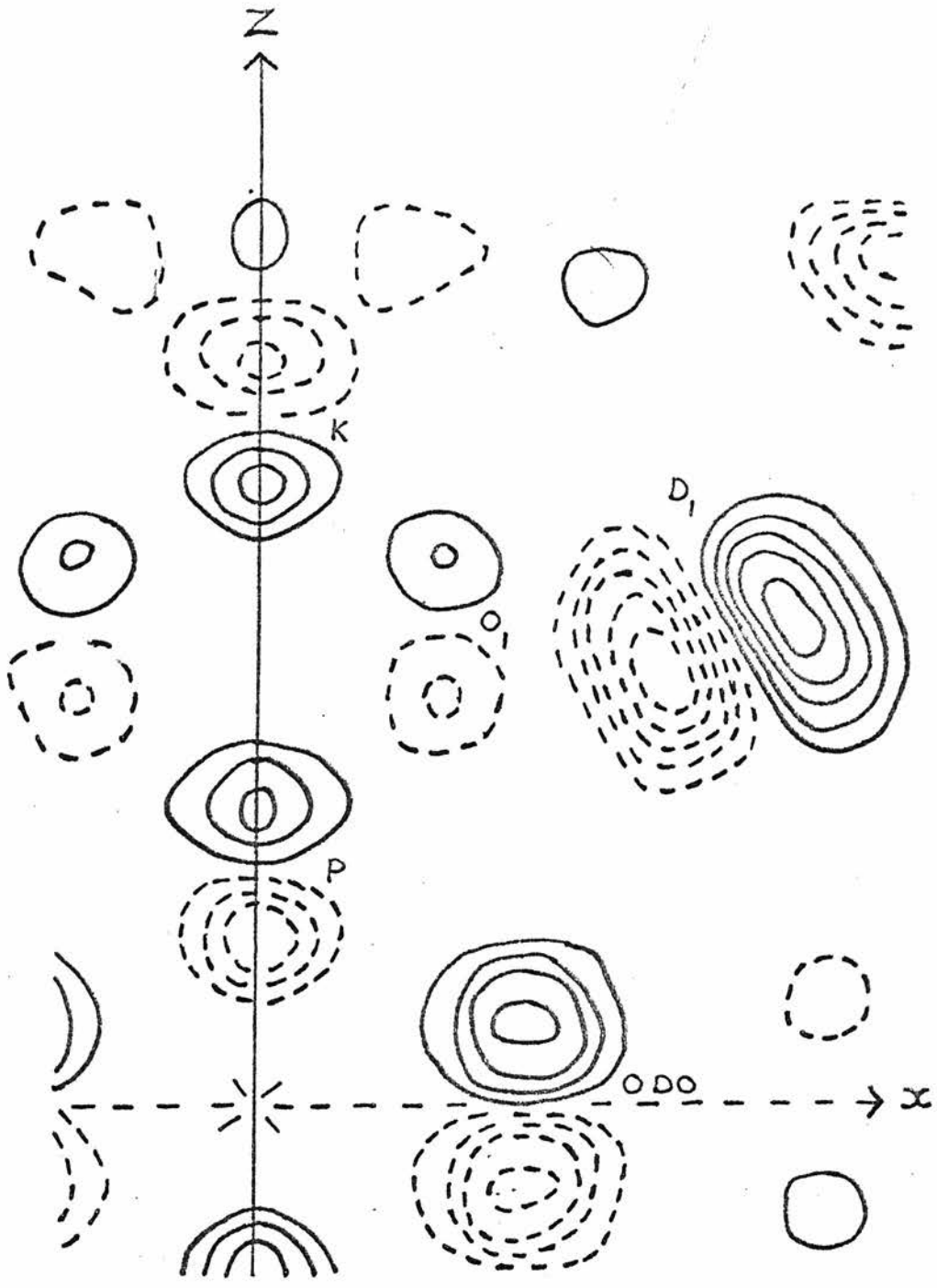

Correction to Figure 6.4

The deuterium peaks (D_1) in this figure have been interchanged between the left and right quadrants. They appear correctly in the figure above from which the other quadrants may be generated by suitable reflection (see page 1

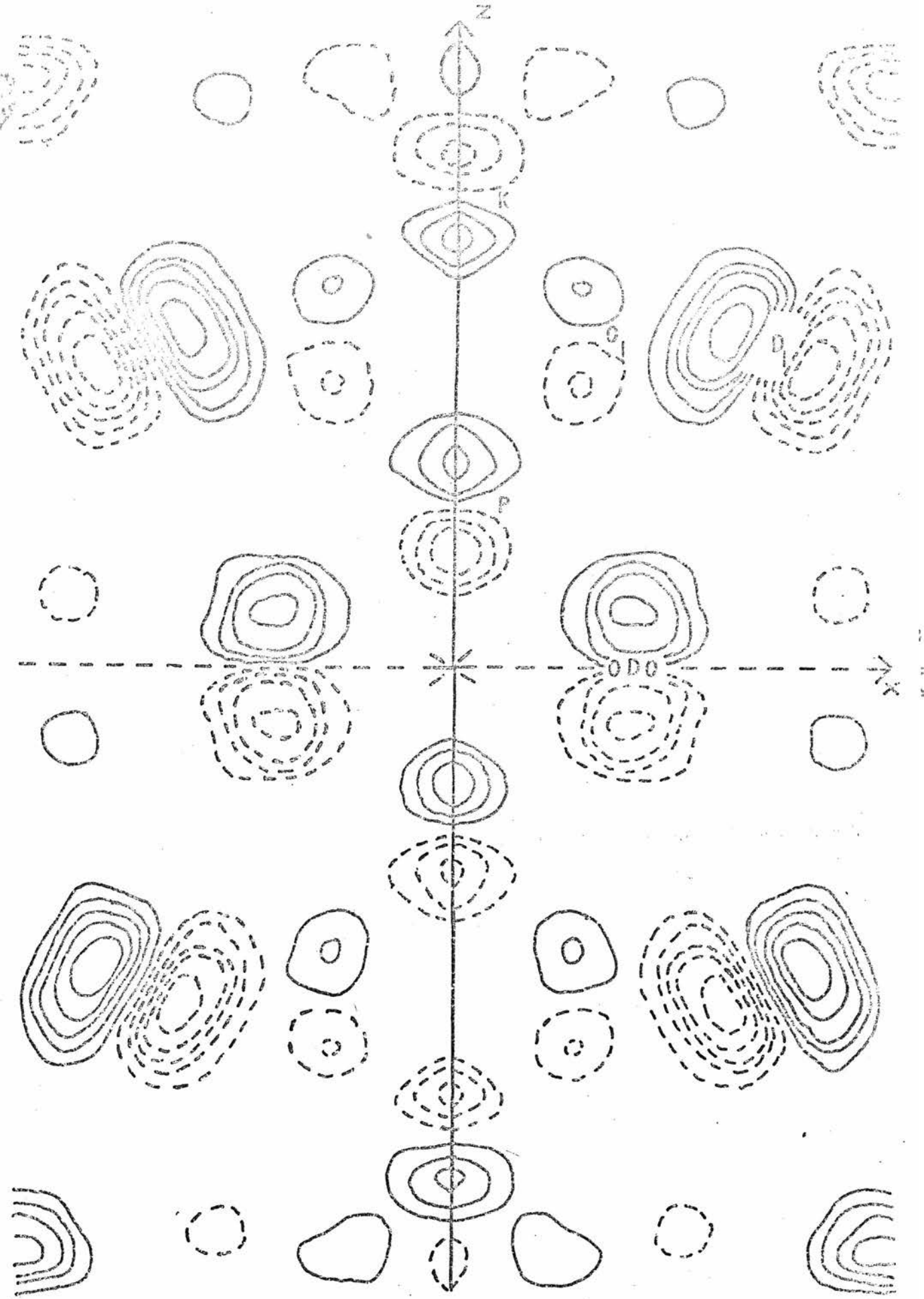
z
K
O
D
P
O D O
x
negative intensi
positive "
contours at ±5 ±10 ±15
±25 ±40

FIGURE 6·4

Figure 6.5 Map of final $\varepsilon(\underline{r})$ for the ferroelectric mode of KD_2PO_4 (page 115)

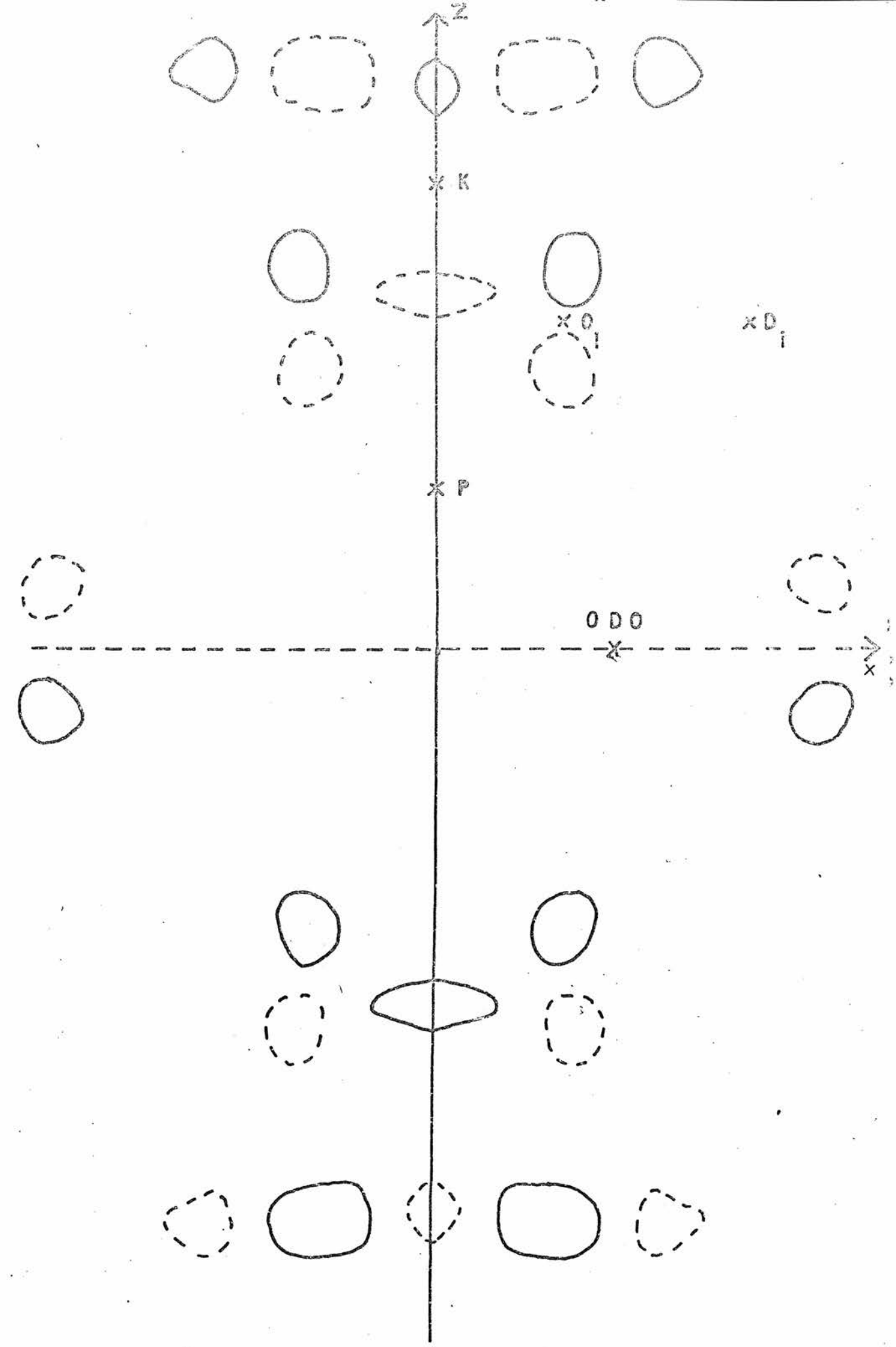

FIGURE 6·5

Figure 6.6 Map of $\mathcal{D}(\underline{r})$ for the antiferroelectric mode of $ND_4\ D_2\ PO_4$ (page 118)

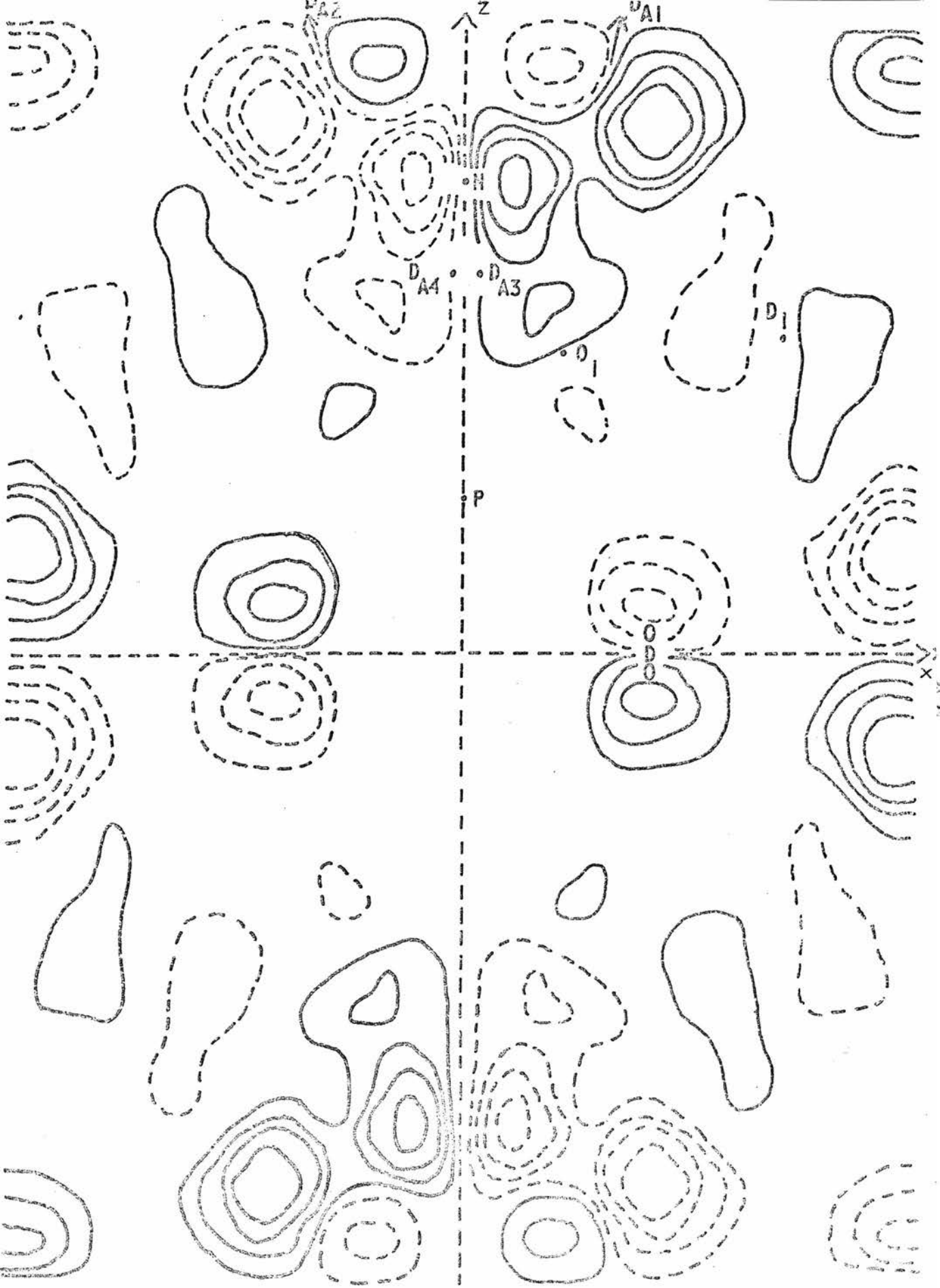
Z
D_{A2}
D_{A1}
N
D_{A4}
D_{A3}
D_1
D_1
P
O
D
O
X
contours drawn at ±10, ±20, ±30, ±4
negative
positive

FIGURE 6·5

Figure 6.7 Map of $\mathcal{E}(\underline{r})$ for the antiferroelectric mode of $ND_4\ D_2\ PO_4$ (page 118)

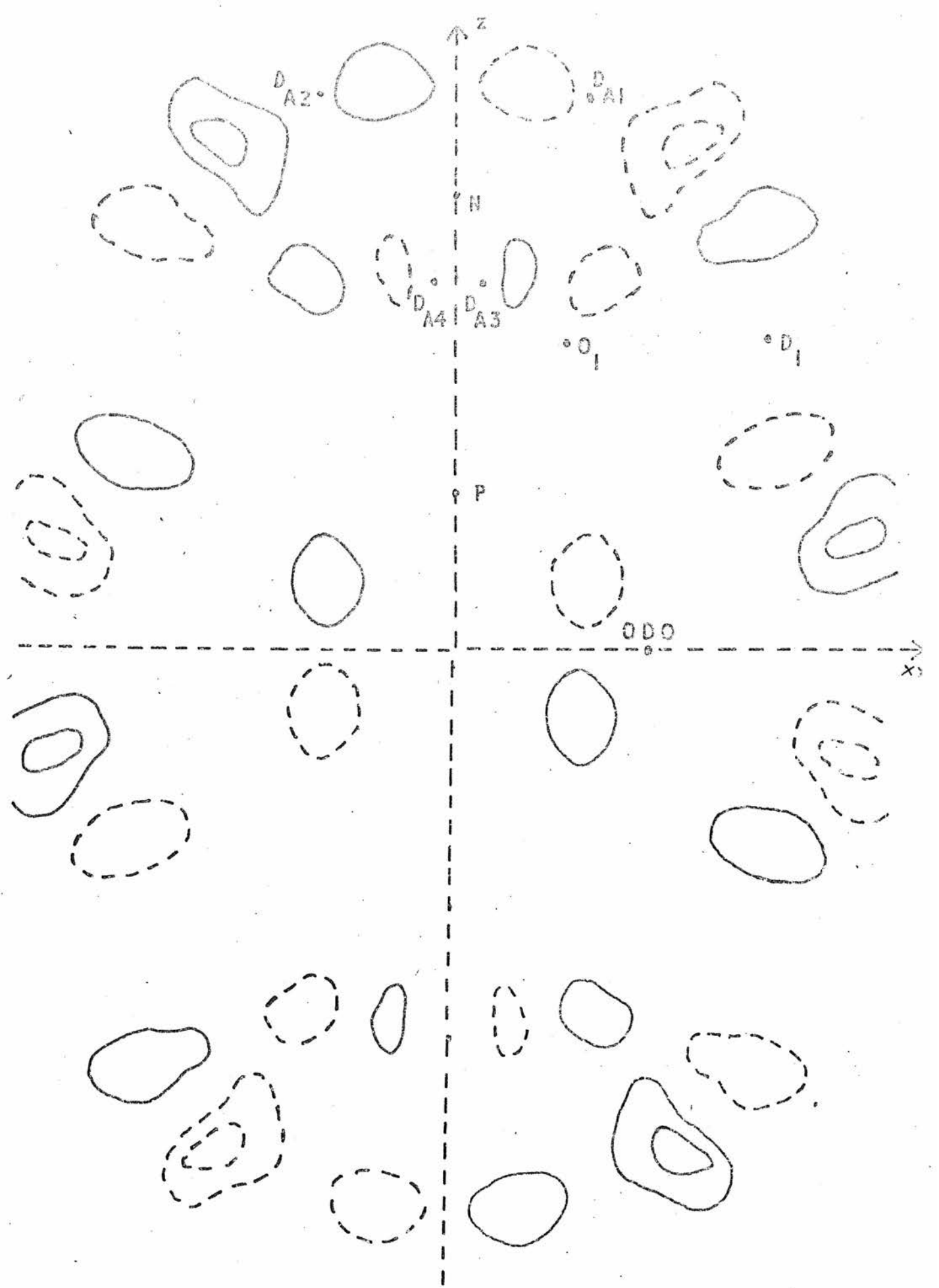

FIGURE 6·7

ACKNOWLEDGEMENTS

It is a pleasure to extend thanks to those who have helped the author throughout the period of this work.

To Professor N. Feather for extending the hospitality of the Department of Natural Philosophy. To the Science Research Council for financial support, and for providing research facilities at A.E.R.E., Harwell, where all the experimental work was carried out.

To Professor W. Cochran and Dr. G.S. Pawley for their guidance and help and their encouragement at all times, especially during the writing of this thesis. To other members of this department for helpful discussions and advice.

To the many members of the Materials Physics Division at Harwell, who have greatly assisted the author during the course of the experimental work; notably Mr. D.H.C. Harris, Dr. B.C.G. Haywood, Dr. M.W. Stringfellow and Mr. N.J. Hance. Finally, to Mrs. R.W. Chester for her painstaking work in preparing this thesis.

REFERENCES

1. Born, M. and Huang, K., The Dynamical Theory of Crystal Lattices, Oxford University Press (1954).
2. Cochran, W., Rep. Prog. in Phys., 26, 1 (1963).
3. Cochran, W., Advanc. Phys. 9, 387 (1960).
4. Cochran, W., Advanc. Phys. 10, 401 (1961).
5. Cochran, W. and Cowley, R.A., Handbuch der Physik, 25/2a, 59 (1967).
6. Maradudin, A.A., Montroll, E.W. and Weiss, G.M., Solid State Physics, Supp. 3 (1959).
7. Herman, F.J., Phys. Chem. Solids 8, 405 (1959).
8. Pawley, G.S., Phys. Status. Solidi, 20, 347 (1967).
9. Weinstock, R., Phys. Rev., 65, 1 (1944).
10. Van Hove, L., Phys. Rev. 95, 249 (1954).
11. Brockhouse, B.N., Phonons and Phonon Interactions, edited by Bak, T.A. 221 (1964).
12. Harris, D., Cocking, S.J., Egelstaff, P.A. and Webb, F.J., Inelastic Scattering of Neutrons in Solids and Liquids, I.A.E.A., (Vienna), (1963).
13. Martin, D.H., Advanc. Phys. 14, 39 (1965).
14. Russel, J.P. and Hardy, J.R., Phonons in Perfect Lattices, edited by Stevenson, R.W.H., 235 and 245 (1966).
15. Cooper, M.J. and Nathans, R., Acta Crys. 23, 357 (1967).
16. Peckham, G.E., Saunderson, D.H. and Sharp, R.I., Britt. J. Appl. Phys. 18, 473 (1967).
17. Collins, M.F., Britt. J. Appl. Phys. 14, 805 (1963).
18. Martin, R., A.E.R.E. Report, M1904.
19. Smith, D.B.J., Martin, R., Russell, M.C.B., A.E.R.E. Report, M1913.
20. Russell, M.C.B., Martin, R., Brown, L.H., Smith, D.B.J., A.E.R.E. Report, R-5663.
21. Ahmed, F.R. and Cruickshank, D.W.J., Acta Cryst. 5, 852 (1952).
22. Abrahams, S.C., Robertson, J.M. and White, J.G., Acta Cryst. 2, 233 and 2, 238 (1949).
23. Cruickshank, D.W.J., Acta Cryst. 10, 504 (1957).

24. Sherwood, J.N., and Thomson, S.J., J. Scient. Instrum. 37 242 (1960).

25. Arndt, U.W. and Willis, B.T.M., Single Crystal Diffractometry, Cambridge University Press (1966).

26. Nilsson, N., Ark. Fys. 12, 247 (1957).

27. Cooper, M.J. and Rouse, K.D., Acta Cryst. A24, 405 (1968).

28. Cooper, M.J. and Rouse, K.D., Acta Cryst. A25, 615 (1969).

29. Jeffery, J.W. and Rose, K.M., Acta Cryst. 17, 343 (1964).

30. Zachariasen, W.H., Theory of X-Ray Diffraction in Crystals, New York, (1945).

31. Zachariasen, W.H., Acta Cryst. 23, 558 (1967).

32. Bacon, G.E. and Lowde, R.D., Acta Cryst. 1, 303 (1948).

33. James, R.W., The Optical Principles of the Diffraction of X-Rays, London, (1962).

34. Buerger, M.J., Crystal Structure Analysis, New York (1960).

35. Wilson, A.J.C., Nature 150, 152 (1942).

36. Cruickshank, D.W.J., Acta Cryst. 9, 754 (1956).

37. Pawley, G.S., Acta Cryst. 17, 457 (1964).

38. Higgs, P.W., Acta Cryst. 8, 99 (1955).

39. Pawley, G.S., Phys. Status Solidi, 20, 347 (1967).

40. Cruickshank, D.W.J., Acta Cryst. 9, 754 (1956).

41. Pawley, G.S. and Yeats, E.A., Acta Cryst. B25, 2009 (1969).

42. Duckworth, J., Willis, B.T.M. and Pawley, G.S., Acta Cryst. A26, 263 (1970).

43. Pawley, G.S., Acta Cryst. (in the press).

44a. Johnson, C.K., Thermal Neutron Diffraction, Oxford University Press (1970).

44. Cochran, W.C. and Pawley, G.S., Proc. Roy. Soc. A280, 1 (1964).

45. Pawley, G.S., Thesis, Cambridge University (1962).

46. Powell, B.M., Neutron Inelastic Scattering, I.A.E.A. Symposium, Copenhagen (1968).

47. Craig, D.P., Mason, R., Pauling, P., and Santry, D.P., Proc. Roy. Soc. A286, 98 (1965).

48. Dolling, G., Powell, B.M. and Pawley, G.S., (1970). In preparation.

49. Kitaigorodskii, A.I., Acta Cryst. 18, 585 (1965).

50. Kitaigorodskii, A.I., J. Chim. Phys. 63, 6 (1966).

51. Ito, M., Suzuki, M., Yokoyama, T., Excitons Magnons and Phonons in Molecular Crystals, Cambridge University Press (1968).

52. Pawley, G.S. and Cyvin, S.J., J. Chem. Phys. 52 No. 8, 4073 (1970).

53. Pawley, G.S. and Yeats, E.A., Sol. Stat. Comm. 7 No. 3, 385 (1969).

54. Harada, I., and Shimanouchi, T., J. Chem. Phys. 44 No. 5, 2026

55. Hadni, A., Excitons, Magnons and Phonons in Molecular Crystals, Cambridge University Press (1968).

56. Kastler, A. and Rousset, A., J. Phys. Rad. 2, 49 (1941).

57. Ichishima, I., Nippon Kagaku Zasshi 71, 607 (1950).

58. De Boer, L., Trans. Farad. Soc. 32, 10 (1932).

59. Kanzig, W., Solid State Physics 4, 1, Academic Press, New York (1957).

60. Megaw, H.D., Ferroelectricity in Crystals, Methuen, London (1957).

61. Cochran, W., Advanc. Phys., 9, 387 (1960).

62. Cochran, W., Advanc. Phys. 10, 401 (1961).

63. Cochran, W., Advanc. Phys. 18, 157 (1969).

64. Devonshire, A.F., Advanc. Phys. 3, 85 (1954).

65. West, J., Z. Krist. 74, 306 (1930).

66. De Quervain, M., Helv. Phys. Acta 17, 509 (1944).

67. Frazer, B.C. and Pepinsky, R., Acta Cryst. 6, 273 (1953).

68. Bacon, G.E. and Pease, R.S., Proc. Roy. Soc. A220, 397 (1953) and A230, 359 (1955).

69. Ueda, R., J. Phys. Soc. Japan, 3, 328 (1948).

70. Tenzer, L., Frazer, B.C. and Pepinsky, R., Acta Cryst. 11, 505 (1958).

71. Keeling, R.O. and Pepinsky, R., Z. Krist. 106, 236 (1955).

72. Nagamiya, T., Prog. Theor. Phys. 7, 275 (1952).

73. Mason, W.P. and Matthias, B.T., Phys. Rev. 88, 477 (1952).

74. Cochran, W., Phys. Rev. Letts. 3, 521 (1959).

75. Cochran, W., Z. Krist. 112, 30 (1959).

76. Dick, B.G. and Overhauser, A.W., Phys. Rev. 112, 90 (1958).

77. Cowley, R.A., Phys. Rev. A134, 981 (1964).

78. Shirane, G., Nathans, R. and Minkiewicz, V.J., Phys. Rev. 157, 396 (1967).

79. Landau, L.D., Physik Z. Soivjetunion, 11, 26 (1930).

80. Landau, L.D. and Lifshitz, E.M., Statistical Physics, (Addison Wesley) (1958).

81. Montgomery, H., Proc. Roy. Soc. 309, 521 (1969).

82. Shur, M.S., Sov. Phys. - Solid State, 8, 43 (1966); 11, 394 (1966); and 12, 181 (1967).

83. Montgomery. H., (1971) to be published.

84. Kobayashi, K.K., J. Phys. Soc. Japan, 24, 497 (1968).

85. Sirotin, Y.I., Sov. Phys. - Crystall., 12, 175 (1967).

86. Kaminov, I.P., and Damen, T.C., Phys. Rev. Lett. 20, 1105 (1968).

87. Paul, G.L., Cochran, W., Cowley, R.A. and Buyers, W., to be published.

88. Skalyo, J., Frazer, B.C. and Shirane, G., to be published.

89. Skalyo, J., Frazer, B.C. and Shirane, G., to be published.

90. Kobayashi, K.K., J. Phys. Soc. Japan, 24, 497 (1968).

91. De Gennes, P.G. Magnetism, Vol. 3, London, Academic Press, (1963).

92. Meister, I.H., Skalyo, J., Frazer, B.C. and Shirane, G., Phys. Rev., 184, 550 (1969).

93. Busch, G., Helv. Phys. Acta, 11, 269 (1938).

94. Tenzer, L., Frazer, B.C., Pepinsky, R., Acta Cryst. 11, 505 (1958).

95. Cochran, W., Neutron Inelastic Scattering, Vol. 1, International Atomic Energy Agency, Vienna (1968).

96. Lipson, H. & Cochran, W., Determination of Crystal Structures, Bell and Sons, London (1966), p. 323.

97. Bragg, W.L. and West, J., Phil. Mag. 10, 823 (1930).

98. Donohue, J., Science, 165, 1091 (1969).

99. Donohue, J., Science, 167, 1700 (1970).

APPENDIX

Reprinted from *Acta Crystallographica*, Vol. B 25, Part 10, October 1969

PRINTED IN DENMARK

Acta Cryst. (1969). B**25**, 2009

A Neutron-Diffraction Study of Perdeuteronaphthalene

BY G. S. PAWLEY AND ELIZABETH A. YEATS

Department of Natural Philosophy University, of Edinburgh, Edinburgh 8, *Scotland*

(*Received* 16 *November* 1968)

The crystal structure of perdeuteronaphthalene, $C_{10}D_8$, is very similar to that of $C_{10}H_8$. The space group is $P2_1/a$ with $a=8{\cdot}266\pm0{\cdot}008$, $b=5{\cdot}968\pm0{\cdot}006$, $c=8{\cdot}669\pm0{\cdot}008$ Å; $\beta=122{\cdot}92\pm0{\cdot}02°$. 331 independent observations give an R value of 5·2% in a refinement where the anisotropic temperature factors were fixed at the best values obtained with the use of the rigid-body thermal-motion constraint, and the positional parameters were constrained to the *mmm* symmetry of the free molecule. Statistical tests showed that no significant improvement is possible on removing the constraints. Consequently, the molecular geometry resulting from the constrained refinements was better determined than it would have been from a conventional unconstrained refinement.

Introduction

The present investigation of the crystal structure of perdeuteronaphthalene, $C_{10}D_8$, is part of the study of the lattice dynamics of molecular crystals. Measurement of phonon frequencies is best done with neutron inelastic coherent scattering. Hydrogen is a very strong incoherent scatterer, and for this reason fully deuterated crystals are preferred.

Calculations have been made of phonon frequencies in naphthalene by Pawley (1967), with the use of the crystal structure of $C_{10}H_8$ as determined by X-ray dif-

fraction (Cruickshank, 1957). We expected a slight change in crystal structure on deuteration and this we wished to find. Neutron diffraction affords a method of accurate determination of nuclear positions and is ideal for obtaining a starting point for lattice dynamical calculations.

The easiest of these calculations to make involves rigid-body motion of the molecules. Consequently when the diffraction data are used to refine the crystal structure, a structure-factor least-squares (SFLS) procedure incorporating a rigid-body thermal parameter constraint is appropriate (Pawley, 1964). If the assumption of molecular rigidity is valid we would expect the molecules to retain in the crystal the symmetry they have in the free state. Consequently another constrained SFLS refinement is of interest, in which the molecules are kept to *mmm* symmetry in the crystal although the molecular site is only centrosymmetric.

Experimental

A large single crystal of 98% deuterated naphthalene was grown by Dr Sherwood of the University of Strathclyde by the moving-vessel technique (Sherwood & Thomson, 1960). A sphere of diameter 7 mm was cut from one end of the crystal, and was mounted with z^* vertical, inside a sealed soda-glass bulb to reduce sublimation losses.

The mosaic spread of the crystal was 0·5° (full width at half height) which was thought to be sufficient for extinction effects to be small, therefore no shock cooling was attempted. Rapid cooling in liquid nitrogen tends to shatter large crystals of this sort.

The unit cell of $C_{10}D_8$ is slightly different from that of $C_{10}H_8$, being

$$\begin{aligned} a &= 8{\cdot}266 \pm 0{\cdot}008 \text{ Å} \\ b &= 5{\cdot}968 \pm 0{\cdot}006 \\ c &= 8{\cdot}669 \pm 0{\cdot}008 \qquad \text{in } P2_1/a\,. \\ \beta &= 122{\cdot}92 \pm 0{\cdot}02^\circ \end{aligned}$$

331 independent intensities were measured at 295°K on the Ferranti four-circle diffractometer on the DIDO reactor at Harwell. A number of equivalent reflexion pairs were measured and the average agreement was 1%. Table 1 contains the $|F_{obs}|$ used in the structure refinements.

Computational

No attempts were made to correct the data for absorption, extinction or thermal diffuse scattering. The maximum of absorption was 7%, owing mainly to the incoherent scattering from the 2% of hydrogen. The angular variation in absorption would be much smaller than this, giving a slight error to the mean-square translational displacement tensor **T**. We found no evidence of extinction when analysing the result of the refine-

Table 1. *Observed and calculated structure factors*

The columns are *hkl*, $|F_{obs}|$, $|F^{r.b.}{}_{calc}|$ and $|F^{mmm}{}_{calc}|$.

ment. A thermal diffuse scattering correction (Cooper & Rouse, 1968) was not applied as this requires a reliable lattice dynamical model. The present study is a necessary step towards this goal. All refinements were based on $|F_{obs}|$ with unit weights.

The first refinements were carried out by the use of the rigid-body thermal-parameter constraint program (Pawley, 1964). With neutron scattering lengths of 0·66 and 0·65 for carbon and deuterium atoms the conventional R value reached 5·30%, dropping to 5·10% when the scattering lengths for the deuterium positions were reduced to 0·63 to take account of the 2% of hydrogen remaining in the crystal.

Removing the thermal-parameter constraints gave no significant improvement at the 2% level of the F distribution, assuming that $\left(\frac{R \text{ initial}}{R \text{ final}}\right)^2$ is F distributed (Pawley, 1966).

We therefore list only the results of the constrained refinement. In Table 1 the calculated structure factors are listed as $|F_{calc}^{r.b.}|$. The mean square rigid-body translational and librational tensors are

$$\mathbf{T}=\begin{bmatrix} 4\cdot84 & 0\cdot20 & -0\cdot09 \\ & 2\cdot92 & -0\cdot06 \\ & & 2\cdot29 \end{bmatrix} \text{Å}^2\times10^{-2}$$

$$\sigma(\mathbf{T})=\begin{bmatrix} 0\cdot09 & 0\cdot06 & 0\cdot08 \\ & 0\cdot08 & 0\cdot08 \\ & & 0\cdot15 \end{bmatrix} \text{Å}^2\times10^{-2}$$

$$\mathbf{L}=\begin{bmatrix} 31\cdot59 & -3\cdot49 & 0\cdot11 \\ & 18\cdot45 & -1\cdot16 \\ & & 19\cdot12 \end{bmatrix} \text{deg}^2$$

$$\sigma(\mathbf{L})=\begin{bmatrix} 1\cdot98 & 0\cdot78 & 1\cdot05 \\ & 0\cdot93 & 0\cdot73 \\ & & 0\cdot85 \end{bmatrix} \text{deg}^2$$

[The use of **L** instead of the **ω** in the original paper (Cruickshank, 1956) seems now to be generally accepted]. The comparison of these tensors with the calculations on $C_{10}H_8$ can only be rough, so we must wait for phonon measurements and an improved model before a good comparison can be made.

The nuclear fractional coordinates found in this refinement are listed in Table 2 under the columns headed $\bar{1}$ symmetry, the molecular site symmetry. The anisotropic temperature factors in this Table are those derived from **T** and **L** and the fractional coordinates just mentioned.

The nuclear positions in the coordinate system defined by the inertia axes of the molecule are given in Table 3. The z coordinates are deviations from the plane perpendicular to the axis of greatest inertia. This is the mean molecular plane weighted heavily by the carbon positions. The least-squares standard deviations are 0·0055 and 0·0079 Å for the carbon and deuterium atom positions respectively. The deviations from the mean molecular plane are no more than one standard deviation for the carbon atoms, but about two standard deviations for two of the deuterium atoms. We need to know whether this is evidence for molecular distortion or whether the deviations are insignificant.

To answer this question we should analyse the deviations from *mmm* symmetry, the symmetry of the molecule in the free state. Column 2 of Table 3 shows the x and y coordinates for the symmetry averaged molecule. We see that in three of the eight coordinate pairs averaged, namely $C_x(A\&E)$, $C_y(A\&E)$ and $D_x(b\ \&\ d)$, the individuals differ by about three standard deviations. The following analysis shows, however, that these deviations are insignificant.

The most valid test of molecular strain from *mmm* symmetry is given by comparing the results of refinements with and without the symmetry imposed. A new program was written to apply the molecular symmetry constraint throughout the SFLS refinement. The procedure which has been described by Pawley (1969) has been followed. A relatively small number of additions have been made to the usual basic least-squares program with the use of the *Editor* system, written by Dr J. G. Burns of Edinburgh. Unfortunately, the rigid-body thermal parameter constraint program is not

Table 2. *Fractional coordinates of the molecule with and without the symmetry constraint, and the thermal parameters for the expression* $\exp[-10^{-4}(h^2b_{11}+k^2b_{22}+l^2b_{33}+2klb_{23}+2lhb_{31}+2hkb_{12})]$ *obtained with the rigid body thermal parameter constraint.*

	mmm symmetry			$\bar{1}$ symmetry			Rigid body					
	x/a	y/b	z/c	x/a	y/b	z/c	b_{11}	b_{22}	b_{33}	b_{23}	b_{31}	b_{12}
C(C)	0·0482	0·1030	0·0359	0·0480	0·1035	0·0352	116	163	174	−10	69	0
C(B)	0·1149	0·1606	0·2205	0·1155	0·1591	0·2206	202	250	187	−50	87	−31
C(D)	0·0761	0·2476	−0·0782	0·0755	0·2487	−0·0777	190	200	235	15	118	−18
C(A)	0·0857	0·0174	0·3267	0·0857	0·0164	0·3260	262	357	181	−12	115	3
C(E)	0·0099	0·1869	−0·2555	0·0088	0·1876	−0·2566	251	311	228	52	145	16
D(b)	0·1883	0·3185	0·2733	0·1878	0·3178	0·2718	328	314	253	−119	126	−110
D(d)	0·1499	0·4043	−0·0213	0·1511	0·4053	−0·0219	307	232	338	−6	182	−89
D(a)	0·1368	0·0627	0·4665	0·1353	0·0630	0·4650	432	561	197	−42	163	−17
D(e)	0·0318	0·2978	−0·3408	0·0327	0·2972	−0·3414	402	448	311	113	238	14

written in the *Editor* system, so both constraints are not possible simultaneously at present.

The number of parameters needed to determine the nuclear positions for the full-symmetry molecule is 12, compared with 27 in the unconstrained case. Nine of these parameters are indicated in Fig. 1, the remaining three being the three Euler angles necessary to form the rotation matrix which puts the molecule in the correct orientation. This matrix is formed as described by Pawley (1969) and the rotated molecule is then transformed to crystal fractional coordinates by the matrix

$$\begin{pmatrix} \frac{1}{a} & 0 & \frac{-\cot}{a}\beta \\ 0 & \frac{1}{b} & 0 \\ 0 & 0 & \frac{\mathrm{cosec}}{c}\beta \end{pmatrix}.$$

The best starting values for the Euler angles were

$$\begin{aligned} \varphi &= -1{\cdot}1707^\circ \\ \theta &= \ 4{\cdot}3952 \\ \psi &= \ 2{\cdot}0597 \end{aligned}$$

Refinement was carried out by anisotropic temperature factors fixed at the values obtained from the rigid body thermal parameter constraint. The R value reached was $R=5{\cdot}15\%$, with

$$\begin{aligned} \varphi &= -1{\cdot}1707 \pm 0{\cdot}0008^\circ \\ \theta &= \ 4{\cdot}3946 \pm 0{\cdot}0010 \\ \psi &= \ 2{\cdot}0592 \pm 0{\cdot}0012 \end{aligned}$$

The calculated structure factors are given in Table 1 under the heading $|F^{mmm}_{\mathrm{calc}}|$.

The atomic coordinates are listed in Tables 2 and 3. This R value is not significantly worse than $R=5{\cdot}10\%$, obtained with the thermal parameter constraint but no symmetry constraint.

When the thermal parameters were allowed to vary independently, the R value dropped to $R=4{\cdot}98\%$. This improvement is not significant on the 25% level of the F distribution, and the results are therefore not given here.

We see in Fig. 1 the large difference between the lengths of the bonds C(C)–C(D) and C(D)–C(E). Although this is in agreement with the X-ray result on $C_{10}H_8$ (Cruickshank, 1957), it is instructive to test the significance of this variation with yet another constrained refinement. Let us take a model for the molecule determined by two parameters, the C–C and the C–D bond lengths. Assume that both rings are perfect hexagons with the C–D bonds pointing radially from the hexagon centres. All the atomic positions in the crystal are now determined by five parameters, the two bond lengths and the three Euler angles.

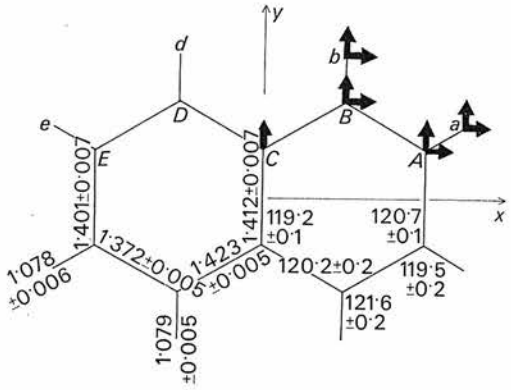

Fig. 1. The molecule of naphthalene. The capital letters denote the carbon atoms, the small letters the deuterium atoms. The bold arrows indicate the positional parameters consistent with the molecular symmetry. The bond lengths and angles and their errors come from the refinement incorporating the molecular symmetry and using the rigid-body thermal parameters, and are uncorrected for librational motion.

Table 3. *Coordinates of the molecule in* Å

The last columns contain unconstrained coordinates transformed into the inertia axes coordinate system.

Atom	Constrained *mmm* molecule	Best *mmm* molecule from next 2 columns	Centrosymmetric molecule, thermal parameter constraint		Atom
	–	–	−0·0088		X
C(C)	0·7060	0·7060	0·7076		Y coordinates
	–	–	−0·0015		Z
	1·2420	1·2399	1·2368	−1·2429	
C(B)	1·3995	1·3987	1·3982	1·3991	C(D)
	–	–	0·0055	−0·0055	
	2·4219	2·4220	2·4133	−2·4307	
C(A)	0·7004	0·6970	0·7046	0·6894	C(E)
	–	–	−0·0008	−0·0031	
	1·2252	1·2252	1·2043	−1·2461	
D(b)	2·4781	2·4782	2·4764	2·4800	D(d)
	–	–	−0·0005	0·0095	
	3·3575	3·3577	3·3453	−3·3700	
D(a)	1·2359	1·2332	1·2458	1·2205	D(e)
	–	–	−0·0154	0·0155	
C	0·0033	Standard	0·0055		
D	0·0046	deviations	0·0079		

A constrained refinement was carried out, giving C-C = 1·4056 ± 0·0015 Å and C–D = 1·073 ± 0·003 Å, but the R values obtained by the rigid-body thermal parameters and then by variable thermal parameters were 6.0 and 5·8% respectively. These are both significantly poorer than previous R values on the 2% level of the F distribution. We therefore conclude that the extra constraint is not realistic, and that the difference between the C(C)–C(D) and C(D)–C(E) bonds found earlier is highly significant.

Conclusion

From our statistical tests we have found no evidence of deviation from either the rigid-body thermal motion model or the full-molecular-symmetry model. We have not attempted to fit the third or fourth cumulants introduced by Johnson (1969) but to the approximation of second cumulants (the usual approximation) we should have optimized our molecular geometry determination by applying these physically reasonable constraints. Indeed, we see that the standard deviations for the positional parameters are considerably diminished by the symmetry constraint, giving bond lengths and angles with errors as shown in Fig. 1. An attempt to simplify the model further gave a significantly poorer fit, indicating that the C–C bonds differ significantly in length.

We have presented three different constrained refinements specifically to answer three separate questions. The task of combining these constraint procedures in one general program is great indeed, but a system where this is possible should be aimed at. In the present example the symmetry constraint gave the least change in the R value, the symmetry information being incorporated in the SFLS refinement. This is in contrast to the recent work of Maslen (1968) where this assumed symmetry information is used in 'phase refinement' after the fitting procedure is concluded. It will be of interest to investigate the 'phase refinement' by the use of the results of a symmetry constrained refinement.

We wish to thank Dr John Sherwood of Strathclyde University for growing the crystal, Mr George Paul for help in collecting the diffraction data, and the SRC for the award of a research studentship to one of us (E.A.Y.). Finally we wish to thank Professor W. Cochran for his continued interest in this work.

References

COOPER, M. J. & ROUSE, K. D. (1968). *Acta Cryst.* A**24**, 405.
CRUICKSHANK, D. W. J. (1957). *Acta Cryst.* **10**, 504.
JOHNSON, C. K. (1969). To be published.
MASLEN, E. N. (1968). *Acta Cryst.* B**24**, 1165.
PAWLEY, G. S. (1964). *Acta Cryst.* **17**, 457.
PAWLEY, G. S. (1966). *Acta Cryst.* **20**, 631.
PAWLEY, G. S. (1967). *Phys. Stat. Sol.* **20**, 347.
PAWLEY, G. S. (1969). *Acta Cryst.* A**25**, 531.
SHERWOOD, J. N. & THOMSON, S. J. (1960). *J. Sci. Instrum.* **37**, 242.

Printed in Denmark by P. J. Schmidts Bogtrykkeri, Vojens

State Communications, Vol. 7, pp. 385–388, 1969. Pergamon Press. Printed in Great Britain

LOW FREQUENCY PHONONS IN NAPHTHALENE

G.S. Pawley and Elizabeth A. Yeats

Department of Natural Philosophy, University of Edinburgh, Edinburgh 8, Scotland

(*Received* 11 *December* 1968)

Using neutron inelastic scattering we have measured some phonons of anomalously low frequency in perdeuteronaphthalene. This supports results obtained by others studying vibronic transitions. These phonons occur near the Brillouin zone boundary and therefore would contribute pronounced peaks in the density of phonon states, at about 10 cm^{-1} and 30 cm^{-1}. We cannot at present identify the form of molecular motion in these phonons.

WE made a preliminary study of the dispersion curves of perdeuteronaphthalene. chnique of neutron coherent inelastic ing[1] has been used, and it is because high incoherent scattering cross-section logen that a fully deuterated crystal was ary.

e specimen used was a large single crystal er cent deuterated naphthalene grown for Dr. J. Sherwood of the University of Strath- using the moving vessel technique.[2] It was der of length 3 cm, dia. 1.7 cm, with a spread of 1° (half-width at half-height). mounted with the b^*–c^* plane horizontal, ntaining the incident and scattered neut- The measurements were made on the triple utron spectrometer on the PLUTO reactor ell, using the constant-Q mode of opera- ith neutron energy loss (down scattering). surements were made at room temperature.

e modes of vibration which can be measured technique usually have frequencies con- ly lower than those of the internal modes tion, so we would expect to be able to e those modes which involve rigid motions olecules. There are two molecules in the e unit cell of the crystal, so there will in be twelve modes of vibration. At zero wave-vector there will be six purely translational modes and six purely librational modes, each set consisting of three symmetric and three anti-symmetric modes. With the wave-vector along the symmetry axis of the crystal we still have symmetric and antisymmetric modes, but their character will not be pure translations or pure librations. We are measuring the modes along this axis.

It is necessary at the start of such a study to set up a model for the crystal and calculate eigenvectors and eigenfrequencies for the model. This has already been done for naphthalene[3] and we have used the eigenvectors of the model to calculate the coherent neutron scattering. This we then use as a guide, telling us where in reciprocal space to make a measurement for any particular phonon. This assumes that the eigen-vector calculated from the model is not very different from the actual eigenvector. We believe this to be true because the eigenvectors calculated for anthracene are very similar to those of naphthalene, showing that the eigenvectors change very little while the model changes by a large amount.

We searched for modes of predominantly librational character near the Brillouin zone boundary in the energy region indicated by the

of the Brillouin zone.

his is not the first time that the existence nons of such low frequencies has been sted. Evidence has been reported from v. studies of vibronic transitions.[6,7] Maria[6] ggested that the Raman measurements may ngly interpreted, but there are now availa- sults of increased accuracy.[5] It is much more actory to explain the u.v. results as evidence eraction with phonons well away from zero vector, indeed the phonons we have measured. xciton-phonon coupling giving rise to Maria's s must depend on the eigenvector for the ular phonon concerned. The intensity of the -band must therefore depend on the crystal ation. This is not mentioned by Maria, but explain the result that for some crystals a in the phonon density of states is suggested cm^{-1} while for other crystals 28 cm^{-1} is indi- . For one set of crystals interaction with one n branch is favoured, while for the other set he other phonon branch which is favoured.

wledgements – We wish to thank Dr. J. ood of Strathclyde University for growing ystal, Mr. G. Paul for help in taking the irements, and the S.R.C. for the award of a ch studentship to one of us (E.A.Y.). ly we wish to thank Professor W. Cochran s interest in and support of this work, and ssor A.B. Zahlan for helpful discussion.

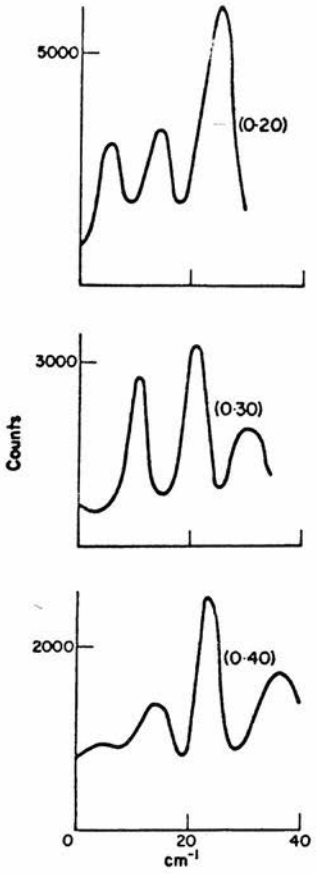

FIG. 2. The neutron groups for some of the anomalous phonons.

ble 1. *Frequencies in* THz (10^{12}c/s) *at three points in the Brillouin zone,* q = (0,0,0); (0,0.25,0) nd (0,0.5,0). *The columns headed* $C_{10}H_8$ *give the frequencies of the modes in Fig. 1 reference* 3. *The other columns give the frequencies for the same modes but in* $C_{10}D_8$

(0,0,0)		(0,0.25,0)		(0,0.5,0)	
$C_{10}H_8$	$C_{10}D_8$	$C_{10}H_8$	$C_{10}D_8$	$C_{10}H_8$	$C_{10}D_8$
4.18	3.83	3.62	3.36	2.97	2.82
3.87	3.55	3.51	3.23	2.97	2.82
2.76	2.59	2.81	2.66	2.73	2.58
2.65	2.57	2.57	2.46	2.73	2.58
2.32	2.18	2.46	2.32	1.92	1.80
1.85	1.73	1.80	1.69	1.92	1.80
1.68	1.63	1.59	1.50	1.67	1.58
1.48	1.38	1.38	1.31	1.67	1.58
1.39	1.35	1.30	1.26	1.49	1.42
–	–	1.19	1.15	1.49	1.42
–	–	0.81	0.78	1.17	1.13
–	–	0.62	0.60	1.17	1.13

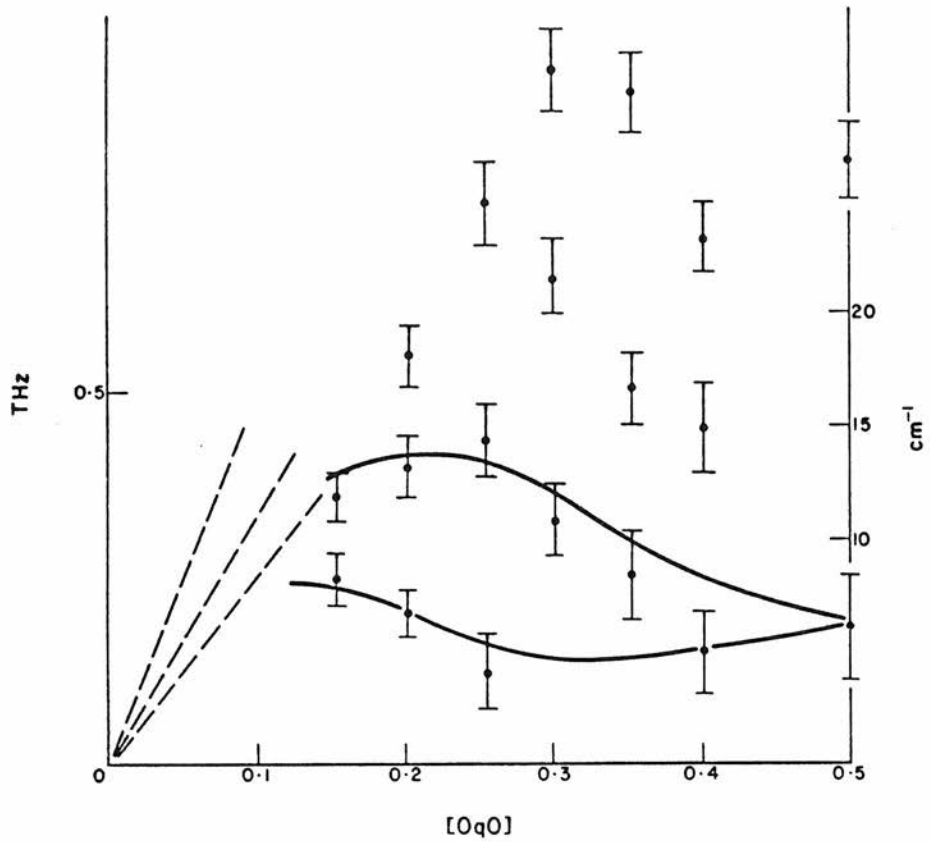

FIG. 1. The extent of the measured dispersion curves. The broken lines are the curves expected fo $C_{10}H_8$ as calculated from the elastic constant measurements.[4]

model calculations, but found modes at much lower frequencies. The extent of the measured dispersion curves is shown in Fig. 1. The neutron groups indicating the anomalously low-frequency phonons are given in Fig. 2. We have tried to explain these neutron groups in terms of the various processes which give rise to spurious results: Bragg scattering from satellite crystallites, Bragg scattering at monochromator harmonic wavelengths, two phonon scattering. However we can find no reason to doubt the results.

We cannot say at present what the forms of the eigenvectors are, but it is most likely that they have a large librational component. Figure 1 shows the dispersion curves for the acoustic and therefore translational phonons calculated using the ultrasonic elastic constant measurements in $C_{10}H_8$.[4] These branches must be continuous with those of the anomalous phonons, but it is most likely that the character of the eigenvector changes to being mainly librational near the z boundary.

The reason for investigating initially in t energy region suggested by the model is beca the model gave a good agreement with the Ra measurements.[5] It could be argued that there would be considerable change on deuteration, a model calculation for perdeuteronaphthalen shows no great decrease in the phonon freque (Table 1). We can use the result of this calc lation to estimate the Raman frequencies in (by lowering the measured values for $C_{10}H_8$ pr portionately. This gives values of 136, 114; 81; 66, 55 cm^{-1}, all well above the values of and 30 cm^{-1}. These last values are the frequ cies for the peaks in the phonon density of s which would occur if the anomalous phonons have observed have flat branches over a larg

REFERENCES

1. BROCKHOUSE B.N., *Inelastic Scattering of Neutrons in Solids and Liquids* p. 113 I.A.E.A.(1961).
2. SHERWOOD J.N. and THOMSON S.J., *J. scient. Instrum.* 37, 242 (1960).
3. PAWLEY G.S., *Phys. Status Solidi* 20, 347 (1967).
4. ALEKSANDROV K.S., BELIKOVA G.S., RYZHENKOV A.P., TESLENKO V.R. and KITAIGORODSKII A.I., *Kristallografiya* 8, 221 (1963).
5. WILKINSON G.R., private communication (1966).
6. MARIA H.J., *J. chem. Phys.* 40, 551 (1964).
7. ZAHLAN A.B., In *Excitons, Magnons and Phonons in Molecular Crystals* (Edited by ZAHLAN, A.B p. 153. Cambridge University Press, 1968.

Nous avons trouvé, par diffusion inélastique des neutrons, des phonons de fréquence anormalement basse dans le perdeutéronaphtalène. Ceci confirme les résultats d'autres études de transitions vibroniques. Ces phonons se trouvent près du bord de la zone de Brillouin et devraient produire des pics aigus, à 10 cm^{-1} et 30 cm^{-1} dans la courbe de densité d'états des phonons. Nous ne pouvons pas à présent identifier les mouvements moléculaires qui correspondent à ces phonons.